Extreme Hydrodynamic Loading on Horizontal Pipelines

By

Behnaz Ghodoosipour

Thesis submitted in partial fulfillment of the requirements for:

Doctorate in Philosophy - Civil Engineering

Academic advisors: Prof. Ioan Nistor, Prof Majid Mohammadian

Department of Civil Engineering

Faculty of Engineering

University of Ottawa

ABSTRACT

Extreme events such as tsunamis and floods have caused massive damaging consequences to nearshore infrastructure. This has been more significant recently due to a changing climate. Transmission pipelines are among such infrastructures and need to be protected against potential extreme events. Design of pipelines requires a comprehensive understanding of the exerting hydrodynamic forces. Understanding the hydrodynamic forces acting on pipelines is vital in ensuring their safe operation and avoiding potential damage to the environment. The American Society of Civil Engineers (ASCE), in its ASCE7 Chapter 6: Tsunami Loads and Effects, the new standard for tsunami impacts and loading, stresses the necessity to study tsunami loads on pipelines. To address these issues, the following study is the first of its kind to investigate loading on horizontal pipelines due to tsunami-like bores. Research experiments are in line with the American Society of Civil Engineers, ASCE7 recommendation for studying tsunami loading on pipelines.

The primary objective of this study was to measure and analyze the forces induced by extreme hydrodynamic events on submerged and above-ground pipelines. This was achieved by combining a comprehensive experimental study and detailed CFD numerical simulations. The study aimed to provide guidelines for the design of pipelines in tsunami-prone areas. At the same time, this study investigates the flow hydrodynamics in the case of dam-break waves impacting the horizontal pipelines and proposes specific values for resistance and lift coefficients in the case of a transient tsunami-like coastal flow for different relative gap ratios and submergence conditions.

This study presents results from investigating the loading on pipelines located on flat and sloped beds induced by transient dam break wave. Different pipe configurations were investigated by changing the distance of the pipe to flume bed as well as the initial pipe submergence level and different flow and initial bed conditions. Different bed slopes were also tested. It was found that under dry bed condition, the initial horizontal impulse force and the lift force were considerably larger for smaller *e/D*. However, altering the gap ratio (*e/D*) under wet bed conditions did not considerably change exerted force components. Investigations over the impact of pipe submergence level showed a decreased impulse force with an increasing initial level of submergence (S/D) due to the decreased effective contact area of the pipe exposed to surge. Increasing the bed slope demonstrated to increase the induced horizontal force. This study suggests force coefficient values for various Froude numbers and several pipe configurations through proposed force coefficient versus Froude number graphs. Suggested resistance and lift coefficients for the experimental conditions investigated are in the range of $1 < C_R < 3.6$ and $-2.8 \leq C_L < 2.8$ respectively. This wide range of suggested force coefficients for various flow and pipe characteristics are essential for design purposes. Results of this work were presented as force coefficient graphs for different flow regimes. These graphs were approved to be included in the ASCE 7 Chapter 6. The CFD numerical model was developed and validated against the data obtained from the experimental study. Various turbulence models were tested and the Renormalization Group (RNG) k-ε model was defined as the most accurate Reynolds Averaged Navier-Stokes (RANS) turbulence model in predicting the induced forces. The numerical model allowed for testing the effect of a wider variety of parameters such as bed roughness and pipe diameter. Pipe diameter showed little influence on the impulse force magnitude at the time of bore impact in the tested diameters range. However, after the initial bore impact, force magnitude increased with increased pipe diameter. Numerical modeling results showed that increasing the bed roughness results in decreasing the induced forces on pipelines while pipe roughness showed no significant impact on the force magnitude.
Findings from this study characterized the effect of the tested parameters on the induced extreme hydrodynamic loadings on horizontal pipelines. Results of this study will assist in a better understanding of the phenomenon and the improvement of the currently available design guidelines.

Acknowledgement

I would like to express my greatest gratitude to my supervisors Professor Ioan Nistor and Professor Majid Mohammadian for their unconditional guidance and support throughout my PhD studies. PhD was a long journey and I couldn't accomplish that without the boundless support of my supervisors. Not only they were great academic advisors helping me with their professional and research expertise they were also outstanding personal mentors, their guidance and support in my personal life and through the ups and downs of this journey helped me to shape my future career.

I would also like to thank people who supported me to accomplish my PhD thesis. UOttawa's lab technician Mr. Mark Lapointe who was a great help in conducting the experiments at University of Ottawa. Dr. Jacob Stolle and graduate students (at the time) who helped me in conducting the experiments, Adrian Simpalean and Derek Eden. Professor Nils Goseberg for his valuable insights. Professor Shibayama who provided me the invaluable opportunity to conduct experiments in his lab at Waseda University in Japan. Dr. Takabatake and all the graduate students and staff at Shibayama lab who kindly helped me in conducting the experiments in Japan. I would like to acknowledge my committee members, Drs, Colin Rennie, Ryan Mulligan, Elena Dragomirescu and Amir Azimi for providing valuable suggestions and comments on my thesis. Special thanks to Dr. Bijan Dargahi for his continued support and encouragement.

I wish to thank my family whom I was lucky enough to have them close by during my studies and without their support I couldn't accomplish this. My beloved Mother who always encouraged me to peruse my educations, My caring sisters (Farnaz and Golnaz) my supportive brother (Farzad) and brother-in-laws (Navid and Ali) and my lovely nieces (Niki and Nila). Thanks to my Father, to whom I owe all I have achieved in my life. He is greatly missed and I regret he did not live long enough to see this.

Last but not least, I would like to thank my beloved husband Saber whom I actually met during my PhD studies. We came on a long journey together step by step as two PhD students working hard to build our life. He helped me technically when I needed a second pair of eyes and personally with his unconditional love and by supporting me in every way possible.

Table of Contents

List of Tables

List of figures

List of Symbols

σ	Surface tension [N/m]
ν	Kinematic viscosity [m^2/s]
$\emptyset$	Angle of stagnation [º]
e	Distance of pipe to bed [m]
ρ	Density [kg/m^3]
du/dt	Total acceleration [m/s]
ρ_s	Sea water density [kg/m^3]
∀	Volume below the water level [m^3]
h_w	Water depth [m]
F_s	Impulse force [N]
F_x	Total induced horizontal force [N]
C_R	Resistance coefficient [-]
F_L	Uplift force [N]
C_m	Inertia coefficient [-]
A_f	Area of the floor panel [m^2]
u_v	Estimated vertical velocity [m/s]
A	Average slope of the grade [1/m]
R	Ground elevation at the maximum tsunami penetration measured from the initial shoreline [m]
H	Impoundment depth [m]
T_0	Non-dimensional gate opening time [-]
D	Tailing water depth [m]
Δx	Distance between two wave gauges [m]
M	Momentum flux [J/$m^2.s$]
We	Weber Number [-]
F_H	Horizontal force [N]
F_z	Vertical force [N]
C_L	Lift coefficient [-]
Fr	Froude Number [-]
Kc	Keulegan-Carpenter number [-]
F_d	Drag force [N]

C_d	Drag coefficient [-]
F_i	Inertia force [N]
C_m	Inertia coefficient [-]
Re	Reynolds Number [-]
D	Cylinder diameter [m]
U	Freestream velocity [m/s]
F_h	Hydrostatic force [N]
p_c	Hydrostatic pressure [N/m^2]
A_w	Wetted area of the panel [m^2]
b	Width of the wall [m]
h_{max}	Maximum water height [m]
F_b	Buoyancy force [N]
kρ	Fluid density factor
I_{tsu}	Importance factor [-]

List of Abbreviations

ADV	Acoustic Doppler Velocimeter
ASCE	American Society of Civil Engineers
CCH	City and Country of Honolulu
CFD	Computational Fluid Dynamics
DOF	Degree of Freedom
LES	Large Eddy Simulation
SMBTR	Structural Design Method of Buildings for Tsunami Resistance
SPH	Smoothed Particle Hydrodynamics
VOF	Volume of Fluid

Introduction

1.1. Background

In recent years due to the growing devastating impacts of global climate change, the number of catastrophic natural hazards such as tsunamis and storm surges has increased significantly. In nature, the sudden release of a large amount of water may cause destructive extreme events. Below are examples of such events (Wüthrich 2018):

1. Dam break waves - produced by the sudden failure of a dam or natural reservoir.
2. Impulse waves - generated by a landslide falling inside a water reservoir.
3. Tidal bores - occur after a sudden increase in water depth during tidal activity.
4. Tsunamis - generated by an underwater earthquake.
5. Storm surges - caused by tropical cyclones with strong winds and high water levels.
6. Flash flood - caused by heavy rain associated with a severe thunderstorm, hurricane, tropical storm, or meltwater from ice or snow

Such extreme events can induce massive damage to nearshore infrastructures. It has been proven that properly designed structures can resist against extreme hydrodynamic events by reducing induced hydrodynamic loads (Kreibich et al., 2005). Such specific designs will help prevent social and economic disasters by saving lives and reducing reconstruction costs. Surveys along the western and northern coasts of Sumatra Island (Indonesia, 2004), central coast of Chile (2010) and in Tohoku, Japan (2011) show that infrastructures which were specifically designed to resist extreme events were able to save people's lives. Moreover, post-tsunami surveys showed that some structures resist better than others. Therefore, it is the engineers' responsibility to develop specific design features to mitigate the destructive effects of extreme events on coastal infrastructures.

a) Courtesy of Prof. Ioan Nistor

b) M.L. Bak / WikiCommons

Figure 1.1 Examples of resilient buildings designed according to specific recommendations to resist extreme events: (a) coastal structure designed as vertical shelter in Minamisanriku (Japan) after the 2011 Tohoku event (b) building in Bandah Aceh (Indonesia) after the 2004 Indian Ocean tsunami.

Different guidelines are available around the world for designing structures to withstand the extreme loads induced by extreme events. Among them are CCH (City and County of Honolulu Building code, Japan), SMBTR (Structural Design Method of Buildings for Tsunami Resistance, Japan), FEMA 55 (Federal Emergency Management Agency, USA). The risk for tsunami is also

high in North America and at the west coast due to proximity to Cascadia subduction zone (Clague et al., 2003; Park et al., 2013). In order to consider and mitigate the potential tsunami risk in America, the American Society of Civil Engineers (ASCE) has developed a new standard in the ASCE7- Chapter 6, focused on Tsunami Loads and Effects (Chock, 2016). The standard proposes design specifications for infrastructures resistance to extreme hydrodynamic loading based on the observations from previous destructive events such as the 2004 Indian Ocean and 2011 Tohoku Tsunami.

Pipelines in coastal areas are used for transmission of gas, oil or even wastewater and its discharge to the ocean waters. Installation of the pipelines in coastal areas is of great importance and different hydro-technical, mechanical and coastal engineering criteria along with economic and industrial issues, should be taken into consideration in the case of such developments. Pipelines are part of the critical infrastructure which are often placed nearshore and they must be hence designed to be protected against extreme events. For example, the submarine pipelines of the Pinghu oil and gas field in East China were damaged due to fatigue fractures caused by the combined action of waves and currents in 2000 (Zhao et al., 2019). Several submarine pipelines were significantly damaged during Hurricane Katrina (2005), in the Gulf of Mexico. (Fang et al., 2014).

a) *AP photo/ Steven Senne*

b) Coastal Municipalities Water Utility

Figure 1.2. Damaged pipelines by extreme events: a) Pipeline damaged due to Hurricane Katrina flooding, Louisiana b) Pipe damaged during the flood in Sheikh Rajleen, Palestine.

The American Society of Civil Engineers (ASCE), in its ASCE7 Chapter 6: Tsunami Loads and Effects, stresses the necessity to study tsunami loads on pipelines. Understanding the hydrodynamic forces acting on the pipelines is vital in ensuring their safe operation and avoiding potential damage to the environment. To address these issues, this study is the first of its kind to investigate loading on horizontal pipelines due to tsunami-like dam-break waves.

Dam-break waves are generated by the rapid opening of a vertical gate, causing an impounded volume of water to be released which results in an unsteady flow propagating in the downstream channel. (Wüthrich 2018). Based on the comparisons with field observations in Banda Aceh during the Indian ocean tsunami (December 2004), Chanson 2005 and 2006 suggest that dam-break waves are an appropriate method to reproduce inundations generated by extreme events such as tsunamis and impulse wave.

This thesis contains the following sections; in section 1, objectives, novelty, scope and contributions of the project are explained. Section 2, is a literature review of existing research in the area including the theoretical background in flow hydrodynamics around pipelines and available design guidelines for extreme hydrodynamic loading on structures. The gap in the literature and the need for novel research in the area is also explained in section 2. Section 3 explains the first part of the conducted experimental research with an emphasis on dam break wave hydrodynamics while section 4 explains the second part of the experimental work on the induced hydrodynamic forces analysis and force coefficient investigations. Sections 5 explains the Computational Fluid Dynamics (CFD) numerical modeling approach which complements the experimental study explained in sections 3 and 4. Section 6 is the summary of the conclusions derived from this research. Sections 7 elaborate recommendations for future work. The thesis ends with Appendices and the list of references used in conducting this research.

1.2. Thesis Objectives

The main goal of this study is to investigate the extreme hydrodynamic loading on pipelines under extreme transient flows. The study attempts to formulate recommendations and improve the current design standards present in the ASCE7 Chapter 6 for the assessment of loading induced by extreme flooding events on horizontally installed pipelines. Findings from this study will lead to the optimal design of pipelines located in tsunami and flood-prone areas, which will be both environmentally and economically safe during such extreme events. The overall objectives of the project consist of:

- Investigating dam-break flow hydrodynamics and its change in the presence of horizontal pipeline installed in its flow path.
- Investigating the effect of initial bed conditions, i.e., dry and wet bed, as well as initial flow conditions, i.e., different wave heights and still water depth, on induced forces on pipelines.
- Investigating the induced hydrodynamic forces on pipelines with respect to different pipe characteristics and installment conditions.
- Proposing force coefficients for various flow conditions and pipe configurations for optimal pipeline design.
- Investigating flow hydrodynamics and induced forces using numerical CFD modeling of the transient dam-break flow around the pipelines.

1.3. Novelty

Existing studies around hydrodynamic forces on pipelines deal mostly with the wave flow, including regular waves, breaking waves or steady current forces on the pipeline. This research aims to provide an understanding of the induced forces on pipelines due to extreme transient flow such as tsunami, storm surge and flood events. As such, the novelty of this project consists of:

- For the first time, a comprehensive study conducted to investigate flow hydrodynamics and induced hydrodynamic forces on horizontal pipelines caused by extreme waves such as tsunamis and storm surges generated using dam-break waves. This study was performed using a comprehensive experimental and numerical program.
- For the first time, this study makes concrete recommendations for drag and lift coefficients induced from extreme hydrodynamic conditions in different flow regimes. Force coefficient versus Froude number graphs were developed from the comprehensive experimental program covering the whole range of potential flow regimes during tsunamis and storm surges.
- The project presented here will provide the most comprehensive data set regarding loading on horizontal pipelines in extreme unsteady flow conditions. As numerical models continue to develop, the data provided by this study will aid in the validation and calibration of these models.
- In this project, for the first time, the transient dam-break wave flow hydrodynamics around the pipeline and the induced forces on the body of the pipes is modeled using CFD numerical modeling.

1.4. Scope of the thesis

The primary objective of this project is to analyze loading characteristics and to provide recommendations for the design of horizontal pipelines prone to extreme hydrodynamic events. The study focuses on providing this information through physical and numerical modelling. Due to time limitation and physical constraints of the laboratory:

- The study focuses on analyzing loading on horizontal circular cylinders from Swing gate generated dam-break waves. Other techniques of extreme wave generation, as well as different types of waves such as solitary or irregular waves, were not tested.
- The experiments were performed at a small scale (1:25). According to ASCE 7 Chapter 6, this is considered as the minimum acceptable scale for tsunami modeling in the case of individual structures. However, due to the limitations of the available laboratory facilities, this was the maximum scale that could be used in the present study.
- The physical modeling experiments did not include testing different pipe diameters or pipe surface roughness values. These parameters were tested and their impacts will be discussed in the numerical modeling section of the thesis.

1.5. Contributions

1.5.1. ASCE7 Chapter 6 proposal.

Proposed force coefficients and design specifications for horizontal pipelines resistance to tsunami waves. To be included in ASCE 7 guideline, chapter 6 on Tsunami Loads and Effect (Thesis: Appendix A).

1.5.2. Journal paper publications

Ghodoosipour, B., Nistor, I., Mohammadian, A. Modeling of hydrodynamic loading on pipelines. Submitted to Coastal Engineering journal, 2021. (Thesis: Chapter 5)

Ghodoosipour, B., Stolle, J., Nistor, I., Mohammadian, A. and Goseberg, N. Experimental study on extreme hydrodynamic loading on pipelines. Part 1: Flow hydrodynamics. *Journal of Marine Science and Engineering*, 2019, *7*(8), p.251. (Thesis: Chapter 3)

Ghodoosipour, B., Stolle, J., Nistor, I., Mohammadian, A. and Goseberg, N. Experimental study on extreme hydrodynamic loading on pipelines part 2: Induced force analysis. *Journal of Marine Science and Engineering*, 2019, *7*(8), p.262. (Thesis: Chapter 4)

Stolle, J., Ghodoosipour, B., Derschum, C., Nistor, I., Petriu, E., and Goseberg, N. Swing Gate Generated Dam-break Waves. *Journal of Hydraulic Research*. Taylor & Francis in-Press. 2018**.**

1.5.3. Conference publications

Ghodoosipour, B., Takabatake, T., Nistor, I., Mohammadian, M., Hamano, G., Ishii, H., Imura, K., & Shibayama, T. Transient dam-break wave loading on pipelines near sloping bed. ICCE, 2020, (36v), waves.p. 55. (Thesis: Appendix B)

Ghodoosipour, B., Stolle, J., Nistor, I., Mohammadian, M. and Simpalean, A.R. Loading on pipelines due to extreme hydrodynamic conditions. *ICCE*, 2018**,** (36), pp.4-4.

Ghodoosipour, B., Stolle, J., Nistor and I., Mohammadian. Experimental and Numerical Modeling of Hydrodynamic Loading on Pipelines due to Extreme Hydrodynamic Conditions. *CSCE Annual Conference*, Vancouver, British Columbia. 2017

2. Literature Review

Literature review of this thesis proposal is divided into two major sections of basics and fundamentals on flow behavior around and associated hydrodynamic forces on circular cylinders and extreme hydrodynamic loadings on structures.

2.1. Theoretical background

Lift and drag forces are the two major hydrodynamic forces on circular pipes induced by fluid flow. This phenomenon is influenced by various factors such as flow hydrodynamics around pipes, the effect of wall proximity and surface roughness, which should be investigated for a better understanding. This section provides a brief explanation of the basics and fundamentals utilized in the laboratory and numerical work of this research.

2.1.1. Hydrodynamics of flow around cylinder pipes

In order to understand the induced hydrodynamic forces on circular cylinders, one should understand the flow behaviour around the cylinder first. Flow characteristics around cylinder pipes is affected by the diameter of the pipe, fluid characteristics and velocity. Thus, a non-dimensional factor known as *Cylinder Reynold Number* has been defined as below to characterize flow around cylinder pipes:

$$Re = \frac{DU}{\nu} \qquad \text{(Eq. 2.1)}$$

Where D is the cylinder diameter, U is the freestream velocity and ν is the kinematic viscosity (i.e. fluid properties of density and dynamic viscosity). Flow characteristics around pipes vary with Reynolds number. Two different flow regions of *boundary layer, and wake region* are specified in figure 2.1. Wake region can be extended up to a lateral distance equal to D while boundary layer extends over a small thickness. The point where detachment of the boundary layer from a surface into the wake region happens is called separation point.

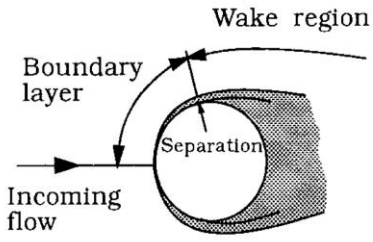

Figure 2.1. Definition sketch. (Adopted from Sumer and Fredsøe 2006)

The vortex shedding phenomenon from the circular pipes occurs at various Reynolds numbers. The flow around cylinder pipes have been divided into different regimes based on different Reynolds numbers, each of these regimes are discussed further in the following sections:

Creeping Flow, Re < 5:

In a low Re range, viscous forces dominate and the separation does not occur. Thus the flow is symmetrical around the pipe and no vortex shedding occurs (Figure 2.2).

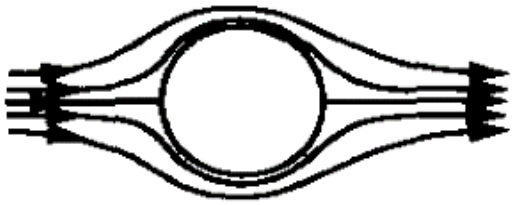

Figure 2.2. Creeping flow – Re < 5. (Adopted from Sumer and Fredsøe 2006)

Attached eddies, 5 < Re < 40:

This is the starting point of the flow separation. Symmetric vortices form the wake for cylinder and as the Re increases instability in the wake vortices increases until vortex shedding happens which causes the vortices to shed at cylinder sides. A circulation zone is formed which is composed of two oppositely located attached vortices (Figure 2.3).

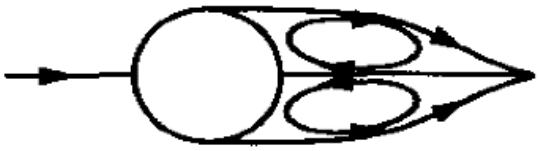

Figure 2.3. Attached eddies, 5<Re<40. (Adopted from Sumer and Fredsøe 2006)

Laminar and turbulent vortex shedding, 40 < Re < 350:

Increasing vortex shedding leads to further instability of the attached eddies. The unstable eddies start to oscillate in the shear layers. The oscillation increases with increasing Re until the sudden commencement of alternate vortex shedding. Shear layers are then rolled up into vortices shedding in the wake region. It should also be mentioned that vortex shedding until Re equal to 200 is laminar and after this point, vortex shedding changes from 2-D to 3-D in the region (Bloor 1964, Gerard 1978 and Wiliamson 1988) Figure 2.4.

Figure 2.4. Laminar 40 < Re < 200 and turbulent 200 < Re < 350 vortex shedding. (Adopted from Sumer and Fredsøe 2006)

Subcritical regime, 350 < Re < 3×10^5:

In subcritical regime, the wake is completely turbulent, but the boundary layer is still laminar. In this flow regime, the transition waves are rolled up into small-scale vortices. The small vortices are carried downstream by fully turbulent vortex shedding. Reynolds number increase, strengthens small-scale vortices (Figure 2.5).

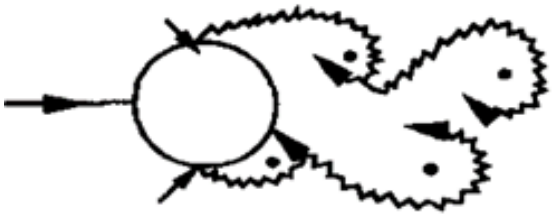

Figure 2.5. Subcritical regime, 350 < Re < 3×10^5. (Adopted from Sumer and Fredsøe 2006)

Critical regime, 3×10^5 < Re < 3.5×10^5:

In the critical regime transition to a turbulent boundary layer occurs after separation only at one side of the cylinder. Thus, the vortices are not symmetrical which causes a small lift force on the cylinder. The turbulent boundary layer changes sides resulting in lift force to change direction regularly. (Schewe 1983) (Figure 2.6)

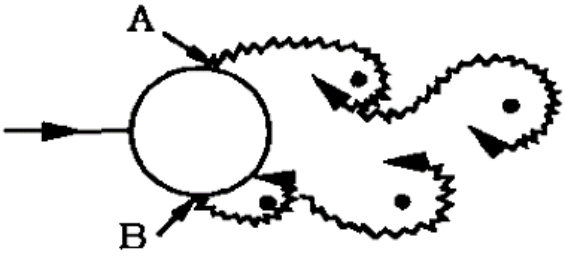

Figure 2.6. Critical regime, 3×105 < Re < 3.5×10^5. Laminar boundary layer with laminar boundary layer separation at point A and turbulent boundary layer separation at point B. (Adopted from Sumer and Fredsøe 2006)

Supercritical regime, $3.5\times10^5 < Re < 1.5\times10^6$:

In supercritical regime the flow around the pipe is symmetric with turbulent boundary layer separation and continuous bubble separation and attachment on both sides. In this regime, the boundary layer is partly turbulent and partly laminar. In supercritical regime, the drag force also starts to increase. (Figure 2.7).

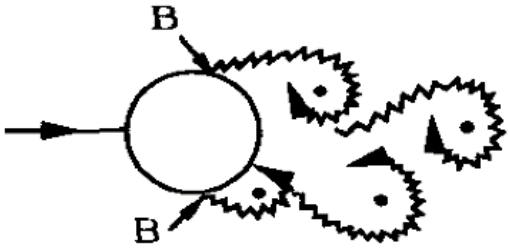

Figure 2.7. Supercritical regime, $3.5\times10^5 < Re < 1.5\times10^6$. At point B the boundary layer separation is turbulent and the boundary layer is partly turbulent and partly laminar. (Adopted from Sumer and Fredsøe 2006)

2.1.1.1 Flow around a pipe in the vicinity of a wall

In a marine pipeline, the gap between the pipe and the sea bed can critically influence the induced forces on pipelines. This gap might have been considered in the installation or may occur later after the installation of the pipeline. Flow and pipe interaction may lead to scour beneath the pipe. This may cause the pipe to suspend above the bed with a small gap, usually in the range from 0.1D to 1D (Sumer and Fredsøe 1989). Moreover, pipelines may be installed with a distance relative to the ground for different operational purposes. Therefore, it is important to understand the effects of such gaps in pipeline design criteria considering the changes in the flow and induced forces. Gap in the vicinity of a pipeline installation can affect the flow regime around the cylinder. Sumer and Fredsøe 1989 explains the change in flow regime in respect to the gap ratio as below:
1) When the gap ratios are smaller than 0.3 ($e/D < 0.3$; e is the gap between the cylinder and the wall), the vortex shedding suppression occurs. The suppression of vortex shedding is related to the asymmetry in the development of the vortices on the two sides of the cylinder. The free-stream-side vortex grows larger and stronger than the wall-side vortex. Hence, the interaction of the two vortices is largely reserved, resulting in partial or complete suppression of the regular vortex shedding.
2) Existence of the gap can affect the location of the stagnation point. In a gap ratio equal to one, the stagnation point is in the middle of the pipe with an angle of $\emptyset = 0°$. As the e/D is reduced to 0.1, the stagnation point moves downstream and closer to the bed $\emptyset = -40°$ (Figure 2.8) .

3) Considering the conditions in the above statement (No.2), the downward movement of the stagnation point in the presence of gap between the cylinder and wall, can also influence the angular position of the separation points. As shown in Figure 2.8, the separation point at the free-

stream side of the cylinder moves upstream while the wall side separation point moves downstream.

4) Lastly, the suction on the free-stream side of the cylinder is greater than on the wall-side.

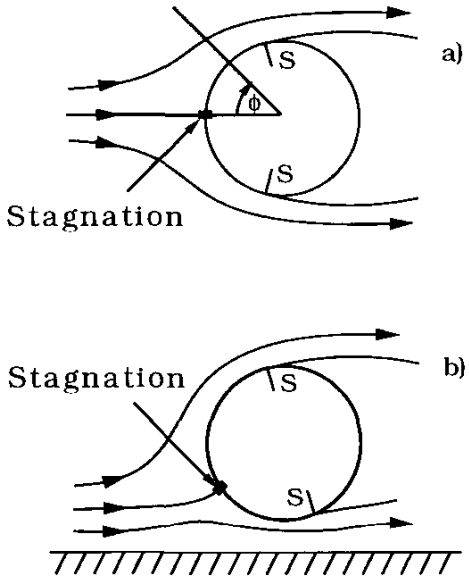

Figure 2.8. Comparison between flow around a) a free cylinder, b) a cylinder near a wall. S is the separation point. (Adopted from Sumer and Fredsøe 1989)

2.1.2. Drag and lift force

It was discussed in section 2.1.1. that the changes of the Reynold number will influence the flow regime around a pipe. As a result of a changing flow regime, the pressure distribution and consequently, the exerted forces around the pipe can also change. The vortex shedding which is a common phenomenon for conditions with Re > 40, leads to a periodic change of the pressure and force distribution around the pipe (Sumer and Fredsøe 1989). Previous experimental studies show that in a similar flow condition, the drag force oscillates periodically around the average drag force and a similar phenomenon occurs for lift force. Figure 2.9. shows the drag and lift forces calculated using the measured pressure distribution in an experiment by Drescher (1956) with Re = 1.1×10^5, D = 0.08 m and U = 1.53 $\frac{m}{s}$. It can be noticed from the figure that the drag force (in-line direction) changes periodically and oscillates around mean drag. There is also a non-zero lift force component in a transverse direction with zero mean which changes periodically with time.

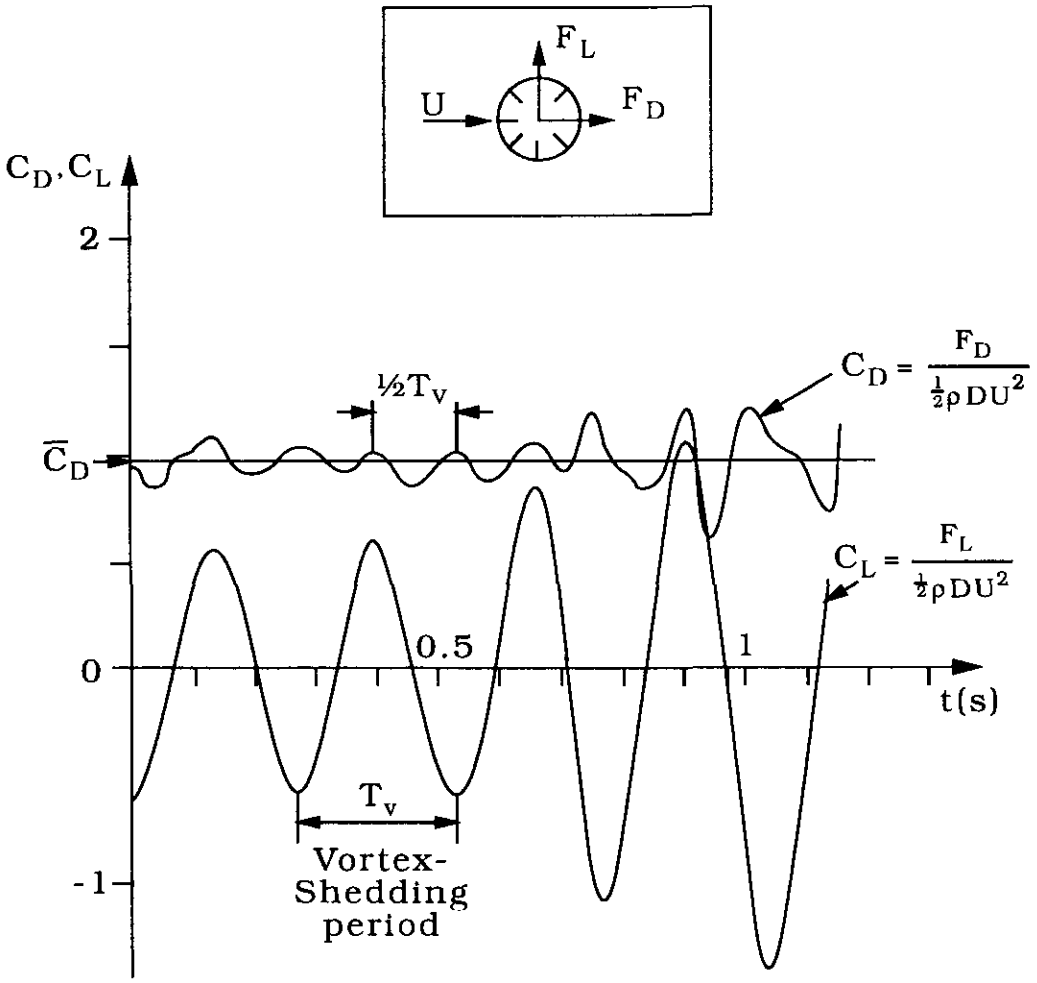

Figure. 2.9. Drag and lift force obtained calculated using the measured pressure distributions. *Adopted from* Drescher (1956).

In most cases friction drag (drag caused by the friction of fluid against the surface) is negligible and it can be assumed that total mean drag has only one component which is the form drag (the drag caused by specific shape of the object) as:

$$\bar{F}_d \cong \int_0^{2\pi} \bar{\rho} \cos(\emptyset)\, r_0 d\emptyset \qquad \text{(Eq. 2.2)}$$

Figure 2.10 presents the pressure distributions with different Re numbers while figure 2.11. shows the corresponding separation point location. As shown in figure 2.10, due to separation, pressure distribution is always negative at the rear side of the cylinder (wake region).

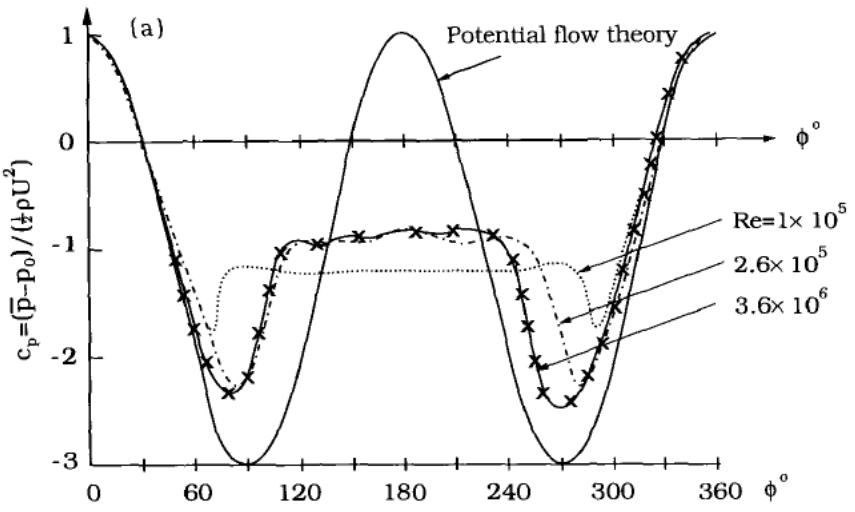

Fig. 2.10. Pressure distribution at different Re numbers for a smooth cylinder. Adopted from Abenbach (1968).

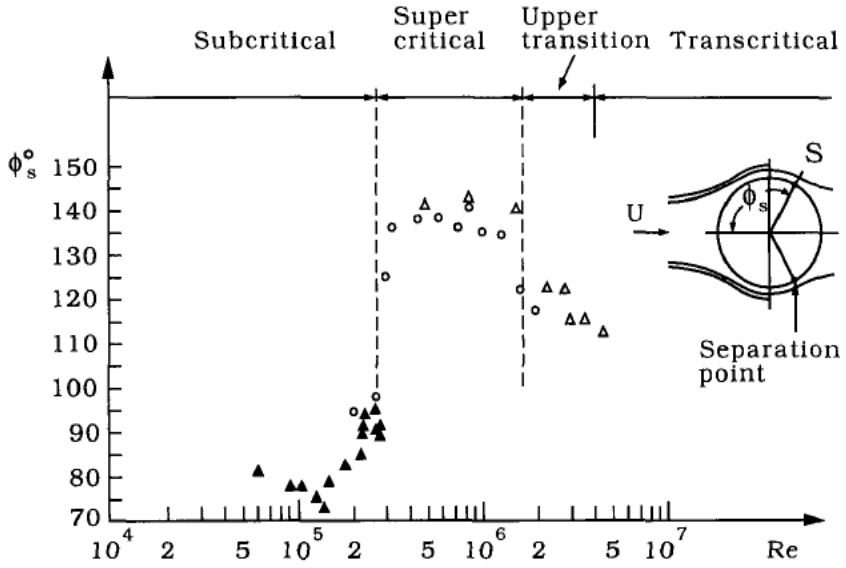

Fig. 2.11. Position of the separation point as a function of the Reynolds number for circular cylinder. Adopted from Abennbach (1968)

2.1.2.1 Drag Coefficient

Drag force can be written in a simple form as:

$$\frac{F_d}{\frac{1}{2}\rho\, D\, U^2} = C_D \qquad \text{(Eq. 2.3)}$$

In which C_D is called the drag coefficient and is a function of *Re*. Figure 2.12 plots the experimental data obtained in different flow regimes obtained by (Wieselsberger and Schew 1983) together with the laminar theory (Oseen-Lamb) and illustrates the change in C_D value by changing flow Reynolds number. Figure 2.13 illustrates C_D variation in the most common Re range i.e., $Re > 10^4$ obtained by Schew 1983.

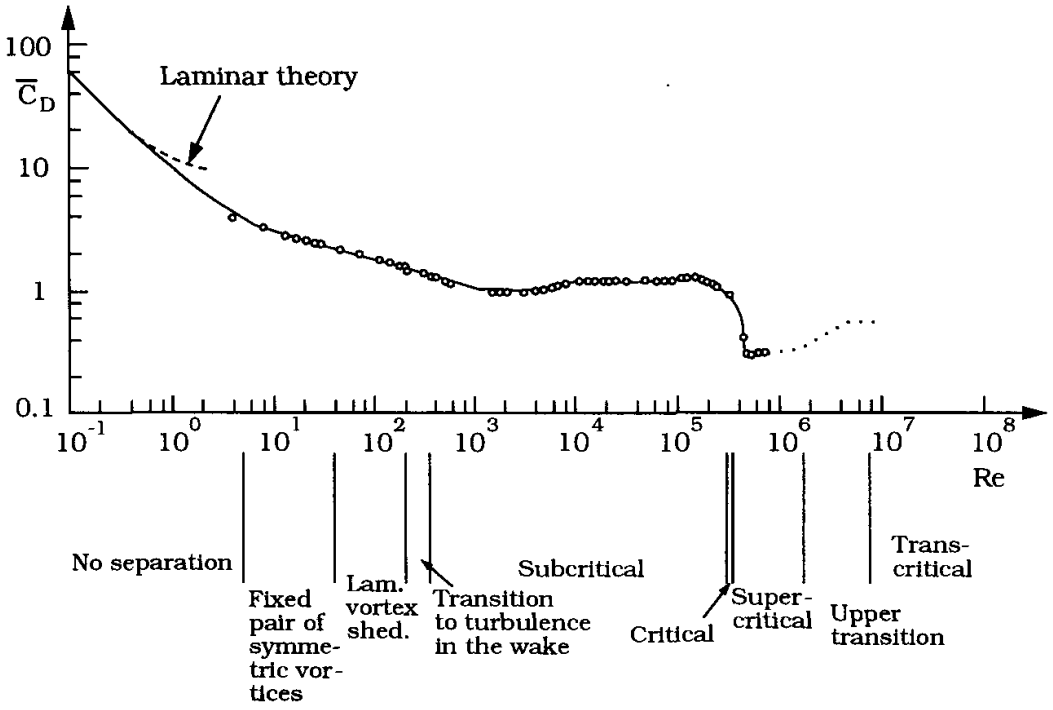

Figure 2.12. Drag coefficient as a function of the Reynolds number for a smooth circular cylinder. Measurements by Wieselsberger for $40 < Re < 5 \times 10^5$ and Schewe (1983) for $Re > 10^5$. Adopted from Sumer and Fredose 1989

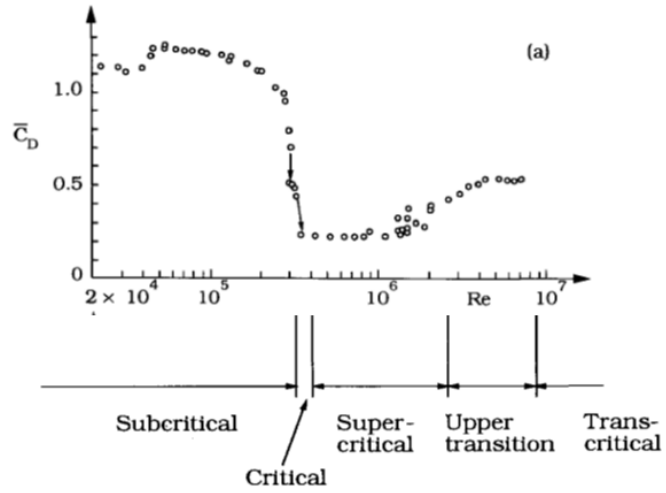

Figure 2.13. Drag coefficient as a function of *Re* for a circular cylinder for $Re > 10^5$. Adopted from Schewe (1983)

From Figure. 2.13, Sumer and Fredsøe 1989 argue that C_D decrease uniformly until *Re* = 300. However, after this point, C_D undertakes almost a constant value of about 1.2, throughout the subcritical *Re* range (300 <*Re* < 3 × 10^5). In the supercritical *Re* range (3.5× 10^5 <*Re* < 1.5 × 10^6) drag crises occurs, which is an extreme decrease in drag (C_D~0.25). Two of the diagrams, namely the one for *Re* = 1 × 10^5 (Threshold for subcritical flow regime) and that for *Re* = 8.5 × 10^5 (Threshold for supercritical flow regime) are reproduced in Figure 2.14. From the figure, Sumer and Fredsøe 1989 conclude that the drag should be smaller in the supercritical flow regime than in the subcritical flow regime. As shown in figure 2.14, the separation point moves from $\emptyset_s$ = 78° in subcritical flow (laminar separation) to $\emptyset_s$ = 140° in supercritical flow (turbulent separation). This change in the separation point location results in an exceptionally narrow wake with substantially smaller negative pressure, which leads to a considerable reduction in the drag.

As the flow regime changes from supercritical to upper-transition, the drag coefficient increases. As *Re* increases further to transcritical values namely *Re* > 4.5 × 10^5, drag coefficient remains constant at a value around 0.5.

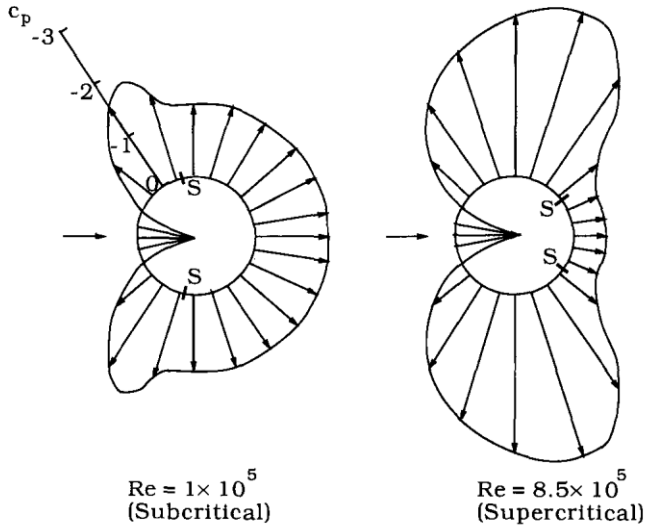

Figure 2.14. Pressure distributions and the location of separation point S in two different flow regime. Adopted from Achenbach (1968)

2.1.2.3 Forces on a cylinder near a wall

The changes in the flow caused by the wall proximity, discussed in Section 2.1.2 can potentially affect the forces acting on the cylinder. Changes of the flow regimes affect the pressure distribution around the pipe surface, Figure 2.15 illustrates the pressure distributions around a cylinder placed at three different distances from a plane bed (Bearman and Zdravkovich, 1978). In general, a decreasing gap ratio near the wall decreases the drag coefficient. This result is consistent with the pressure distributions given in Figure. 2.15.

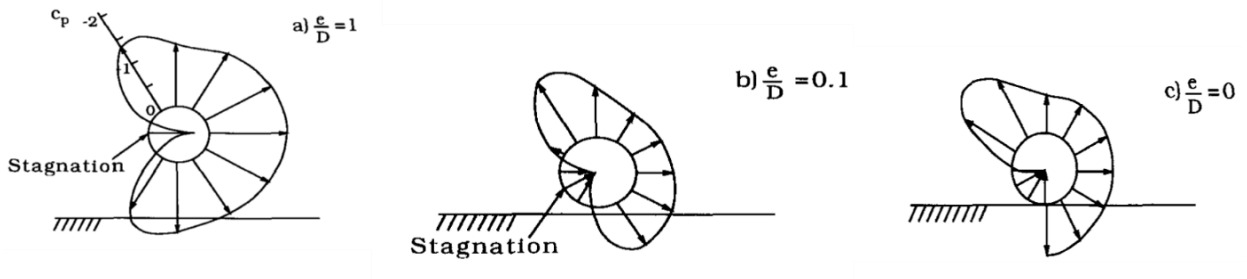

Figure 2.15. Pressure distribution on a cylinder near a wall at various gap ratios e/D. Adopted from Bearman and Zdravkovich 1978

The *e/D* ratio can significantly affect the flow regime around the pipe and consequently can influence the drag force. Increasing *e/D* up to a certain value leads to an increased C_D, However, it remains almost constant for further increase of *e/D* (Figure. 2.16). In a study by Zdravkovich 1985, it was shown that this behavior is related to the thickness of the approaching flow boundary layer. In large gap ratios, the cylinder is embedded fully in the potential flow region. At lower gap ratios, the cylinder is partially embedded in the potential flow region and partly in the boundary layer of the incoming flow.

Existence of the gap ratio will also result in an induced vertical force on the circular cylinder. Flow in the vicinity of a pipe is not symmetric; thus a non-zero lift force is expected. This is in contradiction with the free surface condition. In *e/D* = 1 condition, the mean pressure distribution around the cylinder is almost symmetric and thus, lift force is zero. However, when the gap ratios changes to e.g. *e/D* = 0.1, lift force starts to emerge (Figure 2.15). This lift force is in an opposing direction from the bed.

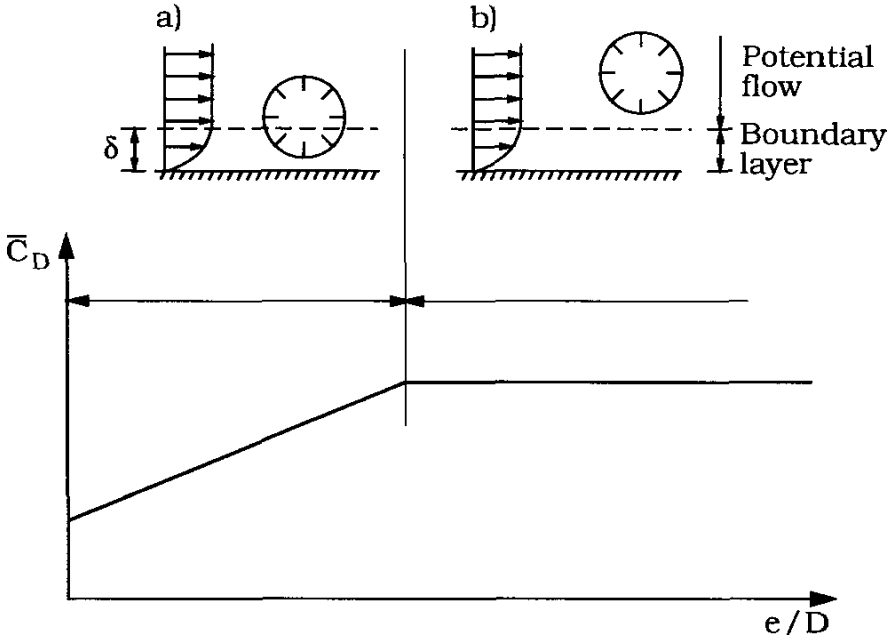

Figure 2.16. Drag coefficient as a function of gap ratio. Adopted from Sumer and Fredose 1989

2.1.2.4 Forces on a cylinder in unsteady flows

Regular waves are considered as unsteady flow. The unsteady flow interaction with a submerged solid body exerts force on the submerged body. The exerted force results both from the particle flow velocity and the flow acceleration. The drag force F_d exerted on the submerged body is due to frictional shear stress and normal pressure. This drag force can be defined as:

$$F_d = \frac{C_d}{2}\rho A u^2 \quad \text{(Eq. 2.4)}$$

An additional force exerted on the submerged body due to the accelerating flow is called inertia force and is defined as:

$$F_i = C_m \rho \frac{\pi D^2}{4}\frac{du}{dt} \quad \text{(Eq. 2.5)}$$

Where C_m is the inertia coefficient. For real flow past this Cylinder $C_m$values less than 2 are common.

Inertia force includes two components: First, an accelerating flow must have a pressure gradient, that produces a net force on the body, to be able to cause the flow to accelerate. The second component is the added mass of fluid that is produced when the flow passes the submerged body. Force is required to accelerate the additional mass of fluid caused by an accelerated body, also force will be induced on a still body by accelerating flow due to its added mass. The fluid density and acceleration, and the body shape and volume are the constituents of the second component of the inertia force.

For a circular cylinder with its axis oriented in a horizontal y or vertical z-direction and wave propagation normal to the axis, the force Fs per elemental length ds of the cylinder can be calculated using Morrison equation as:

$$F = \frac{F}{ds} = \frac{C_d}{2}\rho A u^2 + C_m \rho \left(\frac{\pi D^2}{4}\right)\frac{du}{dt} \quad \text{(Eq. 2.6)}$$

Where u is the particle velocity and $\frac{\partial u}{\partial t}$, is the local acceleration and is used as the total acceleration du/dt.

2.2. Research on hydrodynamic loading on pipelines

2.2.1. Loading on circular cylinders from unsteady wave flow

Many researchers have investigated the induced forces on horizontal pipelines by steady current flows or unsteady wave flows. Among them are comprehensive studies by Summer and Fredose 1989 on hydrodynamic forces on horizontal cylinders and by Sarpkaya and Isaacson 1981 on wave forces on cylinders.

Chaplin and Subbiah 1997, conducted an experimental work to investigate the induced forces and pressure distributions on horizontal cylinders from steady current without waves and with regular waves. They employed the results of their study to evaluate Morison equation formula in predicting loading forces on horizontal cylinders. As a conclusion, they found that the formula is most of the time accurate in predicting horizontal forces on horizontal cylinders. They also showed that forces on rough sections of the cylinder are approximately 20% larger than forces on smooth sections. Moreover, they showed that the obtained force coefficients for horizontal cylinders are similar to coefficients obtained for vertical cylinders and induced forces are insensitive to downstream wake and wave induced vortices around horizontal cylinders at moderate to high Keulegan–Carpenter number (K_C) numbers. Tong et al. 2017 investigated the flow hydrodynamics and the induced forces on horizontal submarine pipelines caused by currents using Large Eddy Simulation (LES) numerical modeling. They evaluated the drag coefficient values on cylinders placed close to the sea bed and concluded that drag force on the spanning side of the cylinder is slightly smaller. They also concluded that forces and pressure distributions alter due to the flow deflection from spanning to non-spanning sections of the pipe.

Flow hydrodynamics and induced forces on pipelines induced by regular and irregular waves have also been investigated by many researchers. Experimental studies such as Subbiah et al. 1991 and Geo et al., 2002, showed that pipe vibration generated by vortex shedding caused by pressure gradient around pipelines is larger in magnitude in irregular waves compared to regular waves.

Yukel and Narayanan 1994, carried out experiments to study wave forces on horizontal cylinders near seabed in wave transformation zone. Cnoidal wave theory was evaluated in investigating the flow behaviour and induced hydrodynamic wave forces, and it was proved to agree well with experimental results. In a similar study, Chevalier 2000, investigated the wave forces on a horizontal cylinder near a sloping seabed experimentally. The effect of wave shoaling was simulated using a slope of 1/20. Effect of different parameters such as the distance of pipe to bottom and water depth on induced forces were tested. Results from this study included the suggested force coefficients. The study also evaluated the classical models such as simple wave theory in force prediction and concluded that for low K_C numbers such models are capable of force prediction with acceptable accuracy. Mouaze and Belorgey 2003, investigated the vortices formation around near-bed cylinder from waves for different flow types, gap ratios and pipe

diameters. Results from this study show growing flow asymmetry and stronger vortex shedding downstream of the cylinder by increasing gap ratio.

Gao et al. 2015 investigated the induced drag and lift forces from the nonlinear wave groups on horizontal cylinders numerically and compared against forces induced by regular wave with the same wave height and period. They concluded that the forces from nonlinear wave groups are larger than forces from regular waves.

Bai et al. 2017, studied the wave-current interaction with horizontal cylinders with different submergence levels, both experimentally and numerically for small KC numbers (KC<4). Their experimental research was conducted using the combination of current and two regular waves with the same height and length and measuring the induced forces on horizontal cylinder. The numerical study was performed using Volume of Fluid method (VOF) to represent the free surface and RNG k-e model for turbulence modelling. The influence of wave reflection and wave blockage on induced forces for different cylinder submergence level was investigated and it was concluded that for partially submerged cylinders, wave reflection effect (which increases the force by increasing the wave height upstream of the cylinder) is more significant than wave blockage (which decreases the force by decreasing flow velocity and acceleration around cylinder). Therefore, the study showed that induced forces are larger than the predictions using Morison's formula for partially submerged cylinders. They also found that for the fully submerged cylinders, only wave blockage is influential; hence the forces are lower compared with Morison's formula.

2.2.2 Hydrodynamic loading on horizontal pipelines from extreme waves

An abundant number of research studies have been carried out to investigate the flow hydrodynamics around coastal and marine infrastructure caused by extreme events such as tsunamis or hurricanes. Haley et al. 2014, investigated loading on a slender horizontal cylinder from an extreme wave event represented with a very steep breaking wave. Results from this study show that as the wave approaches the breaking limit and wave steepness increases, the resultant vector of the drag and lift force components deviates significantly from the normal to the water surface direction. They showed that this force declination depends on the inundation depth upstream of the cylinder.

Solitary wave has been widely used as a typical wave model representing extreme events in literature for example Synolakis 1987, Liang et al., 2013, Hsiao and Lin 2010, Gedik et al., 2005, Goseberg et al., 2013. In these studies, hydrodynamics around circular cylinders prone to solitary waves has also been studied. For the first time, Sibley et al., 1982 investigated the horizontal force induced on horizontal cylinders from a solitary wave. The solitary wave in this study was reproduced manually using a rigid vertical barrier. Results showed good agreement between theoretical solutions and the measured forces on the rising side of the wave while on the falling side, the forces are lower due to separated eddies that form the drag force.

Xiao et al. 2013 investigated the interaction of solitary wave and uniform current and the associated induced forces on horizontal cylinder numerically using K-ε turbulent model. The model was validated using experimental data and solitary wave analytical solutions. Results show that the forces from combined wave and current are larger than linear sum of wave force and current force.

Aristodemo et al. 2017, investigated the induced forces from solitary waves on submerged horizontal circular cylinders both experimentally in a wave flume and numerically using a diffusive weakly compressible Smoothed Particle Hydrodynamics (SPH) model. Results show that inertia force is dominant and largely influence the horizontal and vertical force time history and the peak values in the range of wave characteristics tested, i.e., ($0.08<A/d<0.2$, $Re \cong 10^4$ and low KC numbers).

Although solitary waves are widely used, several researchers have identified important differences between waves generated during tsunamis and storm surges with solitary waves. Based on the field investigation during 2011 Tohoku tsunami, Chan and Liu 2012, showed that solitary wave's wavelength is significantly smaller than that of tsunami wave. Madsen et al. 2008 showed that considering geophysical scale, solitary waves are not good representatives of tsunami waves as the required evolutionary distance for an initial free surface hump into a solitary wave is larger than the width of existing oceans on earth. Qu et al. 2017, proved the tsunami waves to be more dangerous than solitary waves as they have higher run-up distance compared to solitary waves.

In regards to the induced hydrodynamic forces, Leschka and Oumeraci 2014, investigated the forces from both solitary waves and bores on three vertical cylinders with different arrangements numerically. Results show different wave heights upstream of the cylinders and different flow velocities in the vicinity of the cylinders. Istrati et al., 2018 experimentally investigated the loading on offshore bridge girder with cross-frames using both bores and solitary waves. Bore induced forces on the offshore girder showed a peak impulsive horizontal force at the time of bore impact. Force magnitude decreased immediately after the impact time and after the deck was flooded. However, in the case of solitary waves, the peak impulse force was not observed. In general, horizontal and vertical force patterns as well as the overturning moment were different between bores and solitary waves.

In a recently conducted research, Zhao et al. 2019 numerically investigated induced forces on submarine pipelines from solitary waves and a more realistic tsunami wave based on N-wave theory and according to the data derived from 2011 Tohoku tsunami in Japan. Tsunami wave was modeled by simulating a piston-type wave maker using a dynamic mesh and the wave profile was approximated using a combination of three $Sech^2$ wave profiles. The effects of different parameters such as wave height, water depth, pipeline diameter, and gap ratio on the hydrodynamic characteristics of submarine pipelines were investigated. Results indicate that the maximum hydrodynamic force induced by solitary waves are smaller than those generated by realistic tsunami wave. Moreover, the duration of the acting force under the tsunami-like wave is much longer than that of the solitary wave. It was also shown that under the tsunami-like wave,

increasing the wave height results in an increased induced hydrodynamic force on the pipeline while increasing the water depth causes the induced forces to decrease.

2.3. Extreme hydrodynamic loading on structures

Evaluation and estimation of induced hydrodynamic forces on structures is complicated. The scattered empirical and semi-empirical formulas available for defining the extreme hydrodynamic forces on structures in literature is a confirmation of the complexity of this phenomenon (Wuthrich 2018). The most widely used formula was suggested by Morison et al. (1950). As previously discussed in section 2.1.2.5 and shown in equation 2.6, Morison equation consists of inertia and drag forces. Yeh, 2007 suggests that since waves generated from extreme hydrodynamic events such as tsunamis and dam failures have extremely long waves, the inertia component is negligible except at the tip of the bore impacting structures, which is called impact force. Dias and Mallikarachchi 2006, considers three components of the total force induced on structures by extreme waves as hydrostatic, hydrodynamic and impulse force. Below is the definition of these three force components.

2.3.1. Hydrostatic force

Hydrostatic forces occur in the case of still or slow-moving water interacting with a fixed body. Federal Emergency Management Agency (FEMA, 2012) defines the hydrostatic force as:

$$F_h = p_c A_w = \frac{1}{2}\rho_s g b h_{max}^2 \qquad \text{(Eq. 2.7)}$$

where p_c is the hydrostatic pressure, A_w is the wetted area of the panel, ρ_s is the sea water density, g is the gravitational acceleration, b is the width of the wall, and h_{max} is the maximum water height above the base of the wall, at the structure location.

The vertical component of the hydrostatic force is the buoyancy force. For partially or fully submerged bodies, the buoyancy force is exerted on the centroid of the displaced volume. Buoyancy force in this case is equal to the weight of the displaced water and is given by:

$$F_b = \rho_s g \forall \qquad \text{(Eq. 2.8)}$$

where ρ_s is the sea water density, and $\forall$ is the volume of water displaced by the structure. $\forall$ will be calculated using the volume below the level of h_{max} defined in Equation 2.7.

2.3.2. Hydrodynamic force

Hydrodynamic force, also referred to as the drag force, is caused by fluid flowing around a structure. Structure geometry as well as flow characteristics and fluid density influence the hydrodynamic force. Drag force is a combination of pressure force from moving mass of fluid as well as friction forces from fluid flowing around the structure. The hydrodynamic force is exerted

on the centroid of wetted surface. FEMA suggests Equation 2.9, for calculating hydrodynamic force:

$$F_d = \frac{1}{2}\rho_s C_d B (h_w u^2)_{max} \quad \text{(Eq. 2.9)}$$

where ρ_s is the sea water density, C_d is the drag coefficient, B is the width of the structure in the plane normal to the direction of flow, h_w is the water surface elevation or the flow depth, and u is flow velocity at the location of the structure. C_d depends on both flow characteristics and the structure properties, such as shape and orientation. FEMA (2012) suggests a drag coefficient value as $C_d = 2$, while the recent update to the ASCE 7 standard (ASCE/SEI 7-16, 2017) suggests values based on the width to inundation depth ratio and type of structural component. Suggested C_d values in the ASCE/SEI 7-16 are in the range of $1.2 < C_d < 2.5$.

The component $h_w u^2$ in Equation 2.9 represents the momentum flux per unit mass per unit width. It must be noted that $(h_w u^2)_{max}$, which is the maximum momentum flux during a tsunami inundation wave, does not equal $h_{wmax} u^2_{max}$ which indicates that maximum depth may not occur at the same time instance as the maximum velocity and, therefore, the maximum momentum flux may happen any time during a tsunami event. Yeh 2007, defines the hydrodynamic force similarly and suggests the following formula to evaluate $(h_w u^2)_{max}$.

$$\frac{(h_w u^2)_{max}}{gR^2} = 0.125 - 0.325\,\frac{z}{R} + 0.11\,(\frac{z}{R})^2 \quad \text{(Eq. 2.10)}$$

Where R is the ground elevation at the maximum tsunami penetration measured from the initial shoreline, and z is the ground elevation of the location of interest.

Fujima et al. 2009 investigated the induced forces on buildings located at different distances from the shoreline. They suggested drag coefficient to be dependent on the distance of the building from the shoreline as:

$$C_d = 2 + 5.4\,(\frac{h_w}{D}) \quad \text{(Eq. 2.11)}$$

Where, D is the distance of the building from the shoreline. They conclude that for large $(\frac{h_w}{D})$ (buildings located close to the shoreline) induced forces are better represented by hydrostatic force formulas while for small $\left(\frac{h_w}{D}\right)$ (buildings located far from the shoreline), hydrodynamic force formulas are more appropriate.

Roberston et al., 2013, investigated the induced forces from an offshore solitary wave against a vertical wall. They suggested the following formula for calculating the induced hydrodynamic force, this equation was validated by field survey data by Chock et al. 2012;

$$F_{x,D} = \rho B\{\frac{1}{2}\, g h_w^2 + (h_w - d)U^2 + g^{\frac{1}{3}}.[(h_w - d)U]^{\frac{4}{3}}\} \quad \text{(Eq. 2.12)}$$

Where d is the still water depth.

2.3.3. Impulse Force

Impulse or impact force will act on a body when the leading edge of the bore contacts the structure. Different studies have focused on measuring and analyzing the impulse force. Among them, Nouri et al. 2010 investigated the extreme hydrodynamic loading on circular and rectangular buildings by measuring forces and pressure distribution along the height of the structure. They also tested different wave heights and concluded that the force caused by the initial bore impacting the structures is larger than the proceeding hydrodynamic force. They also proved the pressure distribution to be non-hydrostatic. Al-Faesly et al. 2012 performed similar investigations focusing on initial bed condition i.e., wet and dry. They concluded that impulse force at the time of bore impact is affected by the initial bed condition while the post-peak quasi-steady flow is independent of the bed condition and is similar in wet and dry bed conditions.

FEMA 2012 guideline refers to different studies such as Ramsden 1993 and Arnason 2005, and suggests the impulse force to be 1.5 times the hydrodynamic force in the case of structural wall elements:

$$F_s = 1.5F_d \qquad \text{(Eq. 2.13)}$$

Arnason 2005, carried out a comprehensive experimental program to investigate the interaction between free-standing structures and incident bore. The author tested different structures with different geometries. Results from testing different geometries are shown in Figure 2.17. As shown in the figure, an impulse force larger than the quasi-steady part of the force time-history was observed only for rectangular shaped structures and from waves with small heights. Arnason also tested circular columns with different diameters. Results show that impulse force for intermediate size circular column from large wave is more pronounced.

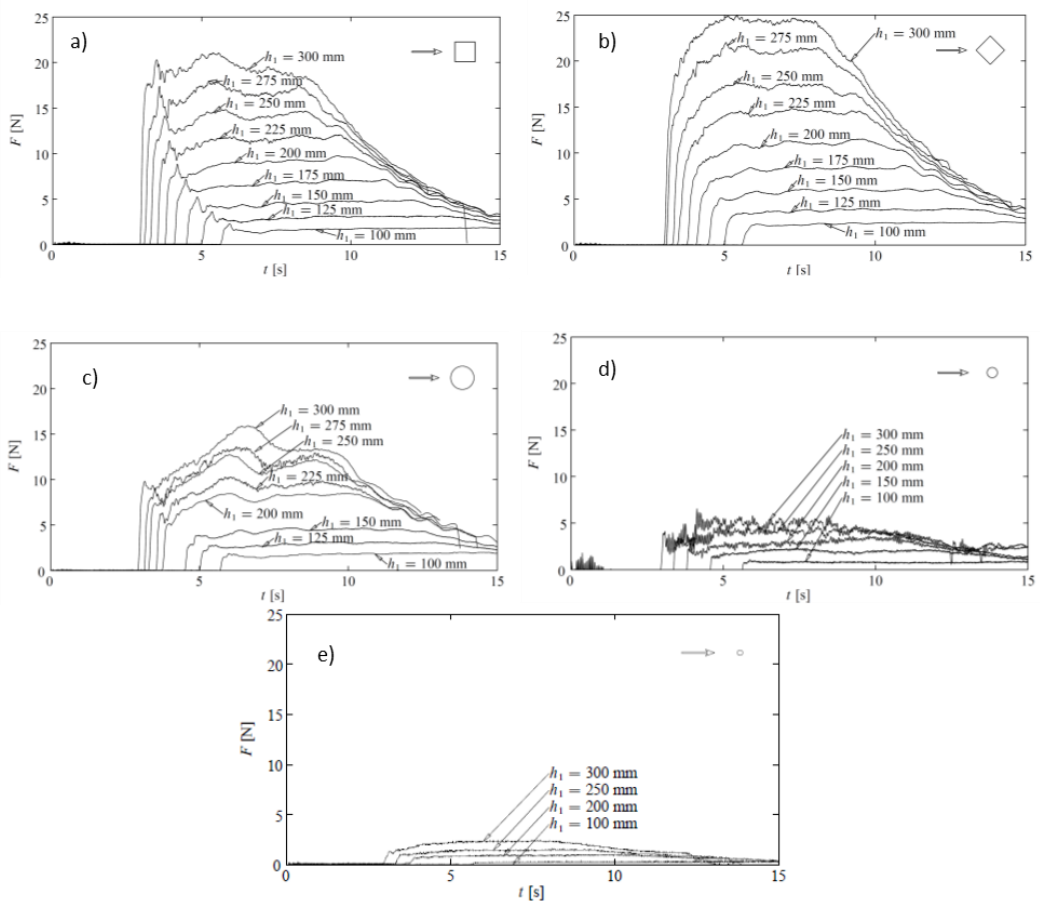

Figure 2.17. Force time history measured for various structure shapes. a) Rectangular column, b)Rectangular column with one corner facing the flow c) Large circular column, d) Intermediate circular column, e) small circular column. (Adopted from Arnason 2005)

In the case of horizontal components such as in pipelines, where the entire length of horizontal structure instantaneously collides with the rising wave, the impulse forces could potentially be significantly higher than the hydrodynamic force induced on the member when it is fully submerged even at the same flow velocity. Consequently, such forces will cause fatigue on the element as well as on the joints and may cause massive damage to the structure even in cases where the hydrodynamic force is larger than the impulse force (Prasad 1994). The very short duration involved makes the wave impact load a dynamic process, and the response of the member due to the load can change the magnitude of the forces. Furthermore, several factors can affect the impulse force rise time and consequently, the variation in the force magnitude. Air entrainment, cylinder roughness, and inclination are among the factors. (Prasad 1994).

Impulse force is usually followed by an increase in force magnitude as the bore flow accumulates in front of the structure, causing a “bulb-like” wake. This force has been named “run-up force” or “transient hydrodynamic force”. (Palermo et al., 2009).

Several studies, i.e. Gupta and Goyal 1975, for steady flow and Arnason 2005, for unsteady dam break flow, suggested a term called "Resistance coefficient (CR)" instead of drag coefficient for the horizontal force coefficient due to the contribution of the hydrostatic and impulse force in addition to the hydrodynamic force. It is often too complicated to differentiate between different force components which makes the need for a new force coefficient as Resistance coefficient. Arnason 2009, defines Resistance coefficient as:

$$C_R = \frac{2.F_x}{\rho B h u^2} \qquad (2.14)$$

Where F_x is the total induced horizontal force. Unlike drag coefficient C_d, C_R is a function of time rather than a constant value.

2.3.4. Uplift Forces

Uplift forces are usually exerted on elevated surfaces that are submerged during tsunami inundation waves. In fact, water rises remarkably fast during a tsunami which will induce uplift to the bottom surface of elevated horizontal components. This uplift force will add to the hydrostatic buoyancy force. FEMA P-646 suggests a formula for computing the uplift force as:

$$F_L = \frac{1}{2} C_L \rho_s A_f u_v^2 \qquad (2.15)$$

where C_u is the lift coefficient and ρ_s is the fluid density. FEMA (2012) suggests C_u to be taken as 3.0. A_f is the area of the floor panel, and u_v is the estimated vertical velocity component or the rate at which water is rising. The guideline suggests u_v to be calculated as:

$$u_v = u \tan \alpha \qquad (2.16)$$

where u is the horizontal flow velocity and α is the average slope of the grade.

For slabs submerged during tsunami inflow, ASCE/SEI 7-16 (2017) suggests to consider a minimum hydrodynamic uplift pressure of 20 psf (0.958 kPa) applied to the soffit of the slab.

Above mentioned force components can be used in the case of dam break tsunami-like waves impacting horizontal circular cylinders or pipelines, which is the focus of current study, and will be explained in the following sections.

2.4. Design codes

Several design codes are being used across the world for safe and efficient design of the coastal structures which are resistant to extreme loads from extreme events such as tsunamis and storm surges. Below are some of these codes which are being used in different tsunami prone areas:

1. CCH - City and County of Honolulu Building Code, Chapter .16, Article 11. (2000). CCH was developed by the Department of Planning and Permitting of Honolulu, Hawaii. The code was developed on the basis of the study by Dames and Moore (1980) and suggests

the summation of hydrostatic, hydrodynamic and surge forces. This code suggests the velocity to be equal to the height (v = h). Surge force is quantified using:

$$F_s = \int_0^{3h_{max}} \rho g B\ (3h_{max} - z)dz = \frac{1}{2}\ \rho g B\ (h_{max})^2 = 4.5\ \rho g B h_{max}^2 \qquad (2.17)$$

Where z is the ground elevation of the location of interest.

2. FEMA 55 – Federal Emergency Management Agency, USA (2011). FEMA suggests neglecting the surge force component (FS). The hydrodynamic force is computed using Equation 2.9. This standard estimates the flow velocity by (v =$2\sqrt{gh}$).

3. SMBTR – Structural Design Method of Buildings for Tsunami Resistance. This code is

developed by the Building Centre of Japan and it is based on the research conducted by Asakura et al. (2000), Okada et al. (2005) and Nakano (2008). Following CCH recommendation Equation 2.17 was used to quantify the surge force for buildings without overflow. The code recommends using separate equation for buildings with overflow as:

$$F_{x,D} = \frac{1}{2}\ \rho g B\ (6h_{max} -\ H_B).H_B \qquad (2.18)$$

Where, H_B is the height of the building.

4. Washington State Department of Natural Resources for tsunami vertical evacuation buildings standard. These guidelines are based on the studies by Yeh et al. 2005.

5. ASCE-7 standard in its 2016 edition entitled "Minimum design loads for buildings and other structures" introduced a specific Chapter 6, "Tsunami loads and effects" (ASCE7-06, 2016; Chock, 2016; Robertson, 2016). This standard categorizes buildings based on their importance in resisting against tsunami. Standard suggests the maximum hydrodynamic loads to occur for the Load Case 2, when $h = \frac{2}{3}h_{max}$, assuming a conservative Froude number of $\sqrt{2}$:

$$F_{x,D} = 1.5.\frac{1}{2}\ k_\rho \rho\ I_{tsu} C_d B\ (hv^2)_{max}\ \rightarrow\ F_{x,D} = k_\rho \rho\ I_{tsu} C_d B\ h_{max}^2 \qquad (2.19)$$

where k_ρ is fluid density factor taking into account the effect of soil and debris (typically k_ρ = 1.1), ρ is flow density, (ρ = 1000 kg/m3), I_{tsu} is the importance factor, and C_d is the drag coefficient, herein C_d = 2 . According to ASCE 7 Chapter 6, the wave velocity is computed using:

$$v = \sqrt{2}\,.\sqrt{g.\frac{2}{3}\ h_{max}} \qquad (2.20)$$

If a more conservative approach is used, then Eq. 2.19 becomes:

$$F_{x,D} = 1.6.\,k_\rho \rho\ I_{tsu} C_D B\ h_{max}^2 \quad (2.21)$$

ASCE 7 Chapter 6 also suggests using the Eq. 2.12 suggested by Robertson et al. (2013).

2.5. Discussion and Research needs

Literature review presented in previous sections focuses on existing research conducted around the topic of a) flow hydrodynamic around horizontal pipelines in steady and unsteady wave flows as well as extreme hydrodynamic loading on horizontal pipelines. and b) research and available formulations and guidelines around extreme hydrodynamic loading on buildings and coastal infrastructure. This chapter illustrates some gaps in knowledge and the need for further investigations that motivated the current research as following:

1. Despite many analytical, numerical and experimental research works that focus on horizontal circular cylinders subjected to current flows or regular and irregular waves, little attention has been focused to address the impact of extreme transient flows in extreme events such as tsunamis and storm surges on horizontal cylinders. As described in section 2.2.2, a few research articles investigated flow hydrodynamics and associated induced forces during extreme events using solitary waves. However, solitary waves proved not to be a suitable wave model for real-world extreme events such as tsunamis.
2. Relatively comprehensive research works have been conducted around the topic of extreme hydrodynamic loading on buildings and vertical structures with different characteristics. Different guidelines and design codes have made recommendations for safe design of structures to resist extreme events in coastal areas. There is a gap in the literature as for the design recommendations of horizontal pipelines prone to extreme events such as tsunamis. ASCE 7, chapter 6, has explicitly expressed the need for research around extreme hydrodynamic loading and design recommendations for horizontal pipelines.
3. Existing research contains a wide range of recommendations for force coefficients for different types of structures, including horizontal cylinders from steady currents and unsteady regular and irregular waves. Research is also available on force coefficient recommendations for vertical structures in the case of extreme hydrodynamic events with different wave characteristics. There is a gap in the literature as for suggestions on force coefficients in the case of extreme events impact on horizontal pipelines in different flow regimes.

4. Similar to the experimental investigations, many researchers have studied hydrodynamics around horizontal cylinders impacted by steady flows, linear, non-linear and solitary waves. Such research has been conducted using different numerical modeling methods such as SPH and CFD. However, there is a gap in the literature on numerical investigation of extreme tsunami-like waves hydrodynamics and induced forces on horizontal cylinders.

3. Experimental Study on Extreme Hydrodynamic Loading on Pipelines Part 1: Flow hydrodynamics[1]

Abstract: Over the past two decades, extreme flood events generated by tsunamis or hurricanes have caused massive damage to nearshore infrastructures and coastal communities. Utility pipelines are part of such infrastructure and need to be protected against potential extreme hydrodynamic loading. Therefore, to address the uncertainties and parameters involved in extreme hydrodynamic loading on pipelines, a comprehensive experimental program was performed using an experimental facility which is capable of generating significant hydraulic forcing, such as dam-break waves. The study presented herein examines the dam-break flow characteristics and influence of the presence of pipelines on flow conditions. To simulate conditions of coastal flooding under tsunami-induced inundation, experiments were performed on both dry and wet bed conditions to assess the influence of different impoundment depths and still water levels on the hydrodynamic features.

3.1. Introduction

3.1.1. Background

Recent devastating tsunami and storm surge events exposed the vulnerability of coastal communities to such extreme natural disasters. The number of people experiencing such catastrophic coastal flood events has been compounded by climate change and the ever-increasing urbanization of low-lying coastal areas all around the world (Nicholls 2004). This provided increased interest for research around the topic of extreme impacts on infrastructure. The need to study the hydrodynamic loading induced by such events and its effects on various structures is important. Coastal-induced inundation, due to tsunamis, hurricanes, and associated storm surges, can generate extreme turbulence, which impacts coastal areas and destroys infrastructures in their path. Moreover, sudden dam failure incidents can also cause similar impacts to vulnerable downstream infrastructures (Cao et al. 2011). Understanding the dynamics of highly turbulent waves, and transient flows, as well as their interaction with structures, is complex and difficult to assess and quantify. This is among others, due to their highly non-linear and rapidly transient characteristics, and the common involvement of turbulent multi-phase processes (Prasad 1994). Several researchers have conducted post-event forensic field surveys of the recent catastrophic events, such as the 2004 Indian Ocean and the 2011 Tōhoku Tsunami. Field survey results after the 2004 Indian Ocean Tsunami conducted in Khao Lak, Thailand, estimated coastal inundation heights between 4 to 7 m (Matsutomi and Okamoto 2010, Dias et al. 2006) and wave front celerities between 6 and 8 m/s (Rosseto et al. 2007). Data recorded by the Japanese Port and Airport Research Institute (PARI) after the 2011 Tōhoku Tsunami in Japan showed inundation depths of up to 15 m in the city of Onagawa. During the same event, onshore inundation velocities

[1] A modified version of this section has been published as: Ghodoosipour, B., Stolle, J., Nistor, I., Mohammadian, A. and Goseberg, N. Experimental study on extreme hydrodynamic loading on pipelines. Part 1: Flow hydrodynamics. Journal of Marine Science and Engineering, 2019, 7(8), p.251.

of up to 10 to 13 m/s were also observed near Sendai Airport (Jaffe et al. 2012). Fritz et al. 2012 used video-processing of images filmed in Kasennuma Bay during the 2011 Tōhoku Tsunami and estimated inundation depths up to 9 m, flow velocities of up to 11 m/s and calculated Froude number values around 1. Field and numerical modelling of the 1993 Hokkaido-Nansei-Oki Tsunami revealed water depths of 5–15 m and flow velocities of 3–15 m/s. Results from such detailed surveys provide invaluable sources of hydrodynamics data for further analysis and comparison with experimental data or available analytical or empirical formula.

Several studies attempted to characterize the hydrodynamics of tsunami run-up on coastlines and its interaction with structures subjected to a solitary wave as a representative of the tsunami (Limura and Norio 2012, Synolakis 1987, Gedik et al. 2005, Hsiao and Lin 2010). Aristodemo et al. 2017 conducted a small-scale experimental study in a wave flume along with a numerical investigation using a smoothed-particle hydrodynamics (SPH) model. In their study, they investigated the induced loading from a solitary wave on a horizontal circular cylinder. Although solitary waves have been extensively used for tsunami-related studies, more in-depth studies have shown that such waves cannot represent real tsunamis properly, due to the discrepancies, such as difference in wave period, and height during the wave run-up (Madsen and Schaffer 2010). Madsen et al. 2008 concluded that the required evolutionary distance for an initial run-up into a solitary wave is well beyond the width of any oceanic dimension, concluding that solitary waves would not represent real tsunamis. Chan et al. 2012, referred to the available data from the 2011 Tōhoku tsunami and concluded that the wavelength for real tsunami is significantly longer than for solitary waves generated in the laboratory.

Several studies tried to compare the different characteristics of solitary waves and a more realistic representative for tsunami-like waves, such as “bores”. Leschka and Oumeraci 2014 investigated numerically the induced hydrodynamic forces from two different types of waves, namely solitary waves and bores, representing tsunamis, on three vertical cylinders with different arrangements. They concluded that two different waves result in different flow hydrodynamics, i.e., wave height and flow velocity. Istrati et al. 2018 investigated the different types of tsunamis, i.e., solitary waves and bores, and their effect on I-grider bridge with cross-frames. They characterized the induced forces from a bore as short-duration impulsive horizontal force at the time of bore impact that is followed by a smaller magnitude and longer duration forces. This was not observed in the case of solitary waves. Such findings emphasize the importance of choosing the correct type of tsunami representation for characterizing the induced forces on structures, especially for long waves. They also indicate that the unbroken solitary waves are not suitable wave models representing tsunamis.

Zhao et al. 2019 studied the hydrodynamic properties of submarine pipelines under the impact of several widely used waves representing tsunamis, including solitary waves and N-waves with characteristics closer to a real tsunami. This study suggests that the hydrodynamic characteristics of the waves, such as water level, flow velocity, flow structure and induced forces in these methods are largely different. Moreover, the longer periods in tsunami-like waves causes a smoother water surface profile compared to solitary waves with shorter periods. As the wave passes the pipe, the size of the vortices generated downstream of the pipe in a solitary-wave is smaller than the vortices generated by tsunami-like waves. Moreover, by the time the wave passes the pipe, the wave height decreases faster for solitary waves as compared to tsunami-like waves, which in turn reduces the induced forces, as well as the duration of the acting force.

In summary, in this study, dam-break waves were used for studying the tsunami-like impact on pipes. Several researchers, i.e., Chanson et al. 2003 and Chanson 2006, have characterized such waves and stated that dam-break waves could represent real tsunamis.

In this study, where the assessment of tsunami-induced coastal floods on pipelines is addressed, a dam-break wave generated using a rapidly-opening swing gate was used to reproduce the highly turbulent flow conditions created during such extreme events. Stolle et al. 2018 described details of the discussed dam-break waves. Several researchers characterized dam-break waves surging over a dry bed. Among them, Ritter 1892, Henderson 1996 and Chanson 2005 developed solutions for the dam-break wave profile. The effect of bed condition (i.e., dry and wet bed) has also been the subject of several studies. Chanson et al. 2003 performed an experimental study on tsunami characteristics on wet and dry horizontal beds. They characterized wave momentum and wave front velocity at the beginning of the wave propagation in tsunamis and compared them to the classical dam-break waves. Wuthrich et al. 2018 proposed a new method to generate bores over dry and wet bed conditions and investigated the influence of different parameters of the wave, such as the bore front celerity and the flow velocity profile. Moreover, studies, such as St. German et al. 2013 and Douglas and Nistor 2015 have investigated the effect of bed condition on tsunami characteristics numerically.

Several other researchers investigated the impact of dam-break and tsunami on structures. Nouri et al. 2010, Al-Faesly et al. 2012, Bremm et al. 2015 and Foster et al. 2017 evaluated the forces induced from tsunami-structure interaction under unsteady conditions. Other studies such as Wüthrich et al. 2018a and 2018b investigated the extreme hydrodynamic forces induced on buildings with various characteristics. Arnason 2005, studied the interaction between an incident bore and a free-standing structure and focused on analyzing flow hydrodynamics in their presence. Goseberg et al. 2014, studied different flow characteristics around vertical obstacles impacted by transient tsunami-like long waves. Studies, such as Araki and Deguchi 2011, Mazinani et al. 2014, and Chen et al. 2017, investigated tsunami bore impact on coastal bridges.

An in-depth review of existing research in the context of extreme flow condition impact on different structures reveals a lack of investigations on the impact of transient tsunami-like waves on horizontal pipelines. The American Society of Civil Engineers (ASCE), through its ASCE7 Tsunami Loads and Effects Committee, has developed a new standard for tsunami impacts and loading (Chock 2016). Amongst the potential effects of such extreme events on infrastructure, this standard has emphasized the need to investigate tsunami loads on pipelines. The work presented herein is the first of a two-part paper which focuses for the first time, to the knowledge of the authors, on the impact of tsunami-like dam-break waves on submerged and above-ground horizontal pipelines on wet and dry bed conditions. Part 1, focuses on the free-stream flow hydrodynamics and its alterations in the presence of a pipe impacted by such a flow. Part 2 (Ghodoosipour et al. 2019b) focuses on the hydrodynamic loading and associated force coefficients for horizontal pipelines located in coastal areas prone to tsunamis.

3.1.2. Objectives

The main goal of this study is to investigate the extreme hydrodynamic loading on pipelines under transient flows. The specific objectives of this first part of the two-part paper are to investigate and discuss the flow hydrodynamics of the dam-break waves and movement and

impingement on a pipeline installed in its flow path. The following specific questions were examined in this study:

- What are the flow characteristics (time-history of the wave surface profile and flow velocity) for dam-break waves propagating over dry bed conditions for different wave heights?
- How are flow characteristics altered in the case of dam-break wave propagation over wet bed (still water on the flume bed, downstream of the impounding gate) and how are these characteristics changing when the dam-break wave height changes and/or when the still water depth of the wet bed varies?
- How do flow conditions get influenced by the presence of a horizontal cylindrical pipe immersed in the flow under both dry and wet bed conditions?

Results from this first paper will be further used to analyze and discuss the complex behavior of the hydrodynamic loading exerted on the pipe: In the companion paper (Ghodoosipour et al. 2019b).

3.2. Experimental setup

3.2.1. Dam-break flume

A comprehensive experimental program was developed and conducted in the Dam-break Flume in the Hydraulics Laboratory at the University of Ottawa, Canada. Experiments were performed at a 1:25 length scale, under Froude similitude. The flume is 30.1 m long, 1.5 m wide, and 0.5 m high. A predetermined volume of water was impounded behind a rapidly-opening swing gate installed in the flume to form an upstream reservoir with a length of 21.55 m and variable water depths. The dam-break waves were generated by the rapid opening of the swing gate. According to a previous study conducted in the same flume by Stolle et al. 2018, the non-dimensional gate opening time, $T_0 = (t\sqrt{g/h})$ (t being the gate opening time, h being the impoundment depth), is dependent on h with an approximately linear relationship as:

$$T_0 = 1.47–1.19\,h \qquad \text{(Eq. 3.1)}$$

With the range of impoundment depths tested in this study, the non-dimensional gate opening time was in the range of $0.875 < T_0 < 1.113$. Therefore, the range of T_0, satisfied the criterion for acceptable non-dimensional gate opening time $T_0 < 1.41$ defined by Lauber and Hager 1998. A vertically-moving steel gate located at the downstream end of the flume ensured the control of the water level downstream of the swing gate and enabled, thus, the formation of wet bed conditions with different water depths. The tested pipe model was made of cold-rolled steel, 0.10 m in diameter and 1.47 m in length, installed horizontally and transversally across the flume at x = 5.60 m downstream of the gate. The pipe was designed to be perfectly rigid with very high natural frequency in order to avoid possible dynamic effects. Schematics of the flume, together with various experimental parameters, are shown in Figure 3.1.

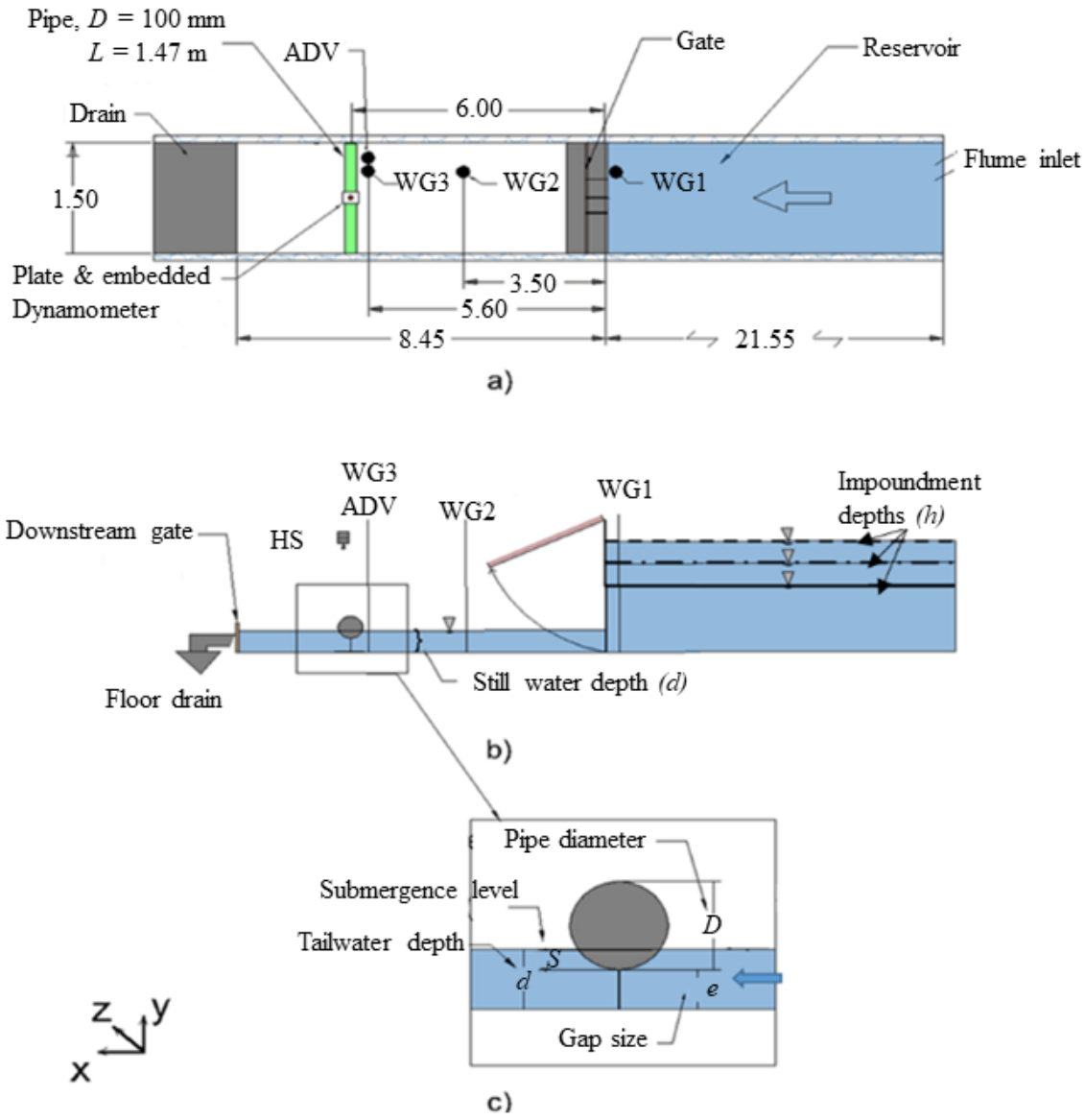

Figure 3.1. Flume and instrumentation sketch, (unless otherwise specified, all dimensions are in m). (**a**) Plan view, (**b**) side view and (**c**) close view with pipe and experimental parameters.

3.2.2. Instrumentation

Figure 3.2a,b show images of the flume together with the instruments and their locations. x = 0 was defined at the longitudinal position of the gate.

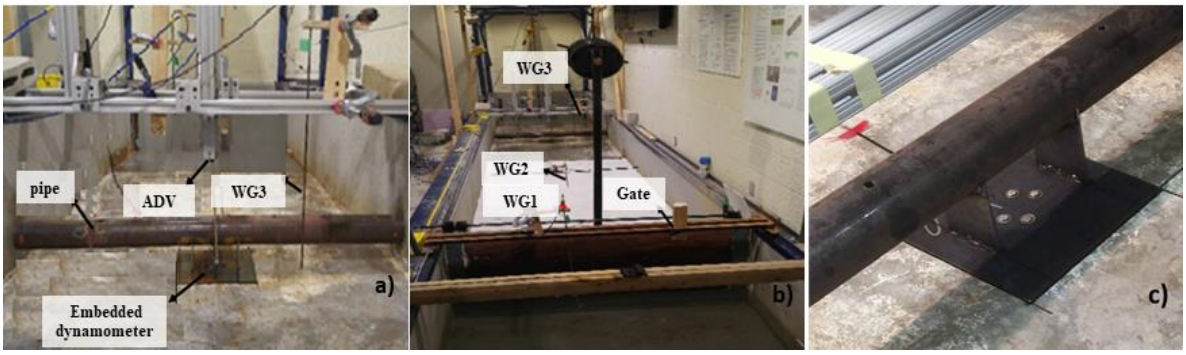

Figure 3.2. (**a**) Downstream view of pipe, dynamometer, ADV and wave gauge, (**b**) downstream view of flume and gate and (**c**) close view of pipe, supports and the base plate.

3.2.2.1. Wave Gauges

To record the time-history of the water level, three wave gauges (RBR WG-50, capacitance-type, ±0.002 m accuracy, RBR Global, Ottawa, ON, Canada) were installed at different locations along the flume. The first wave gauge (WG3) was installed upstream of the gate ($x = -0.04$ m) and was used to determine the opening time of the gate. The instant when the reservoir water level started to decrease, which was recorded by WG1, was used to synchronize the other measurement instruments The other two wave gauges were located at $x = 3.5$ m (WG2) and $x = 5.6$ m (WG1) downstream of the gate. The wave gauges sampling rate was 300 Hz. Wave gauges were calibrated by ensuring a linear gauge response with R^2 values greater than 0.99.

3.2.2.2. Acoustic Doppler Velocimeter (ADV)

A high-resolution acoustic Doppler velocimeter (ADV) (Vectrino, ±1 mm/s accuracy, 2.5 m/s measurement range, Nortek, Norway) was used for velocity measurements in the free stream flow. The velocity was used in the estimation of the drag and lift coefficients. The ADV was able to measure 3-D water velocities using coherent Doppler processing technology. In this study, a side looking ADV was used. The ADV's sampling rate was set to 200 Hz. The instrument was located at $x = 5.6$ m, 0.10 m upstream of the outer edge of the pipe. To derive the velocity profile, each experiment was repeated three times, and the ADV was moved vertically to different depths: (1) The highest water level; (2) the location where the center-axis of the pipe cross section was placed and 0.03 m above the flume bed. Non-uniformities in the cross-flow direction were assumed to be negligible. The water was seeded before each test using aluminum oxide powder with 27 micron particle size (400 mesh) to ensure adequate signal to noise ratio for ADV measurements.

3.2.2.3. Dynamometer

To record the time-history of the forces exerted on the pipe, a 6 degree of freedom (DOF) dynamometer (Interface- 6A68E, non-linearity, 0.04%, maximum capacity: $Fx = Fy$ =10 kN, Fz = 20 kN, $Mx = My = Mz$ = 500 Nm, Interface Inc., Scottsdale, AZ, USA) was used. This dynamometer was able to simultaneously measure the time-histories of the forces and moments along the three axes. The dynamometer was installed beneath the concrete flume floor by cutting the concrete flume floor, placing the device and re-embedding it, as shown in Figure 3.3a,b.

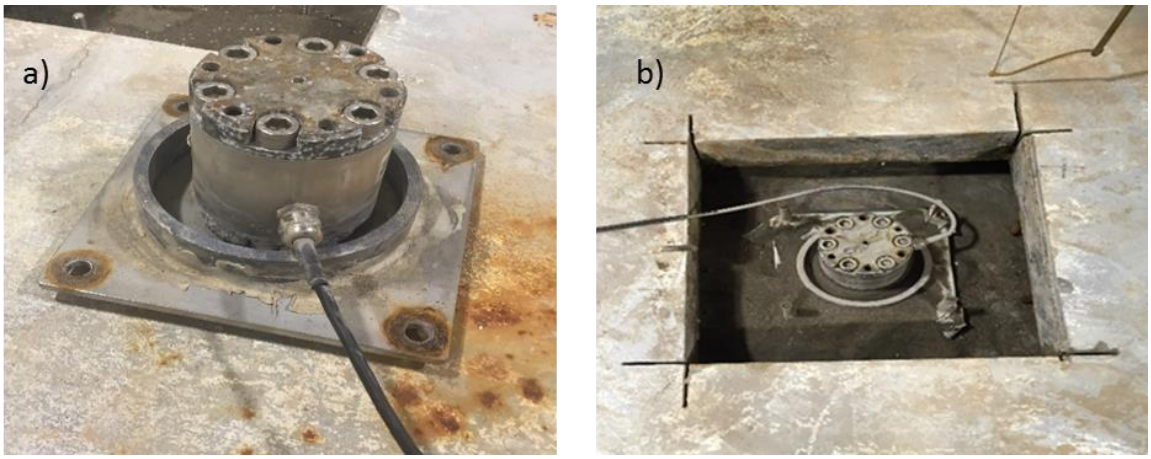

Figure 3.3. (**a**) Dynamometer (Interface-6A68E) and (**b**) dynamometer embedded in the flume floor.

A stiff steel plate was placed on top of the instrument, levelled with the flume. This plate transmitted the exerted force to the dynamometer through four bolts which rigidly fastened the instrument to the pipe model. The cable was securely placed in the flume floor recess, ensuring that no additional forces were transmitted on to the transducer. The pipe was attached to the plate using two very narrow, vertical plates, as shown in Figure 3.2a. The dynamometer was calibrated using the calibration chart provided by the manufacturer and re-zeroed before each test. The sampling rate for the dynamometer was set to 300 Hz. The amount of force and moment applied to the dynamometer was converted to voltage and recorded by the data acquisition system.

3.2.2.4. Data Acquisition System

Analog voltage signals from different instruments used in the experiments were converted to digital format and saved into data files using the QuantumX data acquisition system (MX840B, 8-channel universal amplifier and MX1601B with 16 individually configurable channels, HBM, Marlborough, MA, USA). All data were synchronized between the devices using a FireWire connection.

3.2.2.5. Camera

A camera (HS, Flare 2M360-CL, sampling rate 70 Hz, IO Industrial, London, ON, Canada) was directed towards the pipe from top to capture and analyze the bore impact with the pipe. A GoPro Hero4 Black (GoPro, San Mateo, CA, USA) was also installed 2 m upstream of the pipe and was used for observation purposes.

3.2.2.6. Cylindrical Pipe

A steel pipe, referred to as the cylindrical pipe, with an outer diameter of 100 mm, a wall thickness of 5 mm and a length of 1470 mm was used in the experiments. The pipe was connected to the upper plate bolted to the dynamometer using two brackets, 2 mm thick, made of steel, as shown in Figure 3.1a.

3.3 Experimental Test Program

Findings from this study were used in the companion paper (part 2) to characterize hydrodynamic forces exerted on pipelines, due to extreme flow events, modelled using a dam-

break wave. A systematic and comprehensive experimental approach was conducted for this purpose. The most relevant parameters governing the problem at hand were varied during the experiments, namely: Reservoir depth (*h*), tailwater depth (*d*), lower edge of pipe distance to bed (*e*) to diameter ratio (*e/D*) and pipe level of submergence (*S*) to pipe diameter ratio (*S/D*). (Figure 3.1c). Table 3.1shows the list of hydrodynamic tests in the absence of the pipe, while Table 3.2 illustrates the list of experiments in the presence of a pipe with different experimental configurations. Each test was repeated three times to assess the repeatability of the results of each test. Head ratio (*d/h*) is defined as the ratio between the still water depth (*d*) and impoundment depth (*h*).

Table 3.1. List of hydrodynamic tests (no pipe).

	Reservoir Depth *h* (m)	**Still Water Depth *d* (m)**	**Head Ratio *d/h* (-)**
Hydrodynamic test (no pipe)	0.3	0	0
		0.03	0.1
		0.06	0.2
		0.08	0.26
		0.12	0.4
		0.17	0.56
Hydrodynamic test (no pipe)	0.4	0	0
		0.03	0.075
		0.06	0.15
		0.08	0.2
		0.12	0.3
		0.17	0.425
Hydrodynamic test (no pipe)	0.5	0	0
		0.03	0.06
		0.06	0.12
		0.08	0.16
		0.12	0.24
		0.17	0.34

Table 3.2. List of experimental configurations in the presence of a pipe.

Gap ratio e/D	Reservoir depth h (m)	Still water depth d (m)	head ratio d/h (-)	Level of submergence ratio S/D (-)
0.3	0.30	0.00	0.000	0.0
		0.03	0.100	0.0
		0.06	0.200	0.3
		0.08	0.260	0.5
		0.12	0.400	1.0
	0.40	0.00	0.000	0.0
		0.03	0.075	0.0
		0.06	0.150	0.3
		0.08	0.200	0.5
		0.12	0.300	1.0
	0.50	0.00	0.000	0.0
		0.03	0.060	0.0
		0.06	0.120	0.3
		0.08	0.160	0.5
		0.12	0.240	1.0
0.6	0.30	0.00	0.000	0.0
		0.03	0.100	0.0
		0.06	0.200	0.0
		0.08	0.260	0.2
		0.12	0.400	0.6
		0.17	0.560	1.0
	0.40	0.00	0.000	0.0
		0.03	0.075	0.0
		0.06	0.150	0.0
		0.08	0.200	0.2
		0.12	0.300	0.6
		0.17	0.425	1.0
	0.50	0.00	0.000	0.0
		0.03	0.060	0.0
		0.06	0.120	0.0
		0.08	0.160	0.2
		0.12	0.240	0.6
		0.17	0.340	1.0
0.8	0.30	0.00	0.000	0.0
		0.03	0.100	0.0
		0.06	0.200	0.0
		0.08	0.260	0.0
		0.12	0.400	0.4
		0.17	0.560	1.0

	0.00	0.000	0.0
	0.03	0.075	0.0
0.40	0.06	0.150	0.0
	0.08	0.200	0.0
	0.12	0.300	0.4
	0.17	0.425	1.0
	0.00	0.000	0.0
	0.03	0.060	0.0
0.50	0.06	0.120	0.0
	0.08	0.160	0.0
	0.12	0.240	0.4
	0.17	0.340	1.0

3.3.1. Test Repeatability (Water Level Time History)

Multiple tests with identical impoundment depths and initial still water depths were carried out to verify the repeatability of the tests. Figure 3.4 shows the water surface profile in dry and wet bed conditions measured by WG2 at x = 3.5 m. Good agreement of water surface time-histories was achieved between multiple repetitions for both dry and wet bed conditions. Normalized standard deviations (σ/h) of less than 5% for wet bed and less than 4% for the dry bed were obtained.

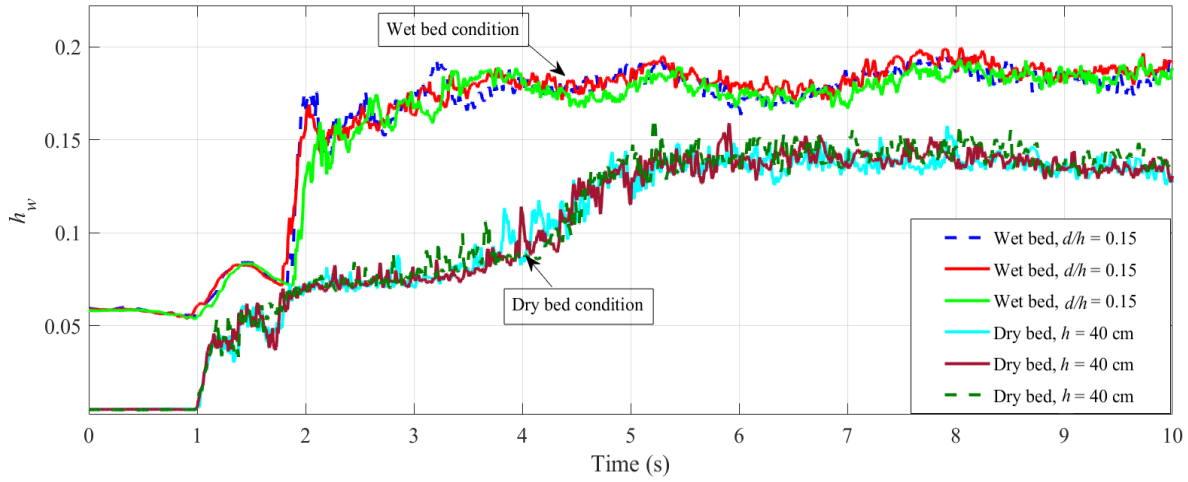

Figure 3.4. Repeatability of tests for water level time history (WG2), with various water depth (h) values of dry bed condition and d/h values of the wet bed condition.

3.4. Results and discussion

3.4.1. Dry bed condition hydrodynamics

3.4.1.1. Dry Bed Water Surface Profile

Figure 3.5 illustrates the measured water surface profile at the locations of the three wave gauges, shown in Figure 3.1. Figure 3.5a shows the normalized water level h_w/h time-history at the location of the reservoir wave gauge (WG1), indicating a decrease in reservoir water depth in time. The gate opening time was used as the reference time in all three figures. Figure 3.5b,c illustrate the water surface profile for WG2 at x = 3.5 m and WG3 at x = 5.5 m (at the pipe location) downstream of the gate, respectively. Both Figure 3.5b,c illustrate the earlier wave arrival time for the dry bed surges generated using larger impoundment depth indicating a larger bore front celerity. The bore front celerity is discussed in more detail in Section 3.1.2. Comparison between water level magnitudes in Figure 3.5b,c also indicates a decrease in water level as the surge moves forward through the flume. The average non-dimensional water level ($\frac{h_w}{h}$) was decreased by 32% at WG3 compared to WG2. This can be explained with energy losses, due to bed friction in the case of flow on dry bed condition.

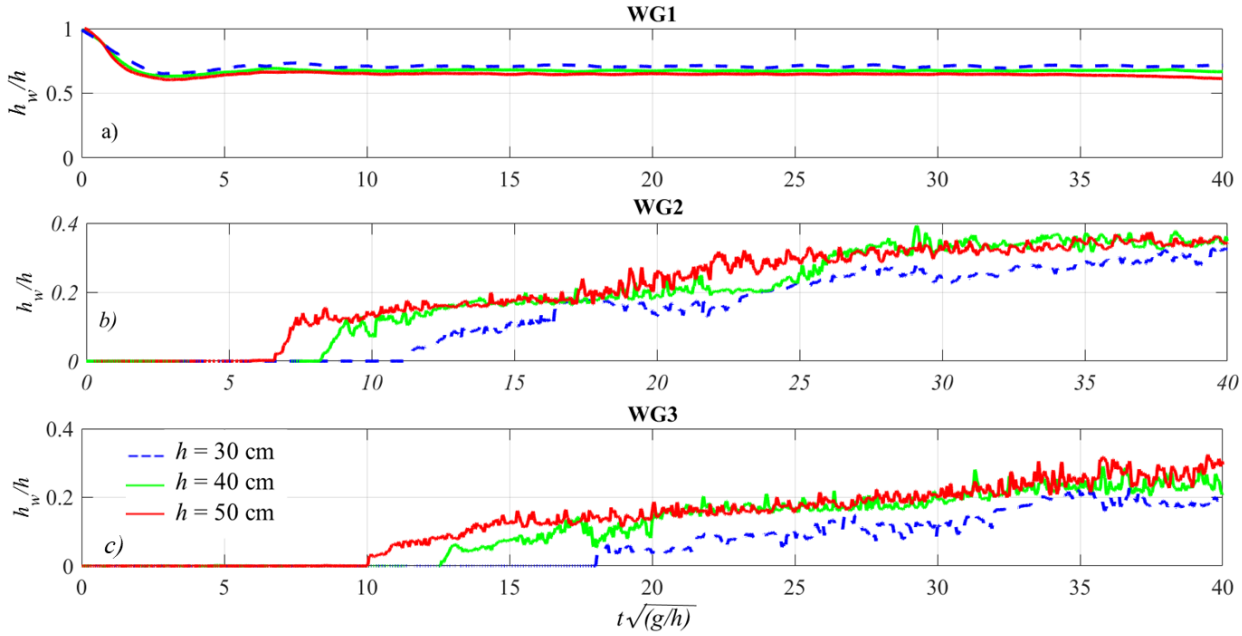

Figure 3.5. Dry bed surge time-history of the water surface profile. h = 50, 40, 30 cm measured at location of the (**a**) reservoir wave gauge (WG1), (**b**) x = 3.5 m (WG2) and (**c**) x= 5.5 m (WG3).

Figure 3.6 compares experimental results for the water surface profiles for dam-break flow in dry bed conditions, obtained from multiple tests with identical gate opening conditions and wave gauge locations along the flume, with the analytical solution of the Saint-Venant equations for a horizontal, frictionless surface given by Ritter 1892 as:

$$\frac{h_w}{h} = \frac{1}{9}\left(2 - \frac{x}{ht\sqrt{\frac{g}{h}}}\right)^2 \qquad \text{(Eq. 3.2)}$$

In Figure 3.6, water surface profiles are plotted versus the dimensionless time, $t\sqrt{g/h}$. Experimental and Ritter's theoretical solution were compared at WG2 (x = 3.5 m) for three different impoundment depths h = 30, 40, and 50 cm. Figure 3.6 shows that, initially ($0 < t\sqrt{g/h} < 2$), the experimental results do not accurately match the Ritter 1982 solution. This observed discrepancy is due to the fact that the surface roughness of the flume bed in the Ritter solution is ignored (fully smooth bed). For the case of the dry bed conditions and at the beginning of a dam-break wave surge, roughness plays a significant role as there is direct contact between the bore front and flume surface. The experimental results agree with a study conducted by Lauber and Hager 1998 where the bed roughness was shown to have a significant effect close to the wave fronts. Other studies, i.e., Wüthrich et al., 2018a also found, namely Ritter's solution does not accurately represent the dam-break flow at the vicinity of the wave front because of the bed roughness.

3.4.1.2. Dry Bed Bore Front Celerity

The average front celerity of the propagating wave was estimated using the following ratio:

$$U = \frac{\Delta x}{\Delta t} \qquad \text{(Eq. 3.3)}$$

where U is the bore front celerity in m/s. Δx is the distance between two wave gauges downstream of the gate, WG2 and WG3, and is equal to 2.1 m. The surge travel time is shown with Δt, as the time taken by the bore to travel between the two wave gauge positions.

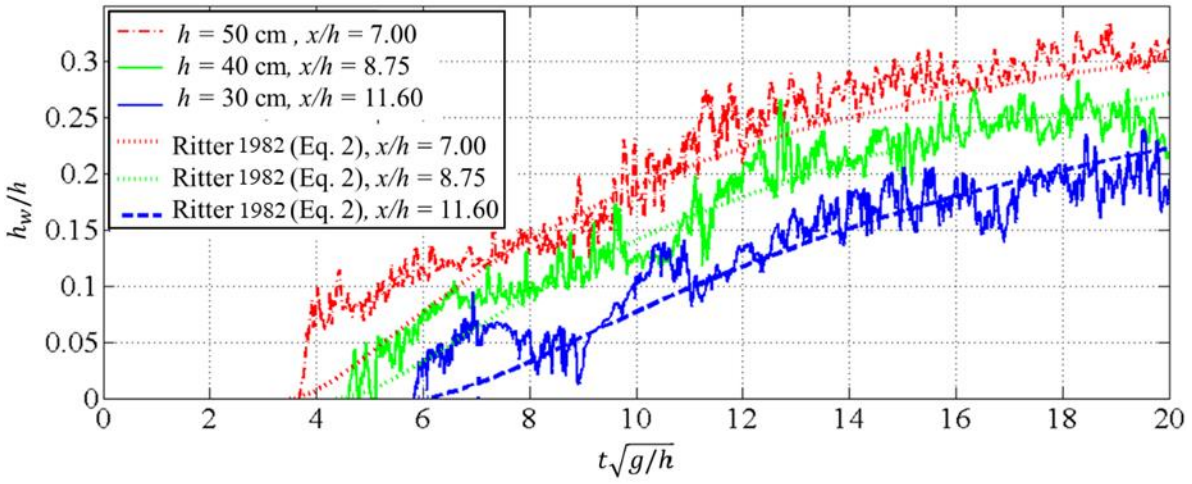

Figure 3.6. Non-dimensional dry bed condition water time-history surface profile: Comparison with Ritter's (1892) solution. $\frac{h_w}{h}$ versus non-dimensional time $t\sqrt{g/h}$ with $\frac{x}{h}$ = 7, 8.75, 11.6.

Several previous studies have estimated the bore front celerity *(U)* relative to impoundment depth *(h)* using:

$$U = \propto \sqrt{gh} \qquad \text{(Eq. 3.4)}$$

where α is a constant with various values reported in the literature. The constant value depends on the flume hydraulic radius and roughness coefficient. Wüthrich et al., 2018 suggest $\propto = 1.25$, while Matsutomi and Okatamo 2014 suggest $\propto = 1.1$. Figure 3.7 shows results from the current study, together with the previous studies mentioned above. This study suggests $\propto = 1.2$ as the constant in Equation (3-4).

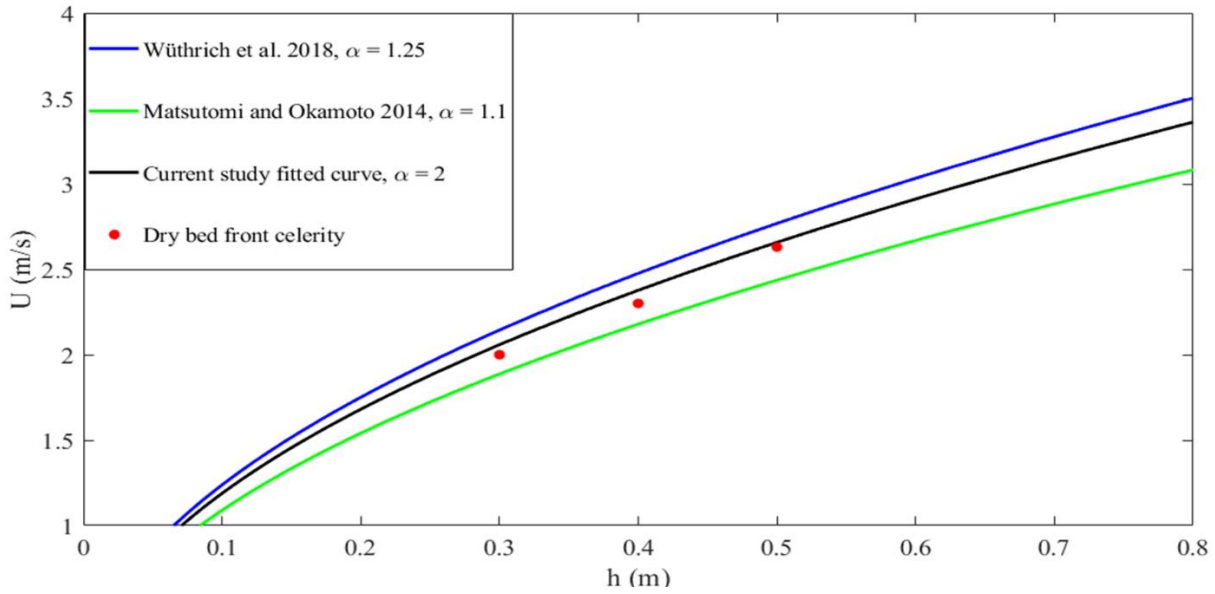

Figure 3.7. Comparison between the front celerity for dry bed in this study and previous studies.

3.4.1.3. Dry Bed Flow Velocity, Froude Number and Momentum Flux

Flow characteristics at the pipe location were studied to analyze the exerted forces on the pipeline. Figure 3.8 illustrates the dry bed surge characteristics as water surface profile (WG3), flow velocity, Froude number and momentum flux at the location of the pipe, respectively.

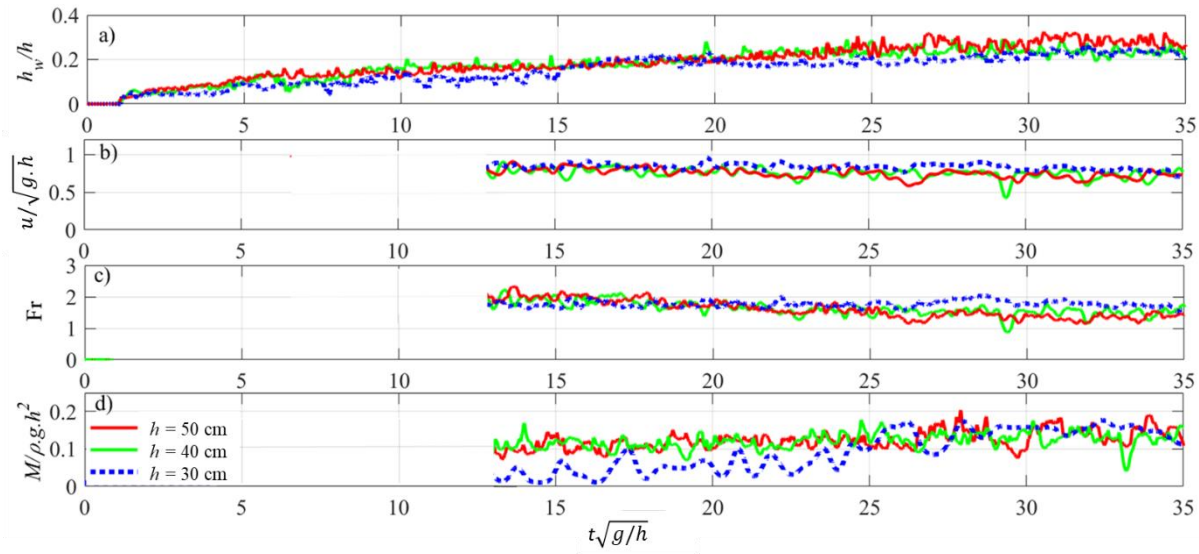

Figure 3.8. Dry bed surge characteristics at x = 5.5 for h = 30, 40, 50 cm. (**a**) water surface time-history profile (WG3), (**b**) flow velocity time-history, (**c**) Froude number time-history and (**d**) momentum flux time-history.

The reference time for all the cases is the wave arrival time at WG3. There is a delay in the velocity measurements using the ADV, due to the air entrainment close to the wave arrival time which corresponds to the zone with no data in the first few seconds in Figure 3.8b–d. Calculated Froude numbers ($\mathrm{Fr} = \frac{u}{\sqrt{gh_w}}$) for dry bed conditions and for different reservoir impoundment depths are shown in Figure 3.8c. It should be noted that for the impoundment depth of h = 30 cm, the water level increases and the flow velocity decreases more gradually compared to the cases with h = 40 cm and h = 50 cm. The dry bed surge was supercritical, Fr > 1, throughout the studied time frame for all three impoundment depths, as shown in Figure 3.8c. The Froude number remains almost constant in the case of h = 30 cm whereas, it gradually decreases for h = 40 cm and h = 50 cm.

The momentum flux per unit width M is an important factor directly affecting the hydrodynamic loading on structures.

$$M = \rho h_w u^2 \qquad \text{(Eq. 3.5)}$$

where h_w, is the water level and u is the depth-averaged flow velocity. Figure 3.8d shows the non-dimensional computed momentum flux as $\frac{M}{\rho g h^2}$ for dry bed and different impoundment depths. Figure 3.8d illustrates that the non-dimensional momentum is smaller for h = 30 cm at the beginning of the surge. This could be explained by considerately smaller flow velocity, as well as small water depth in the case of h = 30 cm. Smaller momentum flux results in smaller induced drag force as is discussed in the companion paper.

3.4.2. Wet bed condition hydrodynamics

3.4.2.1. Wet Bed Water Surface Profile

Figure 3.9 illustrates the water surface profile for wet bed condition with impoundment depth of h = 40 cm and different still water levels *(d)* at the location of three wave gauges WG1 (a), WG2 (b) and WG3 (c). The reference time in the figure was the gate opening time. The figure shows earlier arrival time for the cases with smaller still water depth (wet bed condition) which indicates a larger bore front celerity in such cases. The values recorded by WG2 and WG3, shown in Figure 3.9b,c, did not exhibit any change in the water surface profiles. Stoker 1958 called the region where the water level remains constant "zone of constant state".

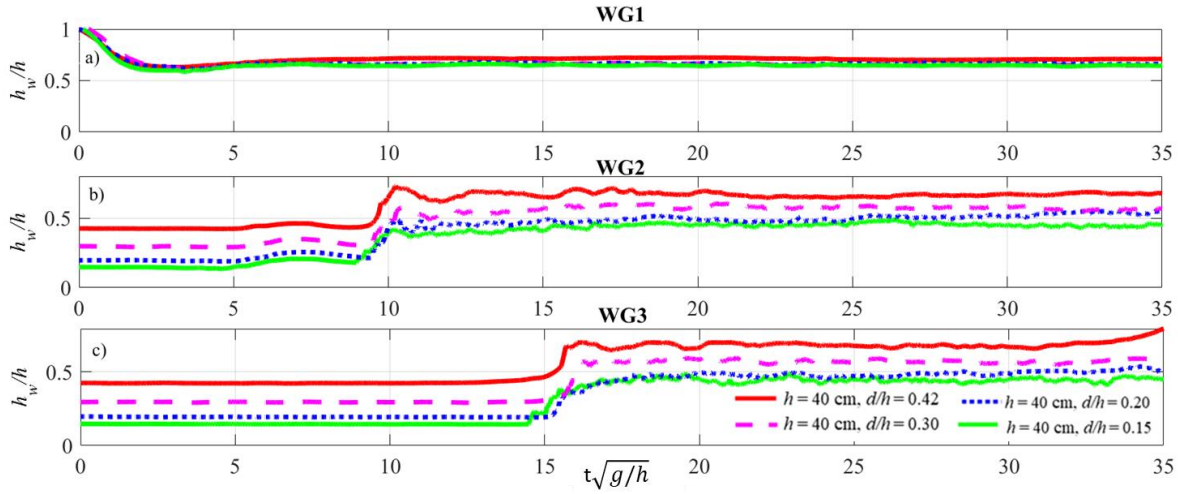

Figure 3.9. Wet bed bore water surface time history for h = 40 cm, different still water levels, d = 6, 8, 12, 17 cm, measured at location of (**a**) reservoir wave gauge (WG1), (**b**) x = 3.5 m (WG2) and (**c**) x = 5.5 m (WG3).

Figure 3.10 shows a comparison between dry bed and wet bed condition water surface time-histories. The data shows a steeper bore front and more abrupt water level rise in the case of the bore propagating over wet bed when compared to dry bed. Other researchers, i.e., Nouri et al. 2010 and Wüthrich et al., 2018a, also found a similar behavior. According to Wüthrich et al. 2018a the behavior of a bore propagating on the wet bed at the wave front, is similar to a turbulent and highly aerated hydraulic jump which causes a more abrupt water level rise compared to wave propagating over dry bed condition.

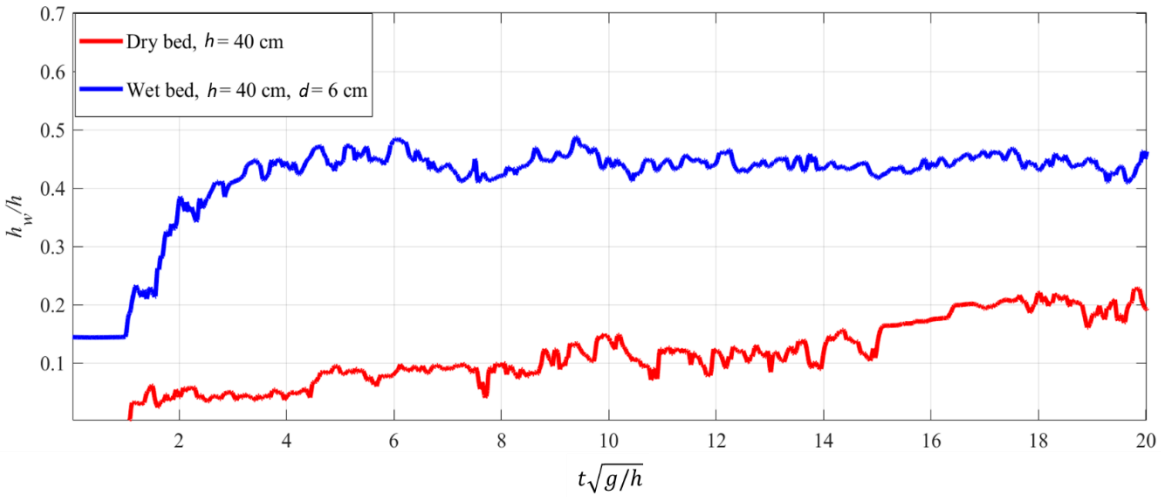

Figure 3.10. Comparison between dry bed and wet bed condition normalized water depth time-history.

3.4.2.2. Wet Bed Bore Front Celerity

The bore front celerity was calculated using Equation (3-3) for the case of wet bed condition for different reservoir impoundment and downstream still water depths. Figure 3.11 illustrates the dimensionless bore front celerity versus head ratio *(d/h)* obtained from this study together with Chanson 2005 empirical solution for bore front celerity in a horizontal channel initially filled with water as:

$$\frac{U}{\sqrt{gd}} = \frac{0.6345 + 0.3286(\frac{d}{h})^{0.65167}}{0.00251 + (\frac{d}{h})^{0.65167}} \qquad \text{(Eq. 3.6)}$$

Results show good agreement between experimental data and the solution of Chanson 2005, which depicts the validity of the empirical solution proposed by this author.

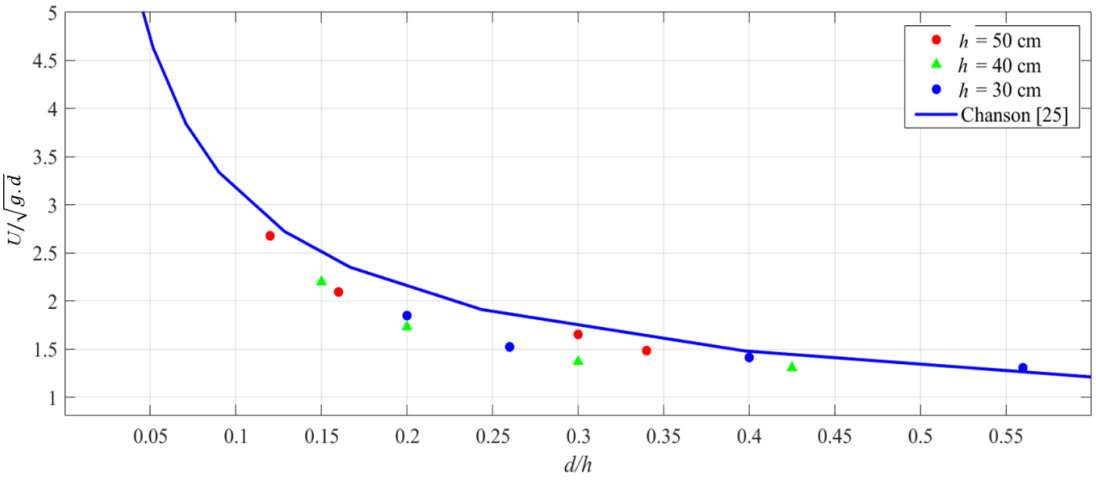

Figure 3.11. Bore front celerity *d/h*. The solid line shows Chanson 2005 solution (Eq. 3.6), while the points show experimental data. (Adapted from [Chanson 2005])

3.4.2.3. Wet Bed Flow Velocity, Froude Number and Momentum Flux

Figure 3.12 depicts the wet bed bore flow velocity, the computed Froude numbers and momentum flux in the case of wet bed condition, a constant impoundment depth of h = 40 cm, and different still water depths *(d)*. The reference time for all the cases is the wave arrival time at WG3. Due to the air entrainment close to the wave arrival time, the flow velocity data at the beginning of the bore propagation were considered invalid and were eliminated from Figure 3.12b–d. Results show a noticeable decrease in flow velocity (Figure 3.12b) and the estimated Froude number (Figure 3.12c), with an increase in the still water depth or d/h ratio. This is because such waves were generated using a smaller pressure head (the small difference between the upstream impoundment depth and the downstream still water depth) which resulted in slower flow velocities and lower Froude numbers. Results from all the three tested impoundment depths, i.e., h = 30, 40, 50 cm, show that for d/h = 0.3 the flow was subcritical, while for $d/h \leq 0.2$ the flow was supercritical. Head ratio values around 0.2 resulted in critical flow regime with Froude number values fluctuating around one. Figure 3.12d shows the calculated non-dimensional momentum flux($\frac{M}{\rho g h^2}$) values in the case of wet bed condition for impoundment depth of h = 40 cm.

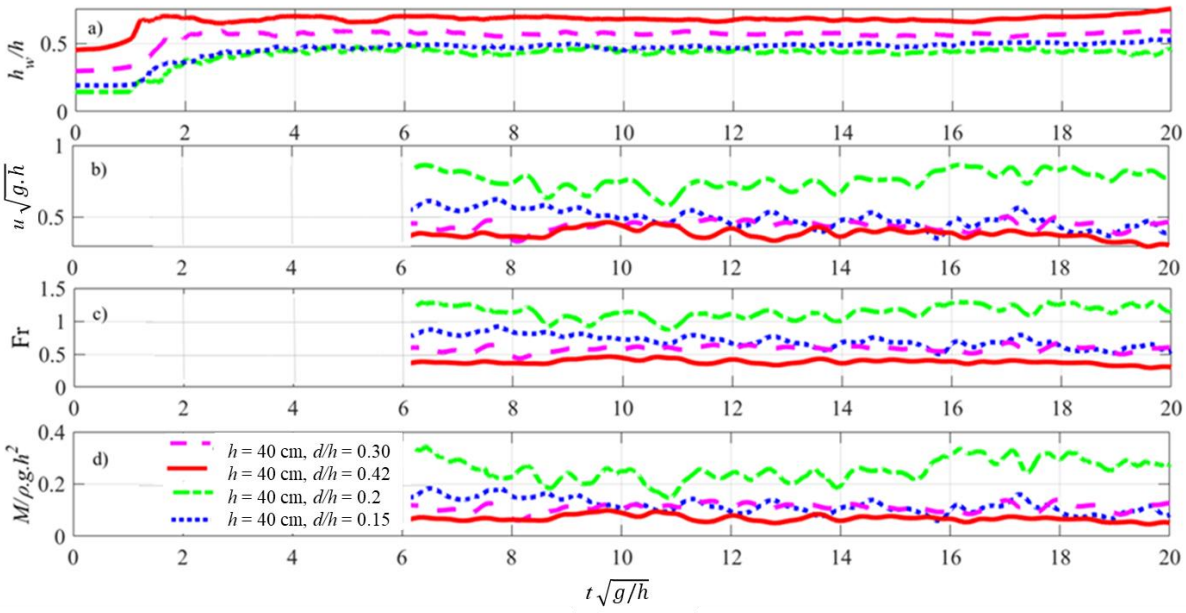

Figure 3.12. Wet bed bore characteristics at x = 6.5 for h = 40 cm, different line types show different d/h values. (**a**) Water surface time-history profile (WG3), (**b**) flow velocity time-history, (**c**) Froude number time-history and (**d**) momentum flux time-history.

Results show that the momentum flux decreases as the value of d/h increases. Smaller flow velocities in the bores generated using a smaller head (larger d/h) resulted in smaller momentum values. The same trend was observed for the case with h = 30 cm and h = 50 cm.

Chanson 2005 presented a solution for a dam-break wave moving over a frictionless horizontal channel initially filled with water. The basic flow equations in wet bed conditions are the characteristic system of equations for simple waves as forward and backward characteristics. The forward characteristic in wet bed condition satisfies:

$$V_2 + 2\sqrt{gh_w} = V_0 + 2\sqrt{gh} \qquad \text{(Eq. 3.7)}$$

where h is the reservoir depth and V_2 and h_w are the flow velocity (m/s) and bore depth (m) immediately behind the positive surge. The quantity V_0 is the initial reservoir velocity (m/s) equal to zero in the current experiments. Chanson 2005 solved this equation together with the continuity and momentum equations graphically. Figure 3.13 compares Chanson 2005 graphical solution and V_2 values measured in current experimental work in a test with d/h = 0.2 (h = 40 cm, d = 8 cm). Results showed good agreement between the two studies.

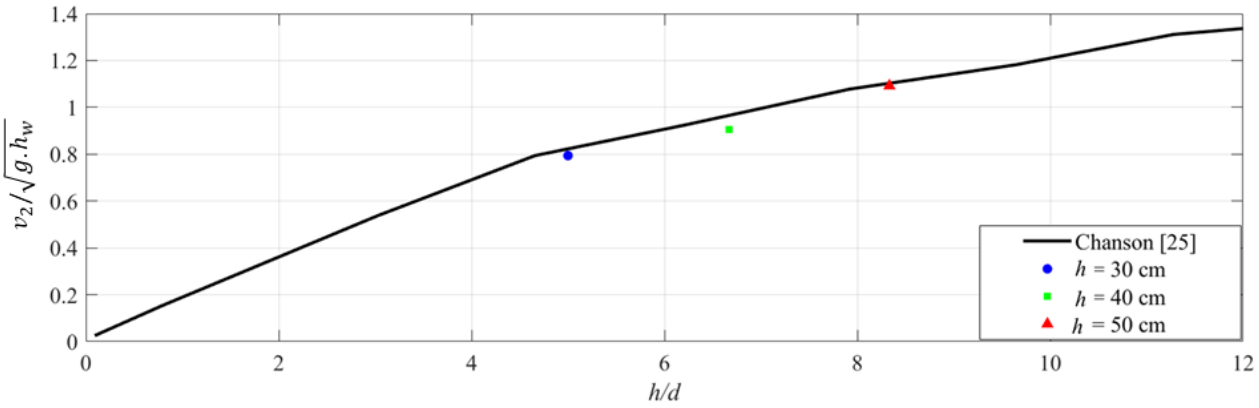

Figure 3.13. Tests with the wet bed condition flow velocity compared to Chanson's 2005 graphical solution.

3.5. Changes in Hydrodynamic Conditions Due to the Presence of the Pipe

3.5.1. Dry Bed Condition

Influence of Pipe Gap Ratio (e/D) in Dry Bed Condition

Experimental results in the presence of the pipe showed a considerable change in flow hydrodynamic characteristics, i.e., in the water level and flow velocity. Figure 3.14 illustrates the alterations in the flow hydrodynamics in dry bed condition in the presence of the pipe with three different gap ratios (*e/D*) compared to the flow in the absence of the pipe. The reference time for all experimental tests is the bore arrival time at WG3. There is a delay in velocity measurements using ADV due to the air entrainment close to the wave arrival time which corresponds to the zone with no data in the first few seconds in Figure 3.14b. The figure also shows that in the case of the smallest gap ratio (*e/D* = 0.3), water reached to the pipe surface faster than other cases and caused abrupt water level rise, as shown in Figure 3.14 (dashed line at t = 1.8 s). The water level rise at the pipe location was due to the flow being blocked by the pipe at the time of wave impact. Results of the flow velocities presented in Figure 3.14b show that the flow velocity reduced in the presence of the pipe, due to flow blockage by the latter. The flow velocity decreased to smaller values after the partial blockage by the pipe. This happened faster as the gap ratio *e/D* decreased from 0.8 to 0.3, since the water reached the lower edge of the pipe and was blocking the incoming flow sooner. At lower gap ratios, i.e., *e/D* = 0.3, the pipe also got fully submerged earlier which reduced the

flow turbulence caused by wave run-up and resulted in the flow velocities to be lower compared to the cases with larger *e/D* (Figure 3.14b).

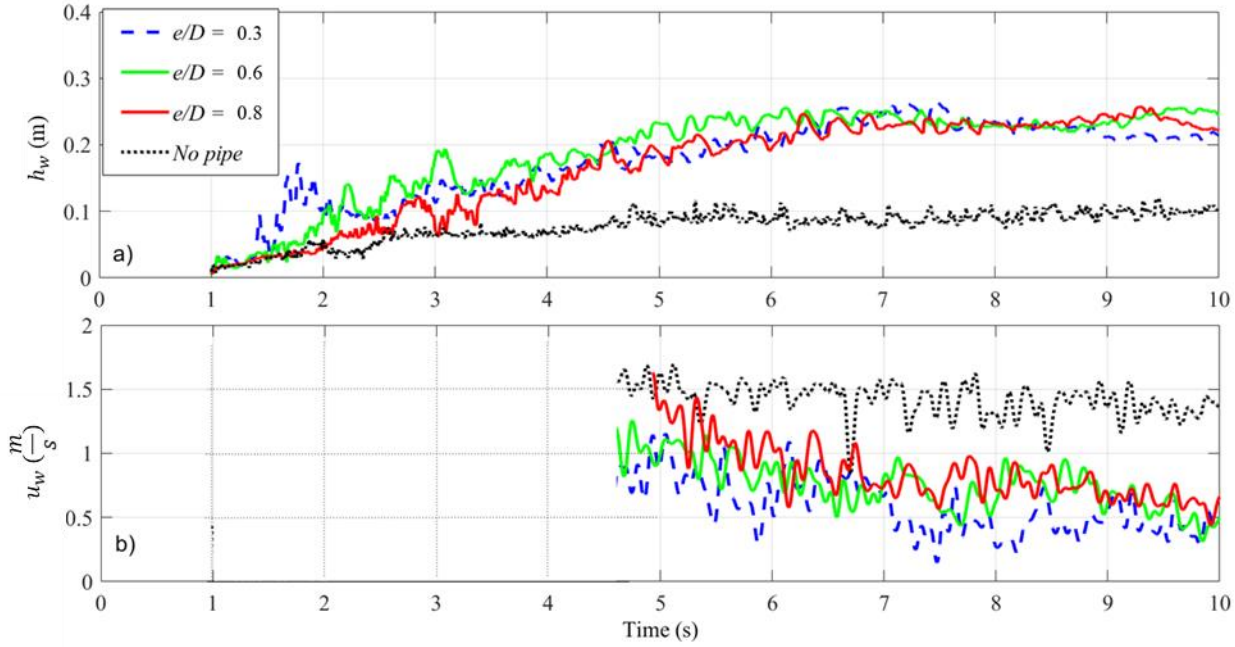

Figure 3.14. Effect of pipe existence in flow hydrodynamics for different *e/D* values, dry bed condition and *h* = 40 cm. (**a**) Water level time history and (**b**) flow velocity time-history.

Influence of Impoundment Depth

Figure 3.15 illustrates the water level rise at the time of bore impacting the pipe. The water level rise is more pronounced for the bore produced by the *h* = 50 cm impoundment depth (Figure 3.15a) and smallest for that generated by the *h* = 30 cm impoundment depth (Figure 3.15c). Such abrupt water level rise in larger impoundment depth results in more pronounced impulse force in such cases. Force time-histories are discussed in more detail in the companion paper (Ghodoosipour et al. 2019b).

(**a**) (**b**) (**c**)

Figure 3.15. Water level rise at the time of bore impact generated by impoundment depths of (**a**) *h* = 50 cm, (**b**) *h* = 40 cm and (**c**) *h* = 30 cm.

3.5.2. Wet Bed Condition

Influences of Changing Still Water Depth (*d*) and Submergence Ratio (*S/D*)

Figure 3.16 shows the change in flow hydrodynamics in the case of wet bed condition for different still water depths and submergence ratios (*S/D*). Results for all different *d/h* values showed a similar behavior as in the dry bed case where the water level increased, and flow velocity decreased by the obstruction caused by the presence of the pipe. Figure 3.16 also shows that in the presence of pipe, the difference between water level and flow velocity with and without pipe is larger in lower still water depths. The root mean square difference (RMSE) were calculated for flow velocity values and for different still water depths. The calculated RMSE showed a decrease from 0.56 for *d/h* = 0.15, where the pipe is non-submerged (*S/D* = 0, Figure 3.16e), to 0.19 for *d/h* = 0.425, where the pipe is fully submerged (*S/D* = 1, Figure 3.16h). RMSE also decreased considerably from 0.40 for the case of less than half submerged pipe (*S/D* = 0.2, Figure 3.16f) to 0.25 for the case of more than half submerged (*S/D* = 0.6, Figure 3.16g). Decreased level of pipe submergence resulted in decreased pipe's effective contact area; hence, reduced flow blockage by the pipe. Therefore, the increased level of pipe submergence by increasing still water depth resulted in the reduced influence of pipe presence on flow hydrodynamics. Figure 3.17 illustrates how the water level rise becomes more abrupt, distinguished with more splashes, at the time of bore impact for cases with lower initial still water depth; thus, smaller level of pipe submergence.

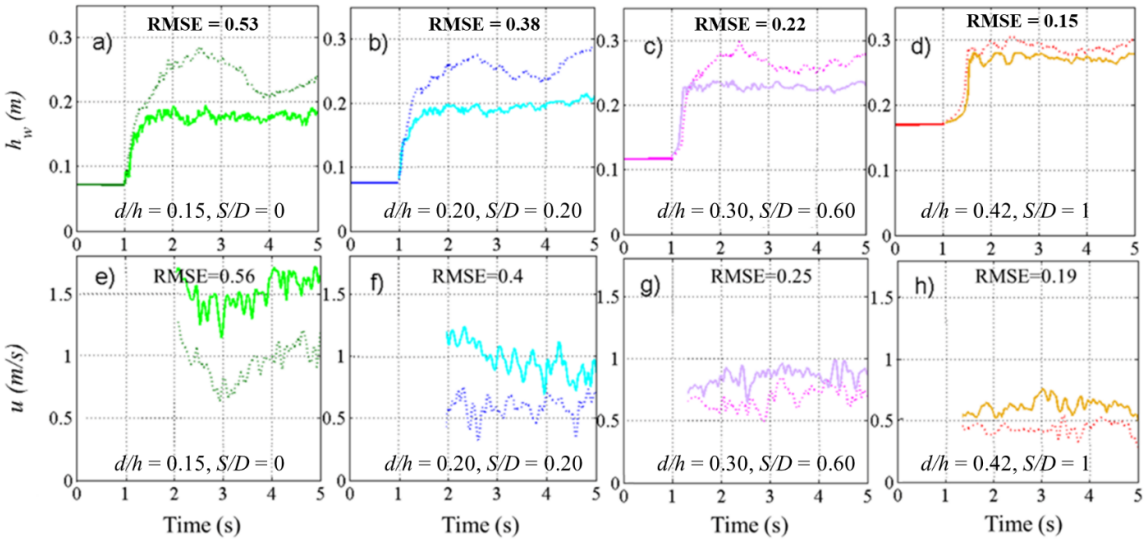

Figure 3.16. Effect of pipe presence on flow hydrodynamics, different still water depth (**d**), wet bed condition and impoundment depth, *h* = 40 cm, (**a**) and (**d**): *d/h* = 0.15, non-submerged pipe *S/D* = 0, (**b**) and (**f**): *d/h* = 0.2, less than half submerged *S/D* = 0.2, (**c**) and (**g**): *d/h* = 0.3, more than half submerged *S/D* = 0.6, (**d**) and (**h**): *d/h* = 0.425, fully submerged *S/D* = 1.0. (Dashed line and continuous line show the "with pipe" and "no pipe" conditions, respectively).

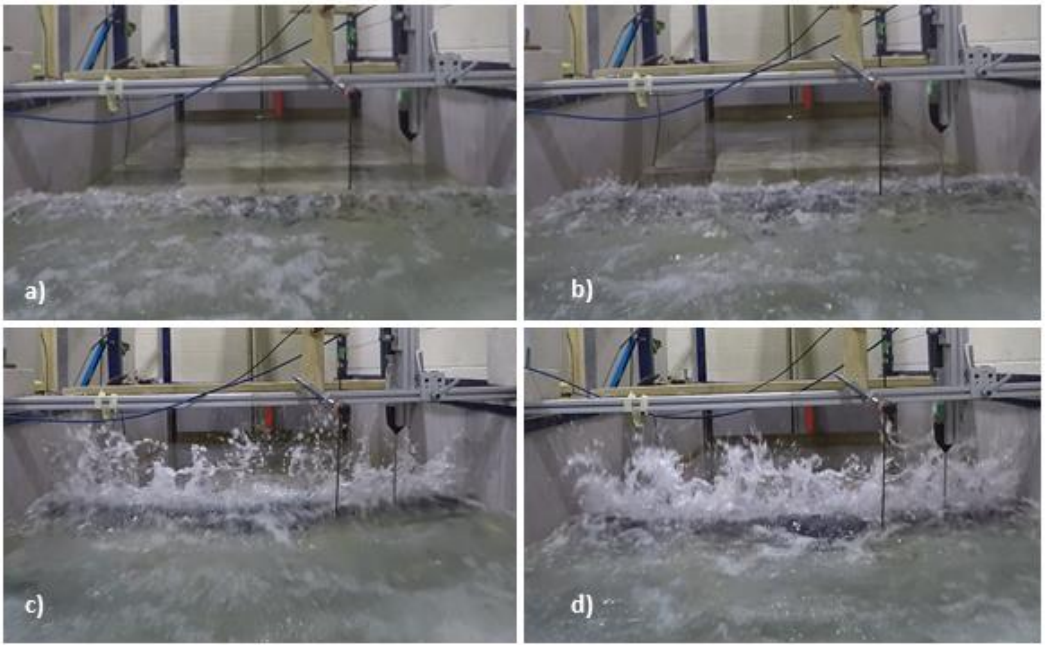

Figure 3.17. Water level rise at the time of bore impact, wet bed condition, and impoundment depth h = 40 cm (**a**) d/h = 0.425, S/D = 1, (**b**) d/h = 0.3, S/D = 0.6, (**c**) d/h = 0.2, S/D = 0.2, (**d**) d/h = 0.2, S/D = 0.

3.6. Scale effects

Table 3.3 summarizes the flow conditions in this study at the location of the pipe. Previous modelling results from the 1993 Hokkaido-Nansei-Oki Tsunami estimated water depths in the range of 5–15 m and flow velocities in the range of 3–15 m/s. Coastal inundation heights reached 4 to7 m in the southern part of Khao Lak (Diaset al., 2006; Matsutomi et al., 2006). Maximum water depth for Hurricane Irma at Charleston USA was reported as 3 m and for Typhoon Ida at China as 1m (Wüthrich 2018). As shown in Table 3.3, the wave height and wave front celerity measured in this study are in the range of the modelling results mentioned above. According to Lauber and Hager 1998, for impoundment depths $h \geq 0.30$ m, inertia forces are dominating and the flow is governed by Froude similarity. This condition applies to all experiments conducted in this study, where the impoundment depths were either equal to or larger than 30 cm. According to Bricker et al. 2015, when using Froude scaling for tsunami modelling, surface tension and viscous effects must be appropriately considered. Weber numbers in Table 3.3 were calculated using:

$$\mathrm{We} = \frac{\rho u^2 h_w}{\sigma} \qquad \text{(Eq. 3.8)}$$

where ρ is the water density ($\frac{kg}{m^3}$), u is the flow velocity, h_w is the water depth, and σ is the surface tension (N/m).

Table 3.3. Hydrodynamic conditions at the pipe location.

Reservoir Depth h (m)	Head Ratio d/h	Maximum wave height (m)	Prototype maximum wave height (m)	Wave Front Celerity (m/s)	Prototype wave front celerity (m/s)	Weber Number (-)	Flow Reynolds Number (-)	Pipe Reynolds Number (-)	Froude Number (-)
0.3	0.00	0.078	1.95	2.00	10.00	4285	1.56×10^5	2.00×10^5	2.29
	0.20	0.100	2.50	1.41	7.05	2730	1.41×10^5	1.41×10^5	1.42
	0.26	0.107	2.68	1.53	7.65	3440	1.56×10^5	1.53×10^5	1.49
	0.40	0.136	3.40	1.35	6.75	3404	1.83×10^5	1.35×10^5	1.17
	0.56	0.163	4.08	1.67	8.35	6244	2.7×10^5	1.67×10^5	1.32
0.4	0.00	0.128	3.20	2.27	11.35	9060	2.90×10^5	2.26×10^5	2.03
	0.15	0.172	4.30	1.68	8.40	6688	2.88×10^5	1.68×10^5	1.29
	0.20	0.176	4.40	1.53	7.65	5660	2.69×10^5	1.53×10^5	1.16
	0.30	0.224	5.60	1.48	7.40	6739	3.31×10^5	1.48×10^5	1.00
	0.43	0.268	6.70	1.67	8.35	10,266	4.47×10^5	1.67×10^5	1.03
0.5	0.00	0.160	4.00	2.60	13.00	14,857	4.16×10^5	2.60×10^5	2.08
	0.12	0.215	5.38	2.05	10.25	12,411	4.40×10^5	2.05×10^5	1.41
	0.16	0.220	5.50	1.85	9.25	10,342	4.07×10^5	1.85×10^5	1.26
	0.24	0.280	7.00	1.79	8.95	12,323	5.01×10^5	1.79×10^5	1.08
	0.34	0.335	8.38	1.91	9.55	16,787	6.39×10^5	1.91×10^5	1.05

As shown in Table 3.3, *We* in all the tested cases are larger than the critical We defined by Peakall and Warburton 1998, i.e., $We_{crit} \leq 120$. Therefore, the effect of changing surface tension in relation to nature scale could be neglected in this study. According to Te Chow 1959, the flow in this study is fully turbulent ($1.41 \times 10^5 < Re < 6.39 \times 10^5$). However, tsunami flow is usually associated with flow Reynolds numbers larger than 10^6. Therefore, the bottom boundary layer may not be properly represented in the conducted experiments (Bricker 2015). The present study focuses on the force on the pipe; thus, pipe Re could be more influential. The flow and pipe Reynolds number in the experiments were calculated using:

$$\mathrm{Re} = \frac{h_w u}{\nu} \qquad \text{(Eq. 3.9)}$$

$$Re = \frac{Du}{\nu} \qquad \text{(Eq. 3.10)}$$

where h_w is the water depth, D is the pipe diameter and ν is the kinematic viscosity. The flow velocity (u) in Equation (3.9 and 3.10) is the free stream velocity measured at the location of the pipe center. Calculated values were in the range of $8 \times 10^4 < \mathrm{Re} < 2.6 \times 10^5$. Wüthrich et al., 2005 and Sumer and Fredsøe 1989 characterized the flow around the cylinder in this range of Re with a completely turbulent wake and a laminar boundary layer separation both of which cause high pressure and large pressure drag in front of the cylinder. Therefore, turbulent wake flow, which plays an important role on the induced forces on the pipe, is well represented in the experiments.

3.7. Conclusions

The results of this study constitute the first part of a two-part work, presenting an experimental study on the impact of dam-break tsunami-induced hydraulic bores interacting with horizontally-mounted pipelines. The focus of this first part was on the flow hydrodynamics in dry and wet bed conditions and its changing characteristics in the presence of the pipe in the flow. The following conclusions are drawn from this research:

- For the dry bed condition, the bore front celerity increased with an increase in the impoundment depth. $\alpha = 1.2$ was suggested to be used in Equation (3.4) for the bore front celerity expression.
- The water surface profile and flow velocity, as well as the flow Froude number, were shown to change more gradually over the same period of time for small impoundment depths (i.e., $h = 30$ cm) compared to the waves generated by higher impoundment depths. Momentum flux was also smaller in the wave front region for $h = 30$ cm, due to a smaller flow velocity and water depth.
- Increasing the still water level downstream of the gate led to slower bore flow velocities, reduced Froude number, and reduced momentum flux compared to the bore produced by the same impoundment depth, but propagating over the dry bed. The flow regime changes from supercritical to subcritical with an increase in the still water depth and for $d/h > 0.3$.
- The presence of the pipe, for both dry and wet bed condition, caused the water level to rise and the flow velocity to decrease. In dry bed condition, smaller e/D values resulted in more abrupt water level rise at the time of the bore impact and a faster decrease in flow velocity.
- For bore propagating over dry bed, the water level increase at the time of bore impact in the presence of the pipe became larger with an increasing impoundment depth.
- In the case of the wet bed condition, increased level of pipe submergence S/D, due to increasing the still water depth d resulted in a reduction of the influence of the pipe on flow hydrodynamics. This was explained by a reduction in the flow blockage, due to the increased pipe submergence.

4. Experimental Study on Extreme Hydrodynamic Loading on Pipelines Part 2: Induced Force Analysis[2]

Abstract: Adequate design of pipelines used for oil, gas, water and wastewater transmission is essential not only for their proper operation but particularly to avoid failure and the possible extreme consequences. This is even more drastic in nearshore environments, where pipelines are potentially exposed to extreme hydrodynamic events, such as tsunami or storm surges induced inundation. The American Society of Civil Engineers (ASCE), in its ASCE7 Chapter 6 2017 on Tsunami Loads and Effects which is the new standard for tsunami impacts and loading, specifically stresses the need to study loads on pipelines located in tsunami-prone areas. To address this issue, this study is the first of its kind to investigate loading on pipelines due to tsunami-like bores. A comprehensive program of physical model experiments was conducted in the Dam-Break Hydraulic Flume at the University of Ottawa, Canada. The tests simulated on-land tsunami flow inundation propagating over a coastal plain. This allowed to record and investigate the hydrodynamic forces exerted on the pipe due to the tsunami-like, dam-break waves. Different pipe configurations, as well as various flow conditions, were tested to investigate their influence on exerted forces and moments. The goal of this study was to propose, based on the results of this study, resistance and lift coefficients which could be used for the design of pipelines located in tsunami-prone areas. The values of the resistance and lift coefficients investigated were found to be in the range of ($1 < C_R < 3.5$) and ($-2.8 \leq C_L < 2.8$), respectively. To that end, the study provides an upper envelop of resistance and lift coefficients over a wide range of Froude numbers for design purposes.

KEY WORDS: Pipelines, Extreme event, Tsunami, Dam-break wave, Drag force, Force coefficient.

4.1. Introduction

Pipelines located in coastal areas are important infrastructures which are used for gas and oil transportation, as well as for conveying and disposing of potable and wastewater, respectively. The Canadian Energy Pipeline Association (CEPA 2013) published a report on "Pipeline watercourse management" which focuses on damage to pipelines caused by natural hazards and proposes practices to ensure the safety of public and environment in the case of severe damages to operating pipelines in Canada. Safe design of pipelines in coastal areas is of critical importance as damage to these pipelines can have significant economic and environmental consequences. Different engineering criteria need to be considered as pipes located in the vicinity of coastal waters or in the shallow water region are subject to a variety of regular loading conditions, such as waves, tides, and nearshore currents, in addition to extreme loads, such as storm surges and tsunamis. Until now, the focus of research on pipe loading has exclusively focused on

[2] This section has been published as: Ghodoosipour, B., Stolle, J., Nistor, I., Mohammadian, A. and Goseberg, N. Experimental study on extreme hydrodynamic loading on pipelines part 2: Induced force analysis. *Journal of Marine Science and Engineering*, 2019, *7*(8), p.262.

hydrodynamic forces exerted in steady unidirectional or oscillatory flows for horizontal or vertical cylinders.

To study the hydrodynamic forces exerted on pipelines, understanding the flow behaviour around the pipe is critical. Several studies on flow behaviour around circular cylinders near a plane boundary (wall) have been performed.

Flow around a circular cylinder changes depending on the flow characteristics defined, among other parameters, by the cylinder Reynolds number:

$$\mathrm{Re} = \frac{Du}{\nu} \qquad \text{(Eq. 4.1)}$$

where D is the diameter of the cylinder, u is the flow velocity, and ν is the kinematic viscosity. The flow undertakes considerable changes with an increase in Re as the wake and boundary layer characteristics experience massive change. Details of such changes were given by Sumer and Fredsøe 1989. Vortex shedding behind an isolated circular cylinder, which occurs when flow turbulence reaches above a critical Reynolds number (Re = 40), is a commonly observed phenomenon which causes uncertainties in the estimation of the drag and lift forces. Due to the frequent vortex shedding occurring behind the pipe placed in flow, local pressure along the cylinder circumference changes and, hence, causes superimposing fluctuations to the drag and lift forces exerted on the cylinder (Lei et al., 1999). Drag and lift forces are usually expressed by their non-dimensional forms as drag and lift coefficient, respectively. Drag and lift coefficients depend on both the cylinder geometry as well as the incoming flow characteristics. In the case of horizontal cylinders close to plane boundaries, the turbulent characteristics of the flow in the region close to that boundary will change depending on the boundary properties such as its roughness. Such variations in the flow characteristics will affect the above-mentioned non-dimensional parameters.

The effect of the wall proximity on the exerted hydrodynamic forces as well as the properties of the vortex shedding on horizontal circular cylinders made the subject of intense research in the past. When pipelines are placed on the seabed, flow around the pipe may cause scouring of the bed material. This may lead to the pipe being suspended above the bed with an underlying gap, usually in the range from 0.1 *D* to 1.0 D (Sumer and Fredsøe 1989) . Above-ground transmission pipelines, installed in initially dry conditions, are also usually installed onto supports which ensure a prescribed distance between the pipe and the ground. When such pipes are accidentally flooded, this distance can significantly impact the flow around the pipeline. Therefore, it is important to understand the flow characteristics that occur in the proximity of such a pipe.

Several researchers have studied the induced forces on pipes placed near sea beds such as Aristodemo et al., 2011 who proposed a new numerical model for the estimation of the horizontal and vertical hydrodynamic forces induced on submarine pipelines exposed to non-linear wave and current conditions.

The parameter gap ratio, *e/D*, (*e* being distance between the lower edge of the pipe and the ground) is defined for the purpose of investigating the impact of bed proximity on flow hydrodynamics around the pipe. In the case of large *e/D* values (*e/D* > 1), the pipe acts similar to a free cylinder with no boundary effects.

Figure 4.1a defines the location of stagnation point (a point in a flow field where the local velocity of the fluid is zero) and separation point (the position where a boundary layer separates from the surface of a solid body) while Figure 4.1b illustrates the displacement of these

points in the existence of a plane boundary during a wave and/or current flow around a circular cylinder.

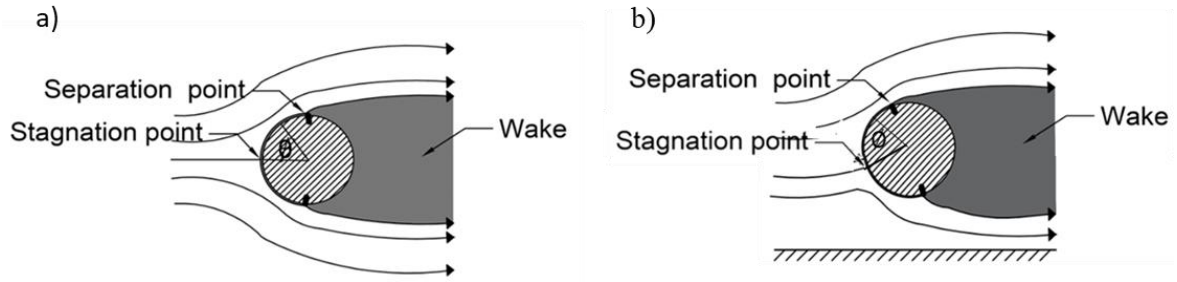

Figure 4.1. Schematic of the flow around a circular cylinder, stagnation and separation points. a) Free `cylinder and b) cylinder near a plane boundary (adapted from Summer and Fredose1989)

According to Sumer and Fredsøe 1989, flow around a cylinder placed close to the bed as shown in Figure 4.1b may change as follows depending on the gap ratio *e/D*: The angular position of the stagnation point ∅ displaces and moves to lower angles. Change in the gap ratio will also change the angular position of the separation point. As the gap ratio decreases, the separation point at the free-stream side of the cylinder moves upstream while the separation point at the wall side moves downstream. Vortex shedding suppression happens when $e/D < 0.3$ due to the asymmetry of the generated vortices on the free stream and wall side of the cylinder. Larger vortices on the free stream side interact with small vortices occurring near the wall and cause vortex shedding suppression compared to regular vortex shedding, which results in increased suction on the free side of the cylinder.

Most studies revealed a gap ratio of $e/D = 0.3$ as the distance for which vortex shedding suppression commences. Bearman and Zdravkovich 1978, Angrilli et al., 1982 and Zdravkovich 1985 supported this hypothesis by looking into the power spectra of hot-wire anemometer signals occurring in the wake region behind a cylinder. However, results from Buresti and Lanciotti 1992 show a gap ratio of $e/D = 0.4$ to be the critical gap ratio. The existence of vortex shedding causes the occurrence of a peak in the power spectra which disappears due to the suppression at a specific gap ratio.

A new topic in pipeline design has emerged due to the recent extreme events, such as the impact of pipelines by coastal flooding generated by tsunamis and storm surges, which caused massive damage to such infrastructure. Catastrophic events, such as the 2011 Tōhoku Tsunami in Japan and the 2012 Typhoon Haiyan in the Philippines, have increased the interest of researchers to re-evaluate existing design and safety standards to consider the effects of such extreme events. The American Society of Civil Engineers (ASCE), through its ASCE7 Tsunami Loads and Effects Committee, has developed a new standard for tsunami impacts and loading, the ASCE7 Chapter 6 (2017). Amongst the potential effects of such extreme events on infrastructure, the standard specifically emphasized the need to investigate tsunami loads on pipelines located in the flood zone.

Several research articles have focused on investigating forces induced by a hydraulic bore on infrastructure experimentally. Wind wave forces on cylinders have been the subject of many studies in the context of hydrodynamics (Summer et a. 1997) and coastal engineering studies (Li

and Lin 2001, Sundar et al., 1998). Qi et al., 2014 investigated the tsunami inundation forces exerted on structures using steady flow data. Several other studies such as Nouri et al., 2010, Arnason 2005, Al-Faesly et al., 2012, Bremm et al., 2015, Foster et al., 2017 evaluated the forces induced from tsunami wave-structure interaction under unsteady conditions. Aristodemo et al., 2017 conducted a small-scale experimental study in a wave flume along with a numerical investigation using an smoothed-particle hydrodynamics model. In their study they investigated the induced loading from a solitary wave on a horizontal circular cylinder.

Various guidelines are available for the design of buildings against tsunami loads and effects. Among them, the Federal Emergency Management Agency (FEMA, 2017) in the section related to the design of Structures for Vertical Evacuation from Tsunamis mentions different forces exerted on a body during a tsunami as follows:

- Hydrostatic and buoyant forces: Hydrostatic forces occur when still or slow-moving water interacts with a fixed body. The vertical component of the hydrostatic force is the buoyancy force. For partially or fully submerged bodies, the buoyancy force is exerted at the centroid of the displaced water volume.
- Hydrodynamic force: Also referred to as the drag force, it is caused by fluid flowing around a structure. Structure's geometry as well as flow characteristics and fluid density influence the magnitude and direction of the hydrodynamic force. The drag force is a combination of the pressure force from moving the mass of fluid as well as friction force between the flowing fluid and the structure. The hydrodynamic force is exerted at the centroid of the wetted surface and can be calculated as:

$$F_d = \frac{1}{2}\rho_s C_d B (h_w u^2)_{max} \qquad \text{(Eq. 4.2)}$$

where ρ_s is the water density, C_d is the drag coefficient, B is the width of the structure in the plane normal to the direction of flow, h_w is the water surface elevation or flow depth, and u is flow velocity at the location of the structure. C_d depends on both flow characteristics and the structure's geometry and orientation. FEMA (2017) suggests using a drag coefficient value $C_d = 2$, while the recent update to the ASCE 7 standard (2017) suggests values based on the width to inundation depth ratio and the type of structural component. Suggested C_d values in the ASCE 7 are in the range of $1.2 < C_d < 2.5$.

- Impulse force: Impulse or impact forces will act on a body when the leading edge of the bore reaches the structure rapidly. Several studies have focused on measuring and analyzing the impulse force on vertical structures. FEMA (2017) guideline refers to different studies such as Arnason 2005 and Ramsden 1993 and suggests an impulse force equal to 1.5 times the hydrodynamic force in the case of structural wall elements. Consequently, such forces will cause damage to the structural element as well as to the joints and may cause massive damage on the structure even when the hydrodynamic force is larger than the impulse force (Sundar et al., 1998, Palermo et al., 2012). The impulse force is usually followed by an increase in force magnitude as the bore flow accumulates in front of the structure causing a "bulb-like" wake. This force has been termed "run-up force" or "transient hydrodynamic force" (Palermo et al., 2012).
- Uplift force: Uplift forces are usually exerted on elevated surfaces that are submerged during tsunami inundation waves. In fact, water passes through a gap between the ground and the elevated surface remarkably fast during a tsunami and this induces uplift onto the bottom

surface of the elevated horizontal components. This uplift force will add to the hydrostatic vertical component (the buoyancy force). FEMA (2017) suggests a formula for computing the uplift force as:

$$F_L = \frac{1}{2} C_L \rho_s A_f u_v^2 \qquad \text{(Eq. 4.3)}$$

where C_L is the lift coefficient and ρ_s is the fluid density. FEMA (2017) suggests C_L = 3.0. A_f is the area of the floor panel, and u_v is the estimated vertical velocity or water rise rate.

The above-mentioned force components were previously addressed in studies and guidelines for the design of vertical evacuation structures. However, to the authors' knowledge, no study investigated the loads exerted in the case of tsunami inundation waves impacting horizontal circular cylinders or pipelines and there is a lack of knowledge regarding the characteristics of such loads on:

- Above-ground pipelines, placed at a given distance from the ground using supports.
- Fully submerged pipelines placed onto or near the ocean or sea bed.
- Partially submerged pipelines.

4.1.1. Objectives

Based on the above outlined lack of knowledge, this study details the findings in this second portion of a two-part work describing a comprehensive experimental program to investigate extreme hydrodynamic loading on pipes. The first part of this study (Ghodoosipour et al., 2019a), focused on the description of the experimental program and instrumentation, the hydrodynamics of the extreme flow generated, as well as the influence of the pipe presence on flow hydrodynamics. This second part details the results of the study with respect to the hydrodynamic forces measured and the calculation of the force coefficients. The specific objectives of this second part of the study are:

- Measuring and analyzing the changes in drag and lift forces exerted on the pipe due to a tsunami-like bore using different pipe elevations or gap ratios *e/D* for dry bed condition.
- Studying the effect of still water depth *d* and of the impoundment head to depth ratio *d/h,* d being the still water depth and *h* being the reservoir depth, on the various force components caused by tsunami-like dam-break wave on the pipelines in wet bed condition.
- Investigating the variation of the drag and lift forces exerted on fully and partially submerged pipelines with the different initial level of submergence ratio *S/D,* in order to examine the influence of the submergence on the force components.
- Studying the characteristics and the magnitude of the forces exerted on pipelines by dam-break waves generated using different reservoir impoundment depth *h*, for both dry and wet bed conditions.
- Proposing force coefficients for various flow conditions and pipe configurations.

It is anticipated that these results will lead to formulating recommendations for the optimal design of pipelines located in tsunami-prone areas, which will be both environmentally and economically safe during such extreme events. The research will also allow for better design and determine load conditions in regions subjected to potential natural hazards.

4.2. Experimental set-up

A comprehensive experimental program was designed and conducted in the Dam-break Flume in the Hydraulic Laboratory at the University of Ottawa, Canada. The flume is 30.1 m long, 1.5 m wide and 0.5 m deep. Various hydrodynamic parameters, as well as the forces exerted on the physical model of the horizontal pipeline (0.1 m in diameter and 1.47 m in length), were measured during the tests. Figure 4.2 illustrates the schematic view of the dam-break flume and location of instruments and the experimental parameters (impoundment depth and downstream water levels). Details of the experimental facilities and their characteristics are reported in the companion paper (Ghodoosipour 2019a). Table 4.1 presents an overview of the instruments used in the experiments and their specifications.

Table 4.1. Instruments used in the experimental program

Instrument	Manufacturer, Model	Sampling rate	Accuracy
Wave gauge (WG)	RBR WG-50, capacitance-type	300 Hz	±0.002 m
Acoustic Doppler Velocimeter (ADV)	Nortek, Vectrino	200 Hz	± 1 mm/s
Dynamometer	Interface- 6A68E	300 Hz	± 0.04%
High-speed Camera (HS)	Flare 2M360-CL	200 Hz	-

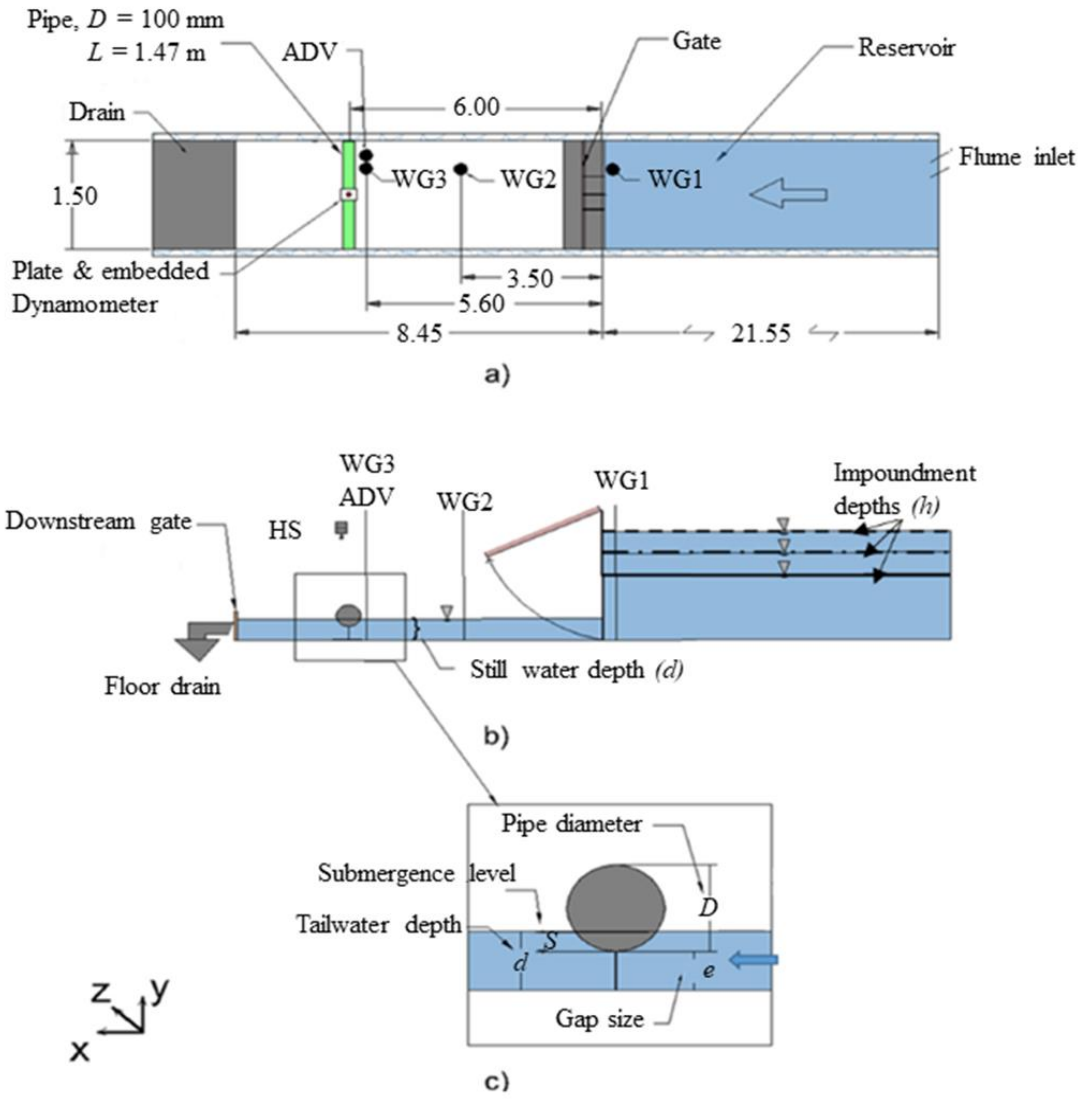

Figure 4.2. Experimental setting and instrument locations (unless otherwise specified, all dimensions are in m). a) plan view, b) side view and c) close view.

4.2.1. Experimental program

A comprehensive experimental study was conducted to investigate effects of design parameters on extreme hydrodynamic loadings on pipelines. Parameters considered in this study include: reservoir depth, *h*, still water depth, *d*, ratio of the lower edge of pipe distance to bed *e* to diameter, *e/D*, and pipe level of submergence, *S*, to pipe diameter ratio, *S/D*. An initial set of tests was performed without the pipe installed in the flume to investigate the initial hydrodynamic conditions.

The second set of tests were conducted with the pipe installed inside the flume to study bore-structure interaction and to measure and analyze the forces exerted on the pipe due to the impacting bore. The pipe was filled with water in all the conducted tests. A detailed list of experimental

parameters and results with respect to the hydrodynamics of this experimental program is presented in the companion paper (Ghodoosipour et al. 2019a).

4.3. Results and discussion

4.3.1. Flow hydrodynamics

The hydrodynamic properties of the generated dam-break waves were affected by the flume bed condition, i.e. dry and wet bed conditions. The dry bed condition represents the first tsunami-like wave flowing on land while the wet bed condition represents the following waves flowing on an existing layer of water remaining from earlier wave attack. The flow hydrodynamics at the location of the pipe for dry and wet bed conditions are described below. Details of the flow hydrodynamics throughout the entire flume as well as its change in the presence of the pipe is discussed in more detail in the companion paper Ghodoosipour et al., 2019a. However, due to consistency and completeness of this work, a summary of the evolution of the surface elevation, velocity and Froude number time-histories is presented below.

4.3.1.1. Dry bed condition

The flow characteristics at the pipe location were studied to analyze the forces exerted on the pipeline. Figure 4.3 illustrates the dry bed surge characteristics as the time-history of the water surface profile (WG3), the flow velocity and the Froude number at the location of the pipe, respectively. The reference time for all experimental tests is the bore arrival time at WG3. There is a delay in velocity measurements using ADV due to the air entrainment close to the wave arrival time which corresponds to the zone with no data in the first few seconds in Figure 4.3b and c. Time-history of the Froude numbers for dry bed condition and different reservoir heights are shown in Figure 4.3. It should be noted that for the impoundment depth of h = 30 cm, the water level increases and the flow velocity decreases more gradually compared to the cases with h = 40 cm and h = 50 cm. As shown in Figure 4.3c, the dry bed surge was supercritical, Fr > 1, throughout the studied time frame for all three impoundment depths. The Froude numbers remained almost constant in the case of h = 30 cm whereas it gradually decreases for h = 40 cm and h = 50 *cm*.

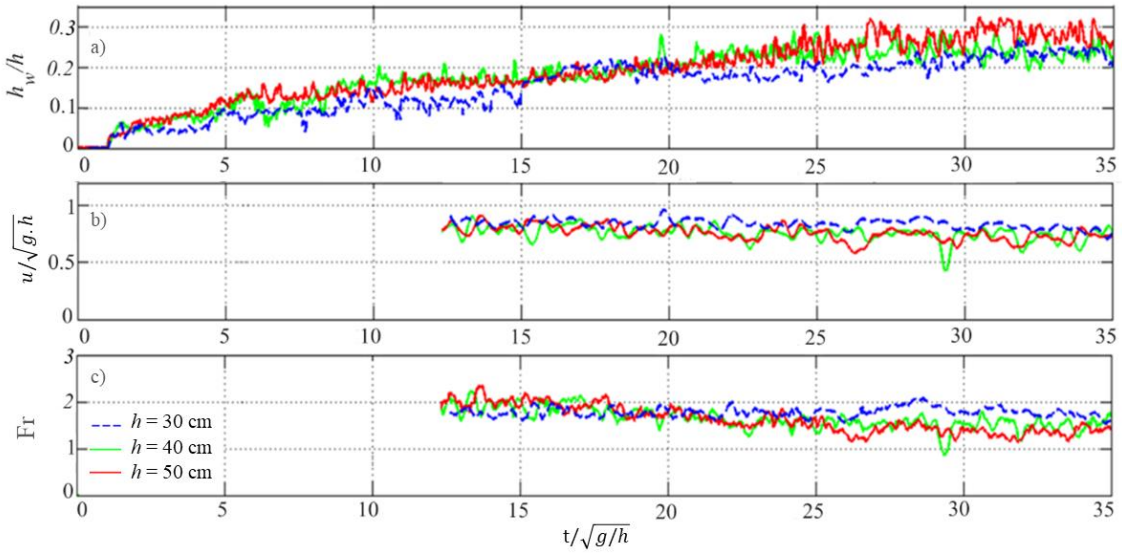

Figure 4.3. Dry bed surge characteristics at x = 6.5 for h = *30, 40, 50 cm*. a) water surface profile (recorded by WG3), b) flow velocity and c) Froude number.

4.3.1.2.Wet bed condition

Figure 4.4 shows the wet bed bore time-histories of the flow velocity and the derived Froude numbers for the cases where the wet bed condition was employed, for a constant impoundment depth, h = 40 cm, and for different d. The reference time for all the cases shown in Figure 4.4 is the wave arrival time to wave gage WG3. The flow velocity data at the beginning of the bore propagation were considered invalid and were eliminated from the graphs in Figure 4.4b,c, and d. Results show a noticeable decrease in flow velocity (Fig. 4b) and the estimated Froude number (Fig. 4c), with an increase in d/h ratio. This is because waves generated using a smaller pressure head (small difference between the impoundment depth and the downstream still water depth) result in slower flow velocities and smaller associated Froude numbers. Results from all the three tested impoundment depths, i.e., h = 30, 40, 50 cm, show that for d/h values larger than 0.3 flow was subcritical while for $d/h \leq 0.2$, the flow was supercritical. d/h values around 0.2 resulted in a critical flow regime with the Froude number magnitude fluctuating around 1.0. A similar trend was observed for the case with h = 30 cm and h = 50 cm.

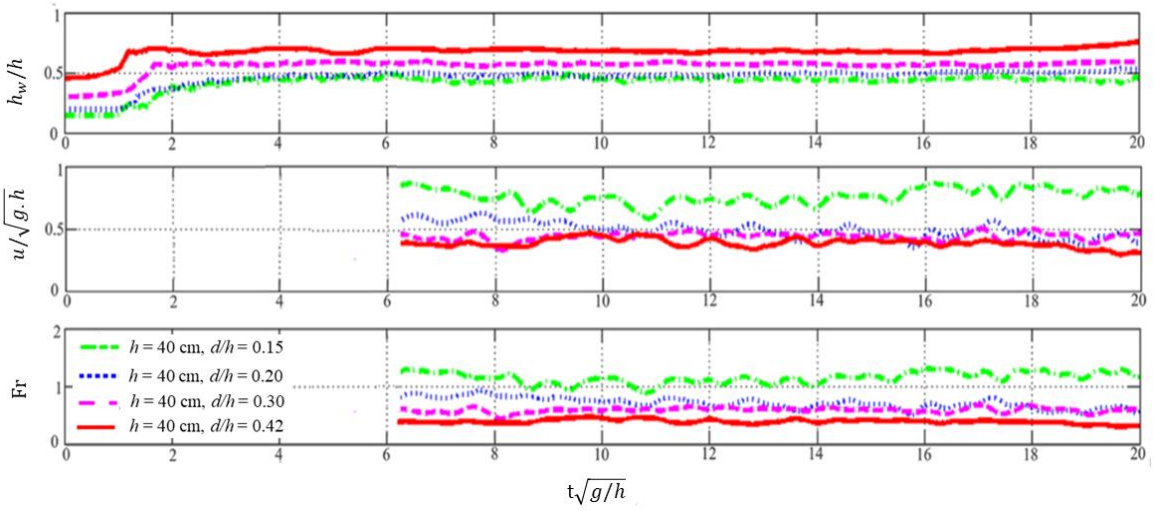

Figure 4.4. Wet bed bore characteristics at x = 6.5 for h = 40 cm, different line types correspond to different d/h values. a) Water surface profile at WG3, b) flow velocity and c) Froude number.

4.3.2. Drag and Lift forces

Results from tests using different impoundment water depths and water depth downstream of the gate for different *e/D* values in wet and dry bed conditions are presented in this section. For clarity, all results are shown starting 1.0 seconds prior to the wave arrival time. The force magnitude in vertical (lift) and horizontal (drag) directions were set to zero shortly before the start of each test to eliminate the effect of the latent hydrostatic forces as well as that of the pipe's own weight.

4.3.2.1. Force time-history for the dry bed condition

a) Influence of pipe gap ratio (*e/D*)

Figure 4.5 shows the results from a test conducted with a wave generated by an impoundment depth *h* = 40 cm in dry bed condition downstream of the gate. Figure 4.5a shows the water level time-history recorded by WG3 for the case with a gap ratio *e/D* = 0.3, while Figures 4.5b and 4.5c show the time-history of the water level for *e/D* = 0.6 and 0.8, respectively. The schematic of the pipe with the corresponding distance from the bed is shown in Figure 4.5a, b, c, for *e/D* = 0.8, 0.6, and 0.3, respectively, in order to visualize the level of the submergence and the full submergence time for each case. The water level for *e/D* = 0.3 rose rapidly immediately after the wave impact time while it gradually increased for cases with gap ratios of *e/D* = 0.6 and *e/D* = 0.8. Figure 4.5d shows the measured drag force time-history for the three gap ratios. In Figure 4.5d, one can observe that for e/D = 0.3, the drag force behaviour was considerably different when compared to data obtained using other e/D ratios. For this particular value of *e/D* = 0.3, an impulse force at the wave arrival instant was recorded whereas for the other two gap ratios e/D no such considerable force was recorded. In the cases with large gap ratio *(e/D* = 0.6 and *e/D* = 0.8), water passed through the gap for the first few seconds of the wave propagation. However, in the case of a smaller gap size (*e/D* = 0.3), less water passed through the gap and instead, a large portion of the incoming flow

separated from the bed and surged on top of the pipe. This observation can also explain the sudden rise in the water level for *e/D* = 0.3 at *t* = 1.5 s (half a second after wave arrival).

Hence, the impulse force was considerably larger for the test with *e/D* = 0.3 while a longer rise time was observed for the force to reach its maximum value for the tests with *e/D* = 0.6 and *e/D* = 0.8. A smaller volume of the water passing through the gap and shorter rise time for the tests with *e/D* = 0.6 when compared to that *e/D* = 0.8, resulted in higher water levels and larger drag forces at *e/D* = 0.6. For the test with *e/D* = 0.3, the water level reached the top edge of the pipe at *t* = 3.16 s. At this time, a surface roller formed right upstream of the pipe and started to propagate upstream causing a considerable decrease in the drag force. The surface roller was also observed in the case of vertical structure obstructing a dam-break flow impacting a column by S-Germain et al., 2013. For the other two gap ratios of *e/D = 0.6* and 0.8, the observed surface roller was much smaller in size and the upstream propagation speed was considerably slower. Therefore, only in the test with *e/D = 0.3*, a sudden decrease in the drag force was observed. After *t* = 4.4 s, when the pipe was submerged in all the three gap sizes, the lowest drag force magnitude was associated with the gap ratio *e/D* = 0.3. This could be explained by the small distance of the pipe to the bottom which caused the lower separation point to move downstream of the lower edge of the pipe while the upper separation point moved upstream of the upper edge. Such a separation point displacement by reduction of the gap ratio results in a smaller wake size at the back of the pipe which in turn results in a smaller drag force. This was observed and reported in previous studies (Lei et al. 1999, Bearman et al. 1978, Zdravkovichet al. 1985, Grasset al. 1984). Moreover, after full submergence, at smaller gap ratios (*e/D* < 0.3), vortex shedding suppression occurs due to the asymmetry of the vortices occurring at top and bottom of the pipe. Therefore, von-Karman vortex shedding behind the cylinder suppresses and causes smaller suction and smaller drag force exerted on the pipe.

The measured vertical (lift) force component time-history for the three gap ratios tested is shown in Figure 4.5e. This figure shows that the magnitude of the lift force increased considerably as the gap ratio decreased during the entire time-history. The variations observed in the time-history of the lift force occurs mainly due to the displacement of the stagnation point. At larger gap sizes, the stagnation point moves away from the plane boundary which causes a considerable decrease in the lift force. A large gap ratio also diminishes the plane boundary effect and the pressure distribution becomes symmetric. As a result, both the drag and lift forces decrease considerably. Moreover, at the beginning of the surge, the lift force at *e/D* = 0.8 was extremely small due to the longer duration it takes for the wave to reach the lower edge of the pipe. The downward-oriented lift force at the beginning of the bore surge at *e/D* = 0.3 can be explained with the large volume of water surging on top of the pipe immediately after the bore impact time which pushes the pipe towards the flume bed. After the first impact, this downward vertical force was not observed in the tests when *e/D* = 0.6 and *e/D* = 0.8 as the flow passed through the gap. Figure 4.5f shows the total force which was calculated using the following equation:

$$F_T = \sqrt{F_D^2 + F_L^2} \qquad \text{(Eq. 4.4)}$$

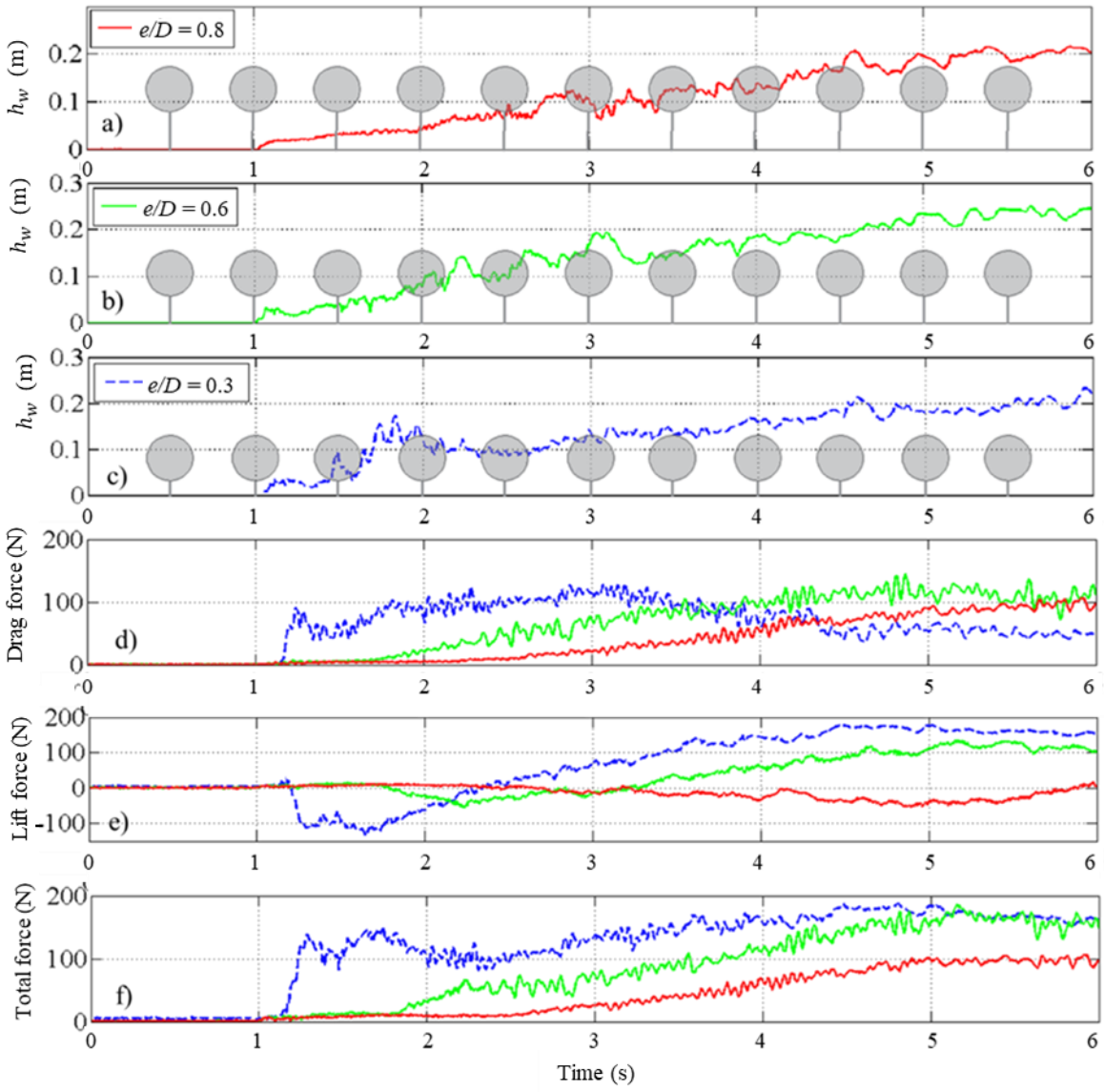

Figure 4.5. Time-history of the water level and the drag and lift force component measurements, dry bed condition, impoundment depth h = 40 cm. a) Water level with e/D = 0.8, b) water level with e/D = 0.6, c) water level with e/D = 0.3, d) drag force time-history for e/D = 0.3, 0.6, 0.8, e) lift force time-history, e/D = 0.3, 0.6, 0.8 and f) total force e/D = 0.3, 0.6, 0.8.

Results from Figure 4.5 indicate that the total force increased considerably as e/D decreased with the highest values recorded for the tests when e/D = 0.3. This is due to the larger drag and lift force observed at smaller gap ratios. The same trend in the force time-history was observed for the tests with the reservoir impoundment depth of h = 50 cm and h = 30 cm.

b) Influence of the impoundment depth

Figures 4.6 shows the water level and the force components for different reservoir impoundment depths for the smallest e/D ratio used in the tests (e/D = 0.3). As expected, due to

the larger initial head which translated into the dam-break wave with the highest flow depth, the reservoir depth h = 50 cm generated the largest force components magnitudes (as shown in Figure 4.6b). As discussed in the companion paper (Ghodoosipour et al., 2019a), higher impoundment depths leads to higher flow velocities and bore heights. This, in turn, increased the exerted drag force. For the impoundment depth h = 30 cm, the impulse force was considerably smaller compared to the two other larger impoundment depths. Waves generated using larger reservoir depths, exhibited significantly steeper bore fronts, which impacted the pipe front face and caused a sudden water level rise and a larger impulse force at the time of bore impact. Figure 4.7 shows the more abrupt water level rise which results in a larger impulse force in higher reservoir depths. For the cases with larger impoundment depth (h = 50 cm and h = 40 cm), large standing waves are generated in front of the pipe after the initial impact. After (t = 4) the standing waves dissipated and started to move upstream towards the gate as surface roller which resulted in a decrease in the drag force. In the case of the smallest impoundment depth h = 30 cm, standing waves and a returning surface roller were not observed. Therefore, the drag force increased gradually until reaching the maximum magnitude and remained then constant.

The lift force time-history in all three cases showed a downward peak which became larger with an increase in the reservoir impoundment depth from h = 30 cm to h = 50 cm. In Figure 4.6c, the negative peak of the vertical force (Fz) varied from −25 N to −50 N and to −150 N for water depths h = 30, 40, and 50 cm, respectively. This is due to the larger amount of water surging over the top of the pipe and pushing the pipe downwards as the wave was larger. The lift force was generally larger for waves generated by the larger reservoir depths, mainly due to higher flow velocity of the dam-break waves generated with higher impoundment depths. The total force magnitude which is a function of the combination of the drag and lift forces was maximum for waves generated using the h = 50 cm impoundment depth (Figure 4.6d).

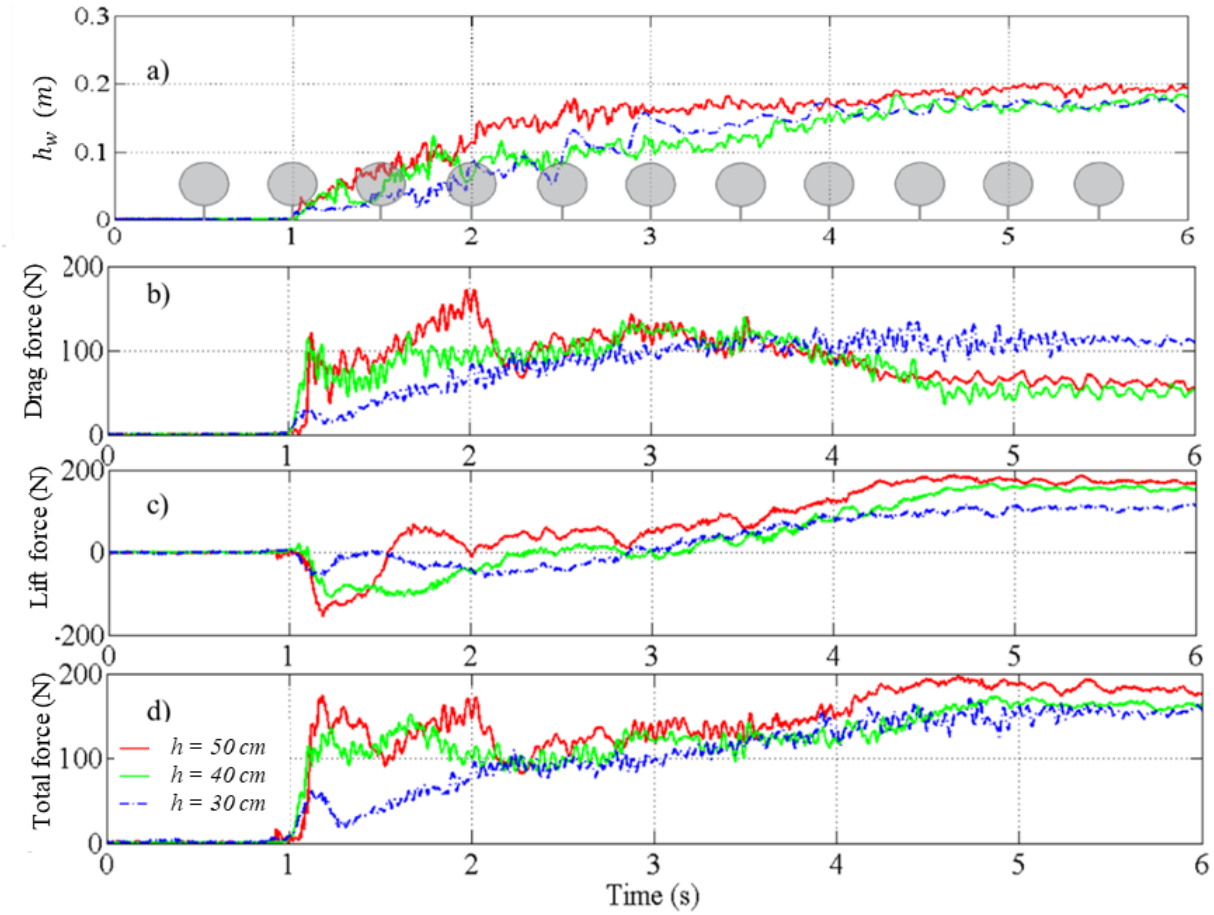

Figure 4.6. Time-history of the measured water level and force components for dry bed condition, *e*/*D* = 0.3 and impoundment depths *h* = 50, 40, 30 cm a) water level at WG3, b) drag force time-history, c) lift force time-history and d) total force time-history.

Figure 4.7. Bore impact on the pipe on the pipe for three impoundment depths: a) *h* = 50 cm, b) *h* = 40 cm and c) *h* = 30 cm.

4.3.2.2. Force components for wet bed conditions

a) Influence of pipe gap ratio (*e/D*)

Figure 4.8 shows hydrodynamic force components in the case of the wet bed condition for a wave generated by an impoundment depth h = 40 cm and a relative downstream water level, d/h = 0.2. For these same initial forcing conditions, considerable changes in the hydrodynamic force time-history pattern can be observed at the time of bore impact when compared to the case with a dry bed condition: in wet bed condition, the horizontal impulse force shown in Figure 4.8d, for all three gap ratio values, is significant compared to the case of a dry bed (Figure 4.5d). In wet bed condition, the gap between the pipe and the boundary was filled with water. Therefore, unlike the dry bed case where the flow passed through the gap and gradually reached the pipe, the bore impacted the entire pipe cross section at the bore arrival time, resulting in a large impulse force. Moreover, according to Yeh 2007, the impulse force increases due to the impact of a steeper bore front onto the object in the path of the flow. Hence, the absence of a clear impulse force for the case of the dry bed condition can be attributed to the significantly milder slope of the bore as discussed in the Part 1 companion paper (Ghodoosipour 2019a). From Figure 4.8d, it can be concluded that, for the wet bed condition, the drag force magnitude during the impact time, does not change drastically by changing the gap ratio (*e/D*). Since for the wet bed condition, the gap between the pipe and flume bed was partially or completely filled with water prior to the arrival of the bore, the effect of the gap ratio and boundary conditions, such as bed roughness, separation and stagnation point, on the recorded force components are also decreased. Only the horizontally-directed impulse force subsided in magnitude as the pipe was further submerged by the incoming bore and as the gap ratio decreased. This was due to an increase in the effective contact area of the pipe with the incoming surge by a lower initial level of submergence.

Similar to the drag force time history for the wet bed condition, results of the lift force time history in Figure 4.8e show a considerable initial impulse vertical force. The general trend for the lift force time-history e/D = 0.6 and 0.8 with a smaller initial submergence ratio (S/D < 0.3) was observed, where increasing e/D led to increase in the impulse lift magnitude. However, for e/D = 0.3, with the initial level of submergence, S/D = 0.5, the pipe was totally submerged right after the bore impacted the pipe and vertical force exhibited an oscillatory behaviour with smoother changes in its time-history. The maximum peak of the lift force was observed for the smallest gap ratio (e/D = 0.3) due to the increased suction forces on the free-stream side of the pipe. No distinct difference between the results for different gap ratios was observed in total force time history (Figure 4.8f).

b) Influence of the wet bed still water depth d and submergence ratio S/D

Figure 4.9 shows the results for the water depth, the drag force, lift force and the total force for different still water level depths downstream of the gate for the case of e/D = 0.6. The d/h ratio was adjusted by varying the still water depth d and using a constant impoundment depth h which resulted in different levels of pipe submergence S/D as shown in Figure 4.9a.

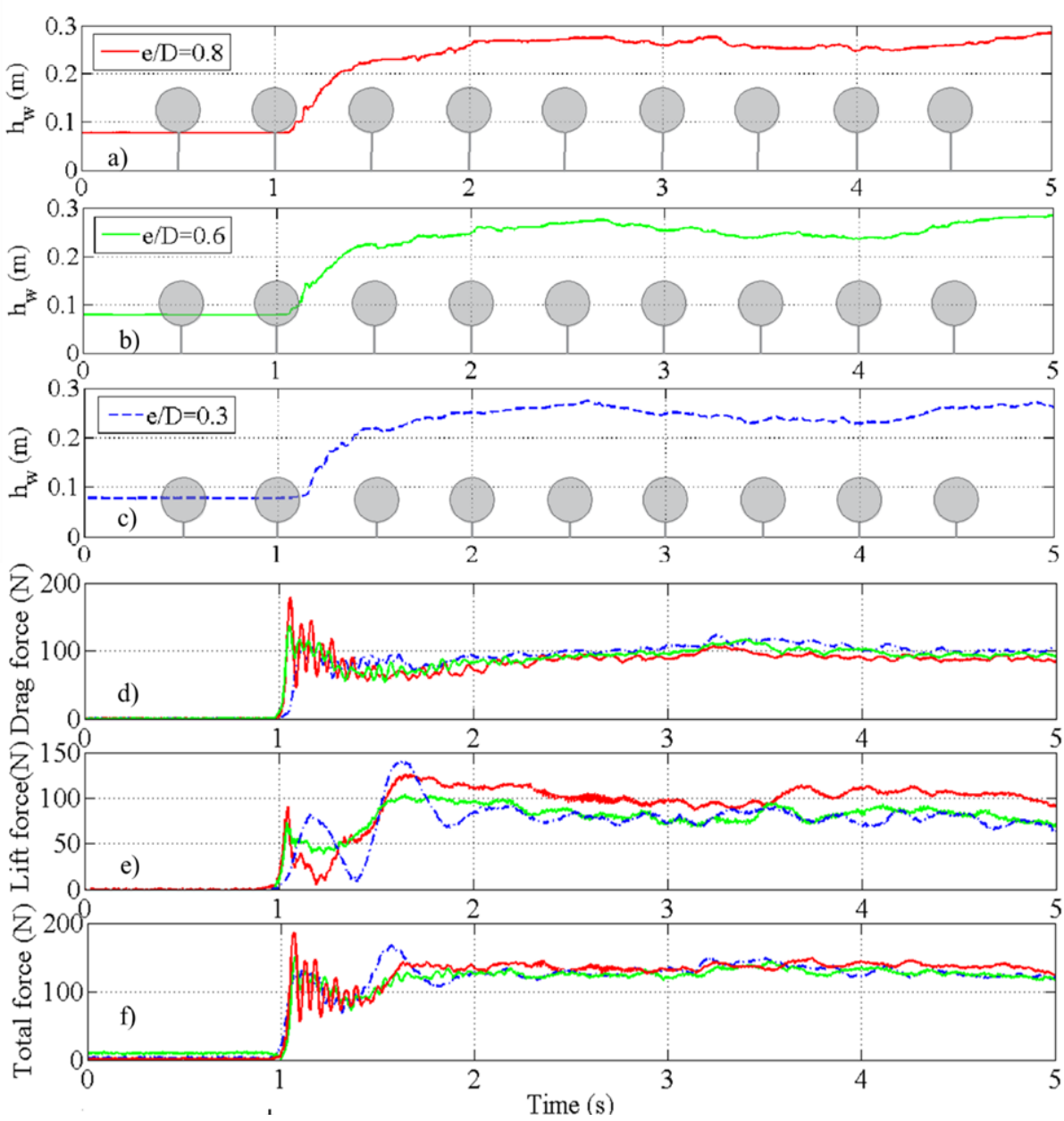

Figure 4.8. Time-history of the water level and force component measurements at WG1 wet bed condition, impoundment depth h = 40cm, still water depth *d = 8cm*, and *d/h* = 0.2: a) water level *e/D* = 0.8, and *S/D* = 0, b) water level for *e/D* = 0.6 and *S/D* = 0.2, c) water level for *e/D* = 0.3 and *S/D* = 0.5, d) drag force time history, *e/D* = 0.3, 0.6, 0.8, e) lift force time history for *e/D* = 0.3, 0.6, 0.8 for f) total force for *e/D* = 0.3, 0.6, 0.8.

The time history of the drag force (Figure 4.9b) shows that for *S/D* = 0 (the pipe not being submerged at the initial stage before opening the gate), the drag force initially exhibited an initial bore impact (impulse force) and further decreased to lower magnitudes afterwards. When the initial still water level was below the bottom edge of the pipe (*d/h* = 0.075), the measured run-up force was larger compared to the impulse force just a few seconds after the bore impact. However,

when the pipe was partially submerged with $S/D < 0.5$, the impulse force was the maximum one. For $S/D \geq 0.5$, a smaller impulse force was observed and the magnitude of the drag force remained constant as the pipe became fully submerged. In the case of a fully submerged pipe with $S/D = 1$, no considerable impulse force was recorded and a gradual drag force magnitude increase was observed, mainly due to an increase in the flow velocity. The run-up force was caused by the pipe obstructing the flow. Therefore, as the pipe was increasingly submerged, this force decreased. This occurred faster for the pipe with a larger initial level of submergence.

The time history of the lift force shown in Figure 4.9c, indicates a decrease in this force's magnitude with an increase in *d* and, as a result, an increase in the initial *S/D* ratio. Lowest values were observed for the case of the fully submerged pipe (*S/D* = 1). In this case, incoming flow only passed over the top of the pipe inducing small, mostly downward, vertical forces. Downward lift force at the time of the bore impact for the cases when *S/D* = 0 is due to the volume of water surging on top of the pipe at the time of bore impact. The rapidly-surging water further pushed the pipe downwards. Figure 4.9d shows the decrease in the total force time history with an increase in the d/h ratio and an increase in *S/D*. As discussed in the companion paper Part 1, a significant decrease in flow velocity was observed as the downstream still water level was increased. This explains the smaller force component magnitudes in larger *d/h* ratios. A similar trend in total force time histories were observed for the case when *e/D* = 0.3 and *e/D* = 0.8.

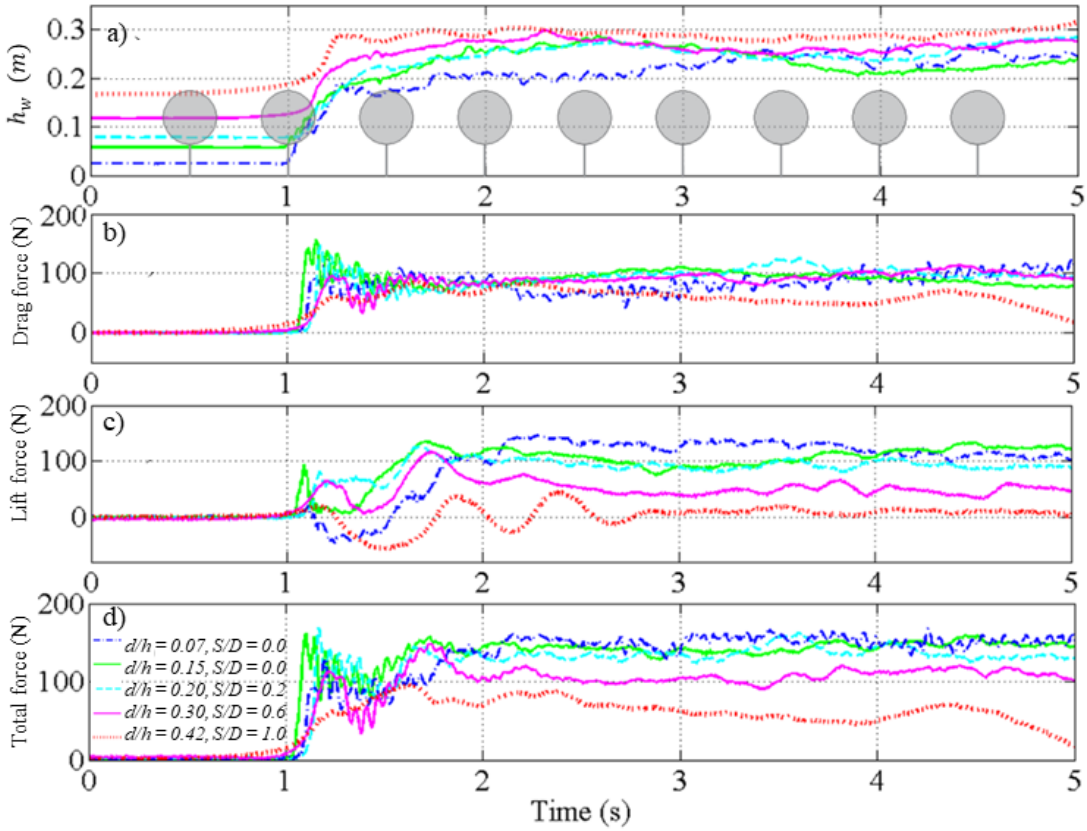

Figure 4.9. Time-history of the water level and force component measurements at WG3 for wet bed condition, different *d/h* ratios (*d/h* = 0.075, 0.15, 0.2, 0.3, 0.42), *e/D* = 0.6: a) water level b) drag force time history, c) lift force time history, d) total force.

4.3.3. Force Coefficients

Force coefficients are used to determine the drag and lift forces exerted on a body placed within flow. Current design guidelines recommend force coefficient values for different bodies including horizontal cylinders exposed to steady flow conditions. For the case of unsteady flow conditions, force coefficients have been suggested mostly for vertically-oriented bluff bodies. For the first time, this research investigates the variation of force coefficients for horizontal cylinders placed in unsteady flow conditions (dam-break waves). Due to the unsteady nature of the dam-break flow, force coefficients are not constant but vary considerably over the duration of the flow-structure interaction (Arnason 2005). In this study, the measured horizontal force incorporates both the hydrodynamic and hydrostatic components. Therefore, the term "resistance coefficient", rather than "drag coefficient" was used for the experimentally-determined horizontal force coefficient similar to studies by Gupta and Goyal 1976 for steady flows around bridge piers and Arnason 2005 for tsunami impacts on vertical structures. The resistance coefficient for different pipe configurations, different impoundment depths and different wet bed conditions downstream of the gate, were calculated using:

$$C_R = \frac{2F_H}{\rho L D u^2} \qquad \text{(Eq. 4.5)}$$

where F_H is the measured horizontal force during the experimental work; D and L are the pipe diameter and pipe length, respectively. u is the depth average free stream velocity as the average of ADV measurements at the highest water level, the location where the pipe center was later placed and 0.03 m above the bed.

The lift coefficients were calculated using:

$$C_L = \frac{2F_z}{\rho D L u^2} \qquad \text{(Eq. 4.6)}$$

where F_z is the measured vertical force.

Figure 4.10 shows the calculated resistance coefficient values as a function of the Froude number for all experimental cases. Due to the flow being transient, full time-history of the measured horizontal force was used to calculate the force coefficient. The values of the maximum estimated resistance coefficients were used to define an upper envelope for the resistance coefficients, C_R. In the case of the dry bed condition, due to the higher flow velocities, the values of the resistance coefficients are found at the right side of the graph, corresponding to the larger Froude numbers which characterized this particular condition. Based on the results presented in Figure 4.10 the suggested C_R values vary between 1.0 to 3.5. Figure 4.10 shows that for the case of supercritical flows (Fr > 1), C_R was almost constant while it has linearly increased with a decrease in the Froude number in the subcritical flow regime (Fr < 1). The black line in Figure 4.10 represent the upper envelope encompassing the entire range of experimental cases, from non-critical to supercritical flow condition. As shown, it covers a variety of submergence conditions, gap width as well as both wet and dry bed conditions. The previous study by Li and Lin (2010) on induced forces by waves and currents on horizontally submerged circular cylinders suggest drag coefficients in the range of $0.6 < C_D < 5.0$ for waves and $0.7 < C_D < 4.0$ for currents.

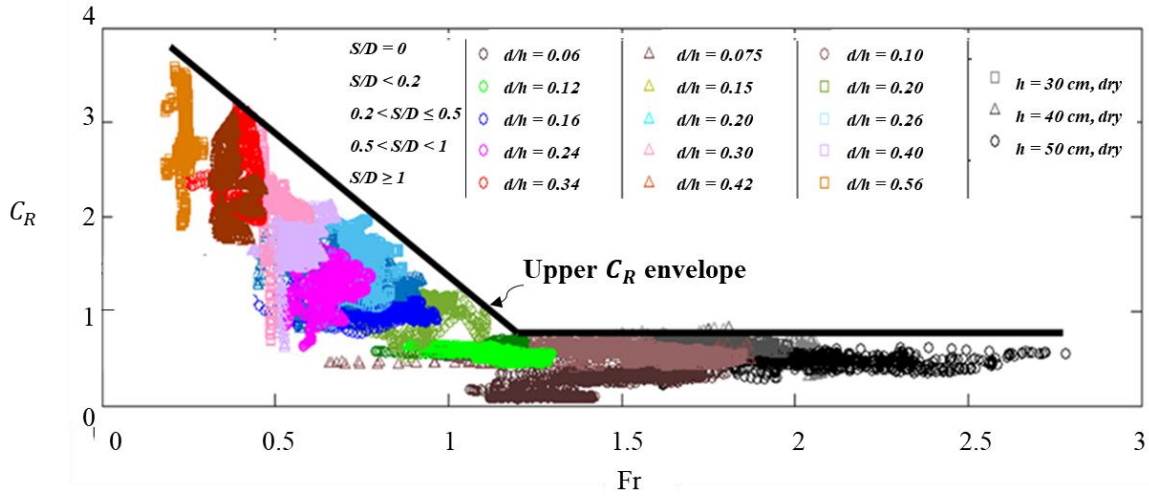

Figure 4.10. Calculated resistance coefficient versus Froude number for all the experimental cases tested in this study.

Similar to the resistance coefficient, the experimentally determined lift coefficients were plotted against the calculated Froude numbers (Figure 4.11). The maximum lift coefficients for all experimental cases were calculated by the authors to further propose an upper C_L envelope. This study suggests that C_L values for pipelines in unsteady flow conditions vary in the range of (-2.8 $\leq C_L <$ 2.8). Similar to the resistance coefficient behavior, C_L remained almost constant in the supercritical flow region while it increases as the value of Fr decreases in the subcritical flow region. Li and Lin (2010) suggest lift coefficients in the range 0.6 < C_L < 6 for horizontal circular cylinders impacted by waves and 1.5 < C_L < 4 for cylinders impacted by currents.

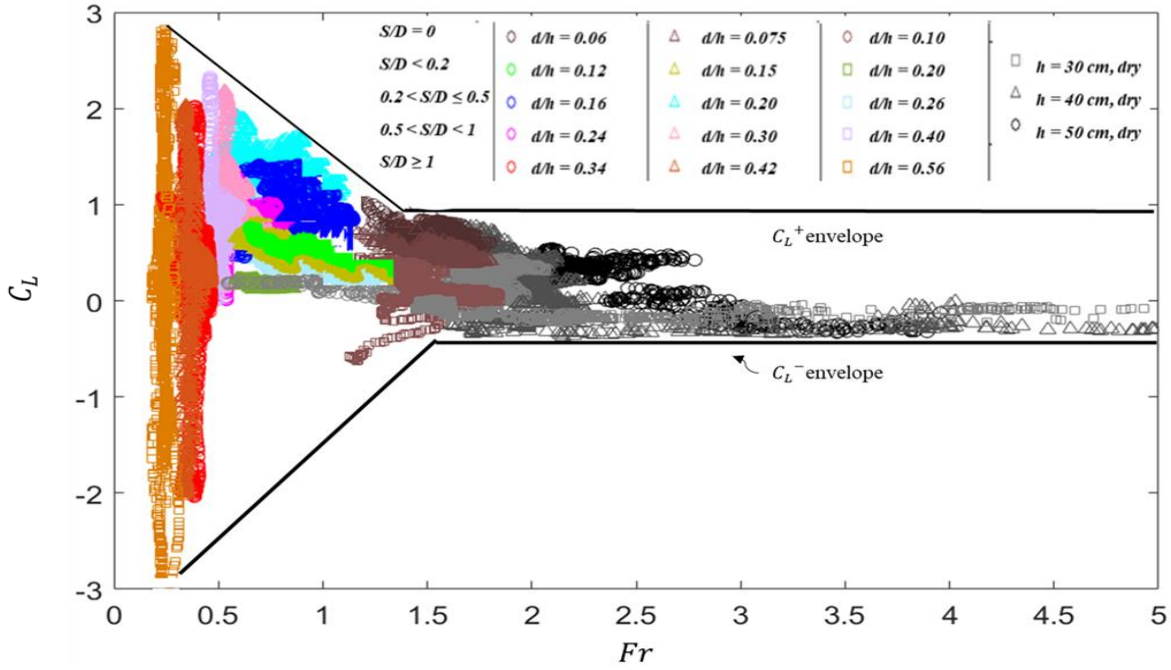

Figure 4.11. Maximum calculated lift coefficient versus Froude number for all the cases tested in this study.

4.4. Conclusion

A comprehensive experimental program was conducted to investigate the mechanisms of the extreme hydrodynamic loading exerted on a pipe due to tsunami-like hydraulic bore flows. The time-history of the hydrodynamic forces exerted on the pipe was measured and analyzed for different experimental conditions with respect to the pipe installation (distance/gap from the bed) as well as the flow characteristics (degree of submergence and hydraulic bores with different heights as well as dry versus wet bed conditions over which the bore propagated.

Dam-break waves generated using higher reservoir impoundment depths propagating over dry bed resulted in larger drag and lift forces due to considerably higher flow velocities compared to the case of the wet bed condition for the same impoundment depth.

Under dry bed condition, the horizontal impulse force, observed at the initial impact of the bore, was considerably larger for smaller *e/D* i.e. $e/D \leq 0.3$. The small gap space between the pipe and the bed led to a full impact of the steep bore front. However, after the complete submergence of the pipe, the magnitude of the horizontal force decreased due to vortex shedding suppression. The lift force time history for the dry bed condition showed larger lift forces for smaller e/D ratios due to the asymmetry in pressure distribution at the bottom and top of the pipe when this was placed close to the bed.

Changing the pipe distance to the bottom (gap ratio, *e/D*) for the wet bed condition did not significantly alter the force components. However, the impulse force recorded in the case of the wet bed condition was considerably larger for the same relative impoundment depth when compared to the same wave propagating under dry bed condition. This is due to the impact of a steeper bore front onto the entire pipe at the initial impact.

The effect of the downstream still water depth *d* was investigated and it was concluded that for *d/h* ratios corresponding to a smaller initial level of submergence *S/D*, the impulse force was considerably larger compared to the cases with larger submergence levels. For the case of the fully submerged pipe *S/D* = 1, no impulse force was observed due to the elimination of effective contact area of the pipe exposed to surge.

The pipe resistance coefficient exhibits lower values for the case of supercritical flow conditions (Froude number larger than 1.0), for both the dry and the wet bed conditions. This study suggests force coefficient values for various Froude numbers and several pipe configurations. The wide range of suggested force coefficients for various flow and pipe characteristics could be extremely helpful for design purposes. The suggested resistance coefficients are in the range of $1 < C_R < 3.5$ and lift coefficient values in the range of $-2.8 \leq C_L < 2.8$ for the experimental conditions investigated.

5. Modelling of extreme hydrodynamic loading on pipelines[3]

Abstract: Extreme hydrodynamic events such as tsunamis and storm surges have caused drastic damages to the coastal infrastructures in recent years. Horizontal transmission pipelines in coastal areas are among the most vulnerable infrastructures prone to such damages and need to be properly designed to withstand the extreme hydrodynamic events. This study investigates the induced extreme hydrodynamic loading on horizontal pipelines using Computational Fluid Dynamics (CFD) numerical modeling. The developed numerical model replicated a set of experiments investigating tsunami-like dam-break wave induced hydrodynamic loading on horizontal pipelines conducted by the authors at University of Ottawa, Canada. Different turbulence models were tested and results were validated against the experimental results. Renormalization Group (RNG) $k-\varepsilon$ model proved to have the best performance among all different tested turbulence models with a smaller error compared to the experimental results. The impact of different parameters such as distance of the pipe to bed to pipe diameter ratio (e/D), bed roughness and pipe diameter on the induced forces were investigated numerically using RNG $k-\varepsilon$ turbulence model. Findings from this study can enhance our understating of extreme hydrodynamic loading on horizontal pipelines caused by extreme hydrodynamic events which can be used for proper transmission pipeline design.

5.1. Introduction and Research Needs

Proper design of pipelines used for oil, gas, water and wastewater transmission is of great importance. As such, a clear understanding of the external forces exerted on pipelines is crucial. Flow around circular cylinders and pipes such as offshore pipelines is complex and had long made the object of research and engineering investigations. The correct estimation of hydrodynamic loading on pipelines requires a comprehensive understanding of the flow field around them.

Experimental studies have been previously conducted by researchers such as Bearman and Zdravkovich, 1978, Zdravkovich 1985, Lei et al. 1999, and Nishino et al. 2007, with the purpose of investigating flow around a circular cylinder placed near a plane boundary. These studies suggest that the flow characteristics and the associated hydrodynamic loading on cylinders are governed, aside from the object geometry and flow velocity, by the turbulence intensity characterized through the Reynolds number, as well as on the space between the cylinder and the ground.

[3] This section has been submitted as: Ghodoosipour, B., Nistor, I. and Mohammadian, A. Modeling of extreme hydrodynamic loading on pipelines. *Journal of Coastal Engineering*.

Lee et al. 1994 presented a finite difference solution to the two-dimensional (2-D) Navier–Stokes equations with a Subgrid-scale (SGS) turbulence model. Comparisons showed good agreement of their numerical results with the experimental measurements of Bearman and Zdravkovich 1978. Chaplin and Subbiah 1997, conducted experimental work to investigate the induced forces and pressure distributions on horizontal cylinders induced by steady current, with and without regular waves. They employed the results of their study to evaluate the Morison equation formula (Morrison et al. 1950) in predicting loading forces on horizontal cylinders. In conclusion, they found that Morrison's formula is most of the time accurate in predicting horizontal forces on horizontal cylinders. They also showed that the obtained force coefficients for horizontal cylinders are similar to those obtained for vertical cylinders and that induced forces are insensitive to the downstream wake and wave-induced vortices around horizontal cylinders at moderate to high Keulegan–Carpenter number (K_C) numbers. Tong et al. 2017 investigated flow hydrodynamics and the induced forces on horizontal submarine pipelines caused by currents using Large Eddy Simulation (LES) numerical modeling. They evaluated the magnitude of the drag coefficient on cylinders placed close to the sea bed and concluded that the drag force on the spanning side of the cylinder is slightly smaller. They also concluded that forces and pressure distributions alter due to the flow deflection from spanning to non-spanning sections of the pipe.

Flow hydrodynamics and induced forces on pipelines by regular and irregular waves have also been investigated. Experimental studies such as those of Subbiah et al. 1991 and Geo et al. 2002, showed that pipe vibration generated by vortex shedding caused by pressure gradient around pipelines is larger in magnitude in irregular waves compared to regular waves.

Bai et al. 2017, studied the wave-current interaction with horizontal cylinders with different submergence levels, both experimentally and numerically, for small K_C numbers (K_C <4). Their experimental test was conducted using a combination of current and two regular waves with the same wave height and length and measuring the induced forces on a horizontal cylinder. The numerical study was performed using Volume of Fluid (VOF) method to be able to capture the free water surface and Renormalization Group (RNG) k-ε model for turbulence modelling. The study showed that induced forces are larger than the predictions provided by Morison's formula for partially submerged cylinders. They also found that, for the fully submerged cylinders, only the wave blockage is influential; hence, the forces exerted on the cylinder are lower compared to those calculated with Morison's formula.

Li et al. 1997 performed finite element analysis using both the two-dimensional (2-D) and the three-dimensional (3-D) Navier–Stokes equations with a Large Eddy Simulation (LES). Lei et al. 1999, 2001, performed 2-D and 3-D direct numerical simulations (DNS) to study the wall effects on the flow over a circular cylinder for relatively low Reynolds numbers. Kawamura et al. 2002, performed a numerical study using Large Eddy Simulation (LES) to study the flow and hydrodynamics around a vertical circular column in turbulent flow. The unsteady Reynolds-averaged Navier–Stokes (URANS) and detached-eddy simulations (DES) were tested by Nishino

et al. 2008 to study the flow around a circular cylinder placed near a plane boundary. Breuer 1998, 2000 performed Large-Eddy Simulations (LES) in a uniform cross-flow. He was able to validate the model successfully but found the LES method to be computationally expensive.

A new topic in pipeline design has emerged due to effects of recent extreme events such as tsunamis and storm surges. Such extreme events have caused serious damage to the communities in coastal areas. To mitigate the damage from such extreme events, previous researchers have undertaken detailed studies on the processes involved and the type of damage such events cause to infrastructure. Several of them attempted to conduct experimental studies to replicate events similar to tsunamis at laboratory scale. Ramsden 1996, conducted a laboratory experiment to study the interaction of a turbulent bore with a vertical wall. Arnason 2005, studied the interaction of a broken tsunami-like bore with structures with various cross-sections. Leal et al. 2006, performed a series of experimental tests to study flow hydrodynamics in the case of dam-break waves for different bed conditions such as bed roughness. Numerical modelling approach has been widely used for studies on this topic. Gomez-Gesteria and Dalrymple 2004, used the Smooth Particle Hydrodynamics (SPH) method to investigate the flow hydrodynamics around and induced forces onto a tall vertical structure from a dam-break wave in both dry and wet bed conditions. They were able to validate their results with the available experimental data. Douglas and Nistor 2014, developed a three-dimensional multiphase numerical model to study the effect of the bed condition (i.e., wet vs. dry bed) influence on induced forces in the event of tsunami-like bore interaction with a square structure. Wei et al. 2015, developed a SPH model to investigate the interaction of bore with bridge piers and found a direct relationship between the hydrodynamic forces and the dimensionless width of the flume.

Haley et al. 2014, investigated hydrodynamic loading on a slender horizontal cylinder from an extreme wave event represented with a very steep breaking wave. Results from this study showed that as a wave approaches the breaking limit and its steepness increases, the resultant vector of the drag and lift force components deviates significantly from the normal to the water surface direction. They also showed that this force declination depends on the inundation depth upstream of the cylinder.

Xiao et al. 2013, investigated the interaction of a solitary wave and a uniform current and the associated induced forces on horizontal cylinder numerically using k-ε turbulent model. The model was validated using experimental data and solitary wave analytical solutions. Results showed that the forces from combined wave and current are larger than linear sum of wave force and current force.

Aristodemo et al. 2017, investigated the forces induced by solitary waves on submerged horizontal circular cylinders both experimentally, in a wave flume, and numerically, using a diffusive weakly compressible Smoothed Particle Hydrodynamics (SPH) model. Results showed that inertia force

is dominant and influences significantly the horizontal and vertical force time-history as well as the peak values in the range of the wave characteristics tested, i.e., ($0.08<A/d<0.2$, $Re \cong 10^4$ and low K.C. numbers).

Zhao et al. 2019, numerically investigated induced forces on submarine pipelines from solitary waves and a more realistic tsunami wave based on N-wave theory as well as according to data derived from the March 2011 Tohoku Tsunami in Japan. The tsunami wave was modeled by simulating a piston-type wave maker using a dynamic mesh and the wave profile was approximated using a combination of three sech2 wave profiles. The effects of different parameters such as the wave height, water depth, pipeline diameter, and gap between the pipe and the bed to diameter ratio on the hydrodynamic characteristics of submarine pipelines were investigated. Results showed that peak hydrodynamic forces due to tsunami-like waves are larger than those generated by the solitary wave with the same characteristics. Moreover, the duration of the acting force due to the tsunami-like wave was much longer than that of the solitary wave. It was also shown that the hydrodynamic forces of the pipeline under the tsunami-like wave increased with the wave height, but decreased as the water depth increased.

The American Society of Civil Engineers (ASCE)), in its ASCE7 Chapter 6: Tsunami Loads and Effects, the new standard written in mandatory language to assess the tsunami impacts and loading outlined the necessity to study tsunami loading on pipelines during such events. Understanding the hydrodynamic forces acting on the pipelines is vital to ensure their safe operation and to avoid potential damages to the environment. Hence, the authors of this study performed a comprehensive experimental program on the hydrodynamic loading onto horizontal pipelines with different pipe geometry and placement conditions due to tsunami-like turbulent bores (Ghodoosipour et al., 2019 a & b).

The objectives of the current numerical modelling study on extreme hydrodynamic forces on pipelines are:

- To examine the performance of different turbulence models on predicting the induced hydrodynamic forces on pipelines due to tsunami-like bores using numerical modelling.
- To investigate the physical mechanism of the flow behaviour for different pipe geometry and placement on the induced forces. Results for pipes with different gap ratios are analyzed against the prediction of both vortex shedding and wake characteristics.
- To investigate the effect of varying the pipe diameter and bed roughness on the induced hydrodynamic forces.

5.2. Experimental study

A comprehensive experimental program was conducted in the Dam-Break Flume in the Hydraulics Laboratory at the University of Ottawa, Canada. The flume is 30.1 m in length, 1.5 m in width,

0.5 m in depth. Various hydrodynamic parameters (time-history of the water surface, bore front and sustained flow velocity), as well as the time-history of the forces exerted on the physical model of the horizontal pipeline (0.1 m in diameter and 1.47 m in width across the flume), were measured during the tests. The instrumentation includes Wave gauges (WG) were used to measure the time-history of the water surface elevation, Acoustic Doppler Velocimeter (ADV) measured the time-history of the flow velocity and a six (6) degrees of freedom dynamometer measured the time-history of the induced forces onto the pipe. Figure 5.1 illustrates the schematic view of the dam-break flume and location of instruments as well as the experimental characteristics, while Figure 5.2 shows pictures of the experimental setup and instrumentation. Table 5.1 presents a summary of the instruments used in this set of experiments together with their specifications.

Table 5.1. Instruments used in the experimental program

Instrument	Manufacturer, Model	Sampling rate	Accuracy
Wave gauge (WG)	RBR WG-50, capacitance-type	300 Hz	±0.002 m
Acoustic Doppler Velocimeter (ADV)	Nortek, Vectrino	200 Hz	± 1 mm/s
Dynamometer	Interface- 6A68E	300 Hz	± 0.04%

The experiment was conducted to test the influence of different parameters: reservoir depth (h), still water depth (d) and the ratio of the lower edge of pipe distance to bed (e) to diameter (e/D) on the forces exerted onto the pipe. The tests were performed in the absence of the pipe to study the free stream flow hydrodynamics as well as with the pipe installed in order to study the bore-structure interaction and to measure and analyze forces exerted on the pipe from the impacting bore.

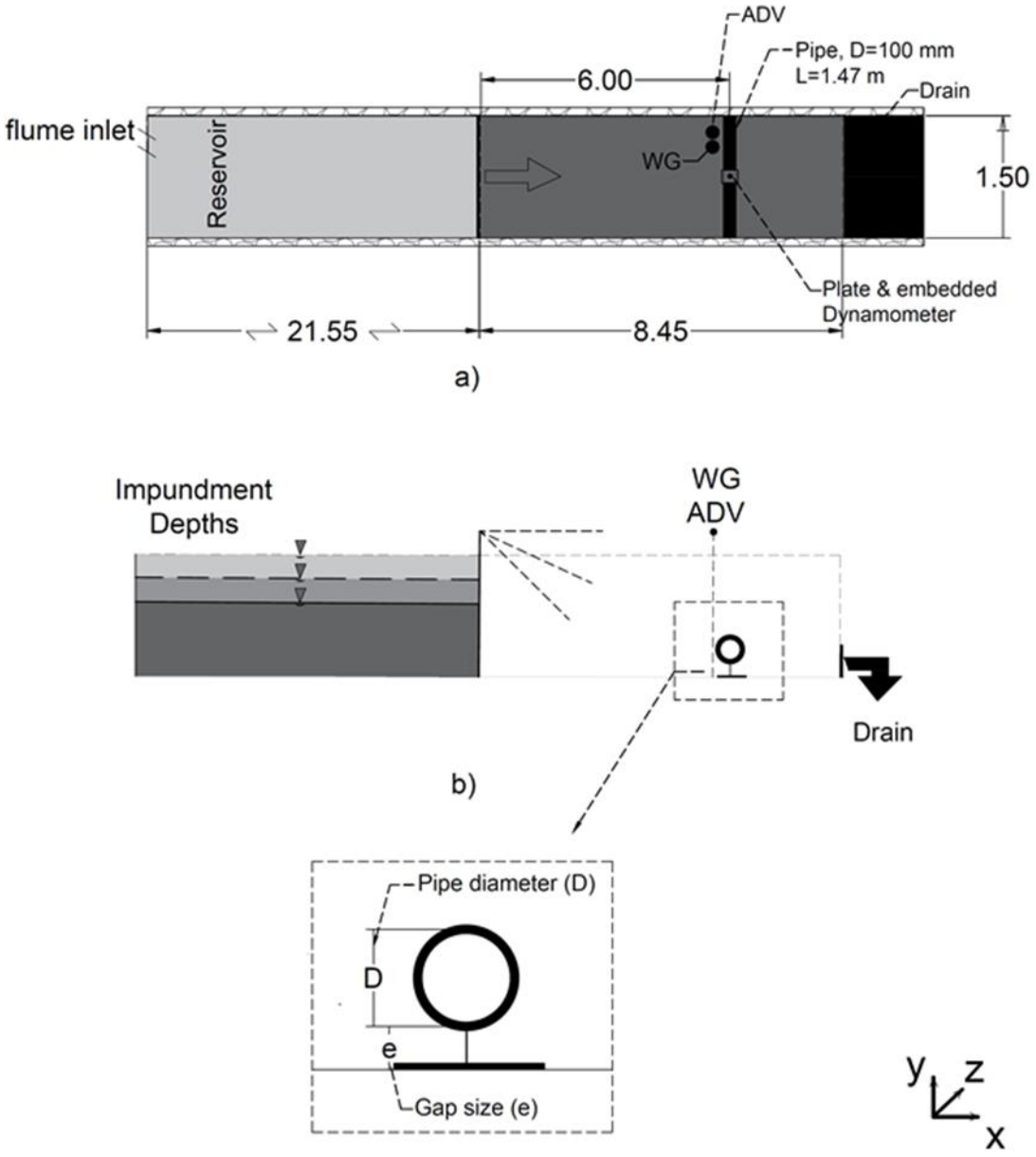

Figure 5.1. Flume and location of the model and instrumentation, (unless otherwise specified, all dimensions are in m; not at scale). a) Plan view, b) Side view, c) Close pipe side view, pipe and experimental parameters.

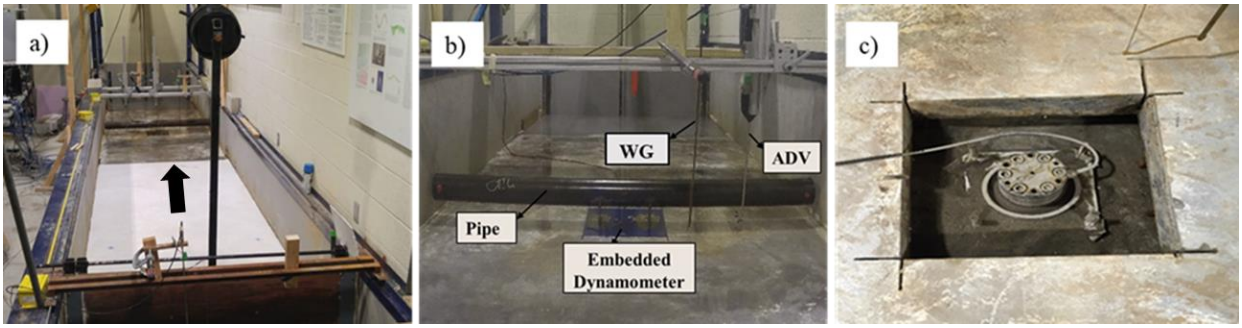

Figure 5.2. (a) Side view from the flume and swing gate (b) ADV, wave gauge and pipe (c) Embedded dynamometer

Several test parameters, including the time histories of the water surface and velocity as well as the induced hydrodynamic forces, were used for the validation of the numerical model and to compare the experimental and numerical results. The next section presents a summary of the results of the experimental study.

5.2.1. Drag force

Results from experimental tests using different pipe distance to bed (*e*) to diameter (D) ratio *e/D* values in dry bed conditions are presented in this section. For clarity, all results are shown starting 1.0 seconds prior to the initial dam-break wave arrival time. The force magnitude was set to zero shortly before the start of each test to eliminate the effect of the latent hydrostatic forces as well as that of the pipe's own weight. Figure 5.3 shows the results from a test conducted with a wave generated by an impoundment depth h = 0.40 m in dry bed condition downstream of the gate.

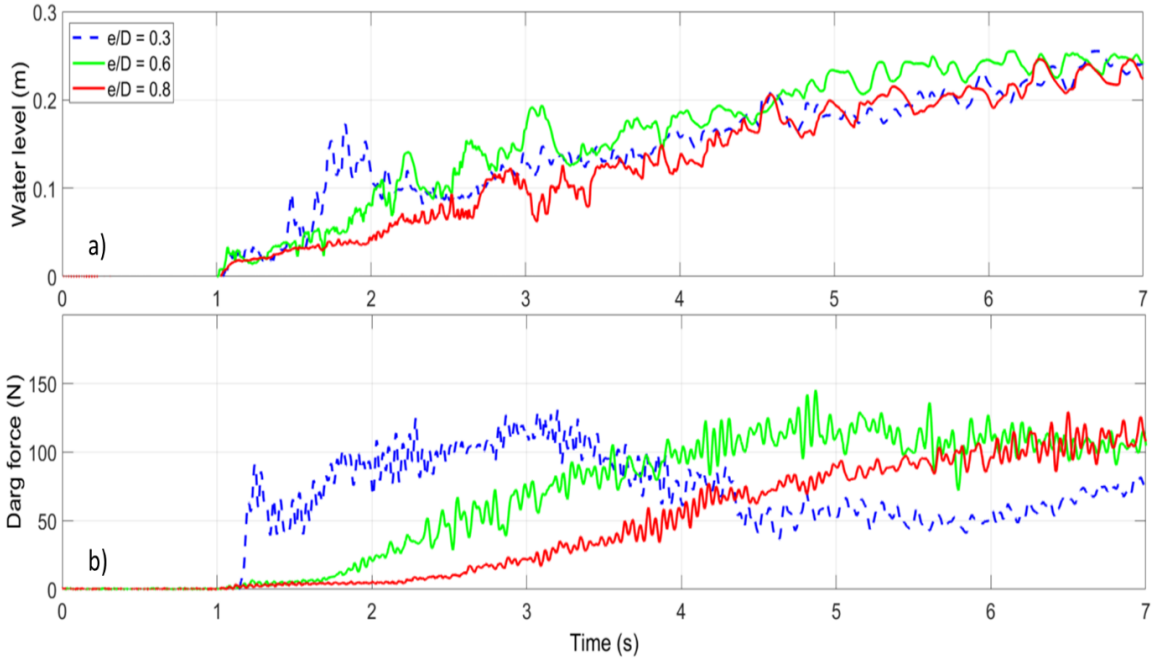

Figure 5.3. Time-history of the water level and of the drag and lift force component measurements for dry bed condition, and impoundment depth, h = 0.40 m. a) Water level for *e/D* = 0.8, 0.6, 0.3. b) Drag force time-history for *e/D* = 0.3, 0.6, 0.8

Figure 5.3a shows the time-history of the water surface recorded by WG3 for the case with a gap ratio *e/D* = 0.3, 0.6 and 0.8. Figure 5.3a shows that the water level for *e/D* = 0.3 increased immediately after the initial wave impact time and that it gradually increased for cases with larger gap ratios, i.e. *e/D* = 0.6 and *e/D* = 0.8. Figure 5.3b shows the measured drag force time-history for the three gap ratios. Figure 5.3b shows that only for the case of *e/D* = 0.3, an impulse force at the wave impact time was recorded whereas no impulse force was observed of the other two gap ratios e/D. In the case of the larger gap ratios, water passed through the gap for the first few seconds of the wave propagation, whereas in the case of *e/D* = 0.3, less water passed through the gap and, instead, the incoming wave impacting the pipe caused a sudden rise in the water level and generated a noticeable impulse force for *e/D* = 0.3 (Figure 5.3a&b). Higher water levels and larger drag forces observed in the case of *e/D* = 0.6 compared to the case with *e/D* = 0.8 can be also explained through the fact that less water passed through the gap between the pipe and the flume bed, resulting in a shorter rise time in smaller gap ratios. For the test with *e/D* = 0.3, as the water level reached the top of the pipe, a surface roller formed right upstream of the pipe and started propagating upstream, causing a considerable decrease in the drag force. For the case of the other two gap ratios of *e/D = 0.6* and 0.8, the observed surface roller was much smaller in size and its upstream propagation speed was considerably slower. Therefore, only in the test with *e/D = 0.3*, a sudden decrease in the drag force was observed.

A detailed presentation of the experimental study and the discussion about the obtained results from testing different parameters are available in Ghodoosipour et al. 2019a and b.

5.3. Numerical study

To solve the three-dimensional Navier-Stokes equations (NSE), an OpenFOAM (Open Field Operation and Manipulation) model was developed which included a solver called interFoam for incompressible two-phase flow. The Finite Volume Method (FVM) is implemented in OpenFOAM to discretize the governing equations. The interFoam solver tracks the water surface elevation using the Volume of Fluid (VOF) method.

In this study, the fluid movement is modeled by Navier Stokes Equations (NSEs). These equations describe the conservation of mass and momentum. The fluid is considered as incompressible. Pressure and velocity fields are linked in these equations and should be solved simultaneously. The three-dimensional continuity and momentum equations are expressed as (Rusche 2002):

Continuity equation:

$$\nabla . U = 0 \qquad \text{(Eq. 5.1)}$$

Momentum equations:

$$\frac{\partial \rho U}{\partial t} + \nabla . (\rho U U) = -\nabla P + \nabla . \tau + \rho g + S \qquad \text{(Eq. 5.2)}$$

where ρ is the fluid density, U is flow velocity vector, τ is the viscosity stress tensor and P is the pressure and S is the momentum source term due to surface tension.
A value of 0.5 was assigned as the maximum Courant number and the initial time step was set to be 0.05 s, although the latter was automatically adjusted during the simulation according to the maximum Courant number. Additional simulations were performed with different values for the initial time step and maximum Courant number and the results were found to be almost identical to the current results.

5.3.1. Turbulence models

A brief discussion of the turbulence models tested in this study is provided in the subsequent sub-sections.

5.3.1.1. Time-averaged models

Navier-Stokes equations are complex and time consuming to be solved using DNS (Direct Numerical Simulation). Therefore, approximations are needed to create a computationally-efficient and accurate model. The most used approximation is Reynolds Average Navier Stokes (RANS) method. Reynolds stresses are the stresses that appear during the averaging process and act on the volume of water. After the time averaging and obtaining the RANS approximation, there are still more unknowns than the number of equations. Turbulence closure models are used to solve the unknowns in the RANS. The models tested in this study are discussed in this section.

- ***k-ε (Standard)***

The most commonly used RANS closure model is the *k-ε* model, where *k* is the turbulent kinetic energy and *ε* is the rate of dissipation of the turbulent kinetic energy. The model closes the RANS by proposing equations to solve the shear stresses (u^2, v^2, w^2, $\overline{u'u'}$, $\overline{u'v'}$, $\overline{u'w'}$). The first step is to define the Boussinesq eddy viscosity (ν_T) term. This viscosity analogizes energy losses due to turbulence in the flow by increasing the fluid's viscosity. This model was developed for fully turbulent flows and employs two main assumptions; (1) the fluid and its Reynold stresses are isotropic and (2) the turbulence is only related to the local flow speed. These assumptions reduce the extent of the model's accuracy. For instance, the isotropic assumption may be erroneous close to walls, where the wall proximity changes fluid properties under some circumstances. Also, this removes the possibility to model accurately non-Newtonian fluids, which are anisotropic. The second assumption limits the model when it comes to highly mixing fluids. In those cases, heavy turbulence from surrounding eddies will most likely affect local turbulence.

- ***k-ε (RNG)***

A newer version of k-ε was derived from the instantaneous Navier-Stokes equations using Renormalization Group (RNG) method (Yakhot & Orszag 1986). RNG *k-ε*, is different from the standard *k-ε* in some parameters and constants in turbulent dissipation rate (ε). These changes in *ε* equation allow for a more accurate description of how the effective Reynolds number (or eddy scale) influences the effective turbulent transport. This results in better model performance at low-Reynolds number and for near-wall flows. In RNG *k-ε* model the swirling effect is included using a swirl modification factor in eddy viscosity equation. Turbulence viscosity in rapidly strain flow is lower in the RNG *k-ε* model than standard *k-ε* one which makes it more precise for simulating streamline curvature and rapidly strained flows. Generally, RNG *k-ε* shows improvement in predicting fluid rotation, boundary layers under strong adverse pressure gradient, flow separation, low Reynolds flows, and near-wall flows compared to the standard *k-ε* model. Also, improvements in *ε* equation result in lower turbulence levels and therefore, the model performs better in predicting complex features such as strong streamline curvature and vortices.

- ***k-ε (Realizable)***

The realizable *k-ε* model is an updated version of the standard *k-ε* model. The model aims to improve the standard *k-ε* model in predicting the spreading rate for axisymmetric and planar jets. *ε* equation was changed in a way that the normal stresses are always positive which makes the equation always "realizable".

5.3.1.2. Spatially averaged models

- ***Large Eddy Simulations (LES)***

The most commonly used spatially averaged model is Large Eddy Simulation (LES) model. The model approximates the Navier-Stokes equation by filtering the small-scale (smaller than grid cell) eddies. The model divides the eddies into two groups: large eddies and small eddies. The main assumption of this model is that the large eddies (that is, those larger than grid cell) are the most influential eddies which carry more energy and can affect flow behaviour. Therefore, this model neglects the presence of the small eddies, an assumption which decreases model accuracy in cases where the small-scale turbulence plays an important role such as flow in near-wall regions and in cases when multiple flows are interacting.

- ***Detached Eddy Simulations (DES)***

In order to overcome the deficiency of the LES model in near wall regions, the Detached Eddy Simulation DES model was developed (Spalart et al. 1997). DES is a mix of LES and RANS models and uses the hybrid technic to change between LES when turbulent length scale is larger

than grid size and RANS when the turbulent length is smaller than the grid size. (Spalart, 2008). This approach reduces the near wall's modelling computational time compared to the LES model. This model exhibits high grid sensitivity and is especially successful in high Reynolds number flows. DES uses the LES in thick boundary layer and shallow separation regions which results in less energy dissipation and deficiency in model predictions in such cases.

- ***Delayed Differential Eddy Simulation (DDES)***

DDES model is a more recent version of the DES model developed by Spalart et al. 2006. In this model, LES is used only when the turbulence length is greater than the grid scale and RANS is used at the boundary layer. This approach addresses some of the deficiencies in DES model such as premature switch between LES and RANS models and ensures a certain level of superiority to DES especially in near-wall regions (Spalart, 2008).Similar to DES, DDES demonstrated strong performance in high Reynolds flows. However, DDES is less sensitive to grid size and grid induced separation.

5.3.2. Flow and mesh configuration

In this study, an unstructured mesh was generated using the SALOME software (Ribes et al. 2017). To ensure that the model is mesh size independent, a sensitivity analysis was performed to select the appropriate grid for the model. This analysis was performed by running several simulations, using standard k-ε turbulence model, with different grid sizes and finding a threshold whereby its results were mesh-independent. The grid refinement criterion was set to reach a difference of less than 2% between the predicted results when using the last two grids. In all cases, results from the uniform mesh showed inconsistencies with the experimental data at and near the time of the initial bore impact. Therefore, to improve model performance, the mesh was divided into three regions: the Far-field region, the Near-field region and the Around-pipe region. The boundary of the Far-field region was set one meter upstream and downstream of the pipe while the Near-field region was set within one meter on each side of the pipe. Using mesh sensitivity analysis, best results were achieved using a 0.02 m grid size for the Far-field region, 0.005 m grid at Near-Field region and 0.0025 m grid size for the Around-pipe region. Figure 5.4 illustrates the generated mesh and the assigned regions.

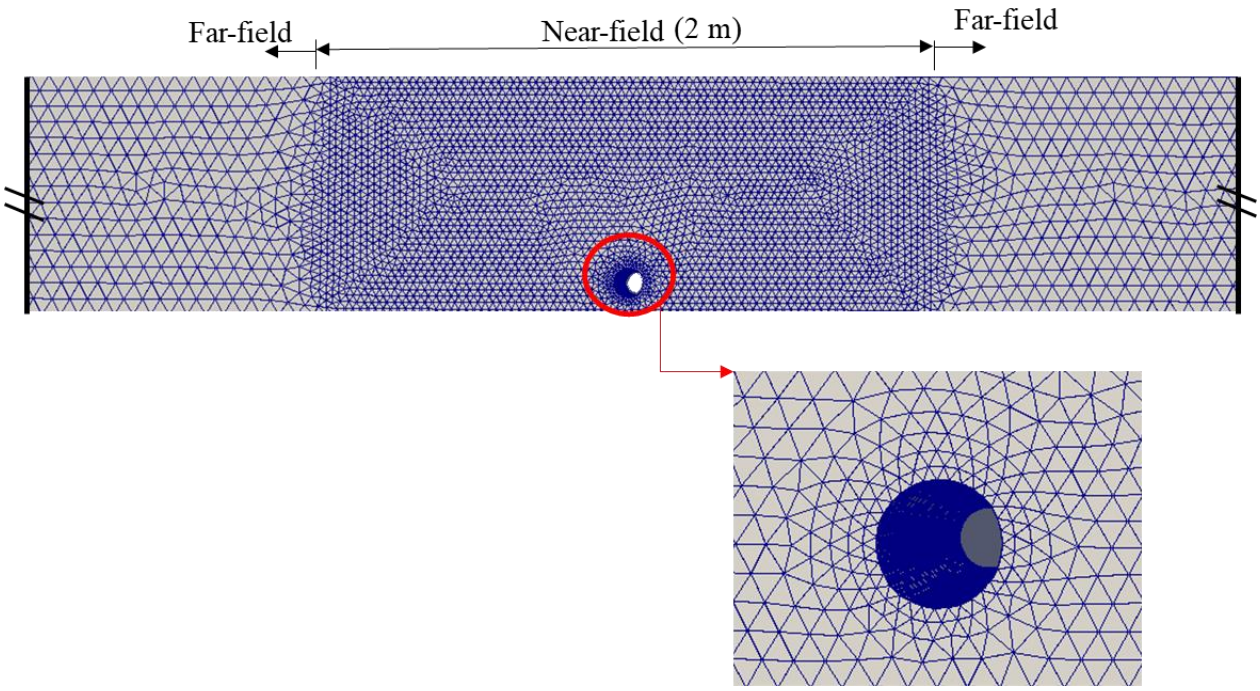

Figure 5.4. Unstructured mesh and refinement regions.

The boundary condition at the sidewalls and flume bed surface were set as *wall boundary* condition with zero surface roughness. The inlet-outlet boundary condition was used for the atmosphere, which works the same way as zeroGradient in forward flow and changes to the fixed-value boundary condition if there is any backward flow. This helps disregard the need to investigate whether the boundary condition is of Neumann or Dirichlet type (Yan and Mohammadian 2017).

5.3.3. Model validation

The validation of the developed numerical model was performed by comparing its results with those collected by the authors from their experimental study (presented in Section 5.2).

5.4. Results and discussion

5.4.1. Influence of turbulence models

To develop a numerical model which would be capable of accurately simulating the experimental data, various turbulence models were tested: Reynolds averaged Navier-Stokes models, RANS (k-ε, k-w, RNG k-ε and LRR), large eddy simulation (LES) models as well as the Detached Eddy Simulation DES (DES, DDES) were tested. Figure 5.5 shows a comparison between experimental results and numerical model results for different turbulence models. The comparison shown is for the drag force measured and computed in dry bed condition with an initial impoundment water depth of 0.5 m. The results shown in Figure 5.5 revealed that all of the tested models were capable of reasonably predicting the overall force trend. However, the forces obtained using the LES model

were noticeably lower than the experimental data, implying that this model underestimated significantly the magnitude of the drag force.

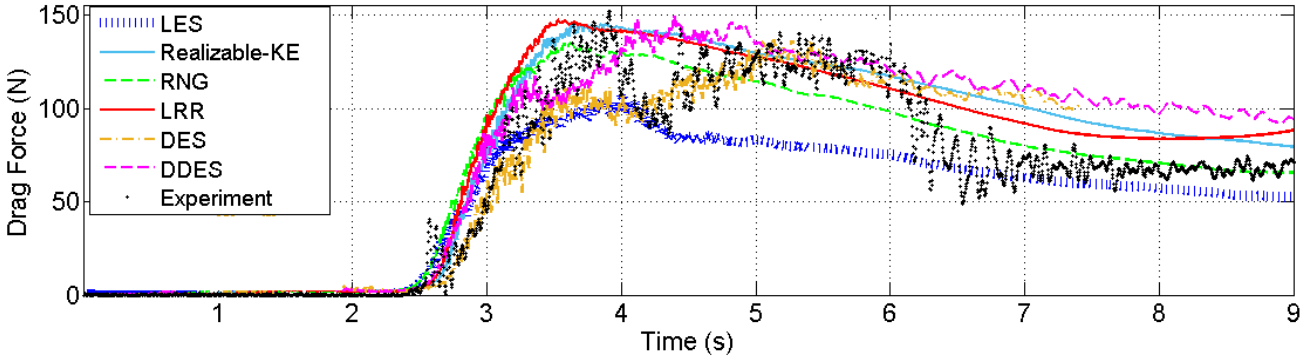

Figure 5.5. Time-history of the drag force – comparison of the turbulence models for an impoundment depth, h=0.50 m, and gap ration, e/D=0.6.

To obtain a quantitative measure of the differences between the experimental data and model results, different statistical errors between numerical and experimental results were calculated as shown below.

The mean absolute percentage error (MAPE) was calculated as:

$$MAPE = \frac{1}{n}\sum_{i=1}^{n}\frac{|EXP_i - NUM_i|}{|EXP_i|} \qquad \text{(Eq. 5.3)}$$

where *EXP* is the experimental data, *NUM* is the numerical data and *n* is the total number of data.

Due to the practical importance of predicting the peak forces for pipeline design, the prediction accuracy of the peak events is of particular interest in this study. Thus, another statistical measure, the Peak Value Criteria (PVC), (Coulibaly et al.,2001 and El-Shafie et al. 2009), was also employed to evaluate the model performance at the extreme values and was calculated using;

$$PVC = \frac{\left(\sum_{i=1}^{n_p}(EXP_{pi} - NUM_{pi})^2 \times (EXP_{pi})^2\right)^{0.25}}{\left(\sum_{i=1}^{n} {EXP_{pi}}^2\right)^{0.5}} \qquad \text{(Eq. 5.4)}$$

where n_p is number of forces peaks greater than one-third of the mean force observed, EXP_p and NUM_p are the peak force values from the experimental and numerical model, respectively. Coulibaly et al. 2001, concluded that PVC is an adequate indicator for assessment of the prediction model performance for the extreme events compared to RMSE. To reduce the effect of the noise in the experimental data, an error was also calculated using the first mode of the experimental data, derived by using Dynamic Mode Decomposition (DMD) method as proposed by Schmid and

Sesterhenn 2008. DMD is a dimensionality reduction algorithm which computes a set of modes associated with a fixed oscillation frequency and decay/growth rate. The DMD algorithm was applied to the experimental data and the error was calculated using Eq. 5.3.

Additionally, the *R*-squared values (R^2) was calculated using the linear correlation between actual and simulated data.

Table 5.2, summarizes the calculated errors explained above for different turbulence models.

Table 5.2. Comparison of the performance of various turbulence models

Turbulence model	R2	MAPE	PVC	DMD
RKE	0.77	21.8%	0.43	23.2%
RNG	0.8	13.4%	0.34	12%
LRR	0.8	23.95%	0.43	23.4%
DES	0.75	23.78%	0.39	21%
DDES	0.76	23.8%	0.38	20.9%
LES	0.5	24.2%	0.58	23.2%

As shown in Table 5.2, the RNG k-ε turbulence model, with smallest calculated error suite (MAPE, PVC and DMD), exhibited the best performance among other models. RNG model also returned the largest R^2 value. Figure 5.6 shows the correlation and calculated R^2 for the best fitted turbulence model (RNG k-ε).

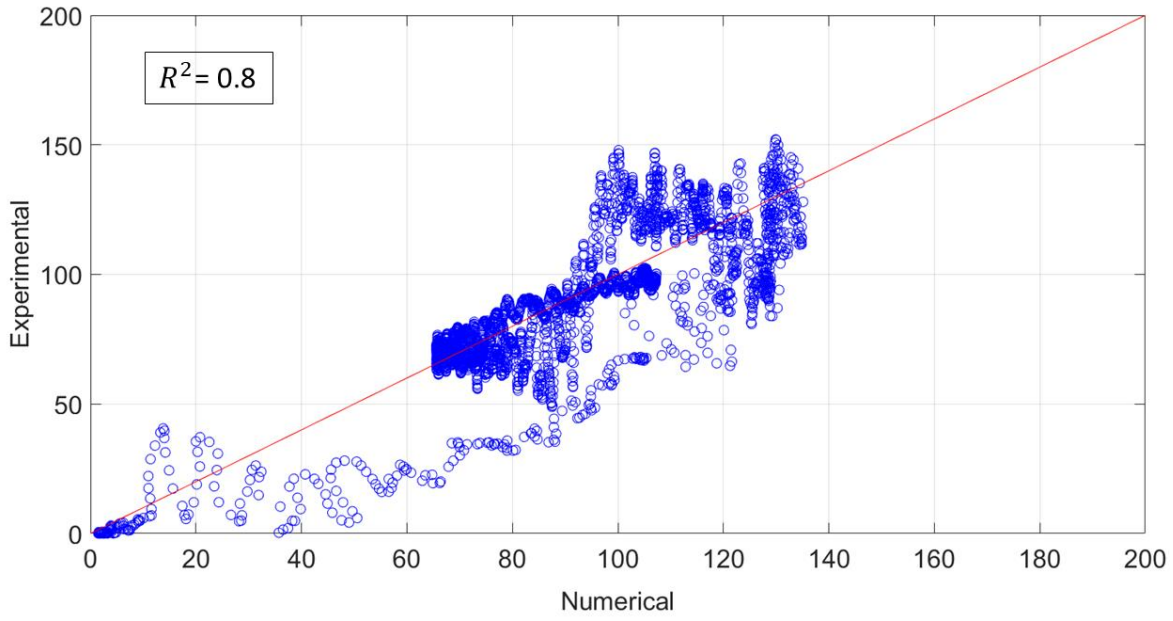

Figure 5.6. Correlation between experimental and numerical model prediction for force time-history using the RNG turbulence model.

The LES model has the advantage of not resolving the smallest length scales, which are computationally expensive to resolve, by using a low-pass filtering of the Navier–Stokes equations. Such low-pass filtering, which can be viewed as spatial averaging, effectively removes small-scale flow information from the numerical solution. According to Zhiyin 2015, for an accurate LES simulation, mesh resolution needs to be fine enough to resolve the smallest dynamically significant length-scale (the Kolmogorov micro-scale). Such mesh refinement increases the computational cost significantly. Large difference between the experimental results and the numerical model predictions using LES turbulence model in figure 5.5, shows that the mesh resolution used in this modeling approach was not sufficiently fine for the LES model to be implemented. Therefore, elimination of the small-scale flow reduced the model accuracy and led to an under-estimation in predicted forces exerted on the pipeline.

The difficulties associated with the use of the standard LES models, particularly in the near-wall regions, has led to the development of hybrid models that attempt to combine the best features of RANS and LES models into a single solution strategy. Examples of hybrid techniques are the detached-eddy simulation (DES) presented by Spalart et al. 1997 and the delayed detached-eddy simulation (DDES) approach by Spalart et al. 2006. As explained before, these models attempt to treat near-wall regions the same way as RANS models and treat the rest of the flow the same way as LES models.

The performance of DES (Spalart-allmaras-DES) and DDES (Spalart-allmaras-DDES) models which are based on the Spalart–Allmaras one-equation model (S–A model by Spalart and Allmaras 1992) showed improvement compared to the LES model. In this study, the standard k-ε model was used as the RANS component of these hybrid models. DES and DDES models showed similar performance as shown in Table 5.2 with their associated errors in close range.

The RNG *k*-*ε* turbulence model differs from the standard *k*-*ε* when calculating the turbulent viscosity, the turbulent Prandtl numbers, and the *ε* equation. The calculation of the turbulent viscosity in the RNG *k*-*ε* turbulence model is performed using the scale elimination procedure in RNG theory, which can precisely describe the impact of the effective Reynolds number on the effective turbulent transport. More importantly, the RNG *k*-*ε* model introduces an additional term in the *ε* equation, which can improve the calculation of the turbulent viscosity, especially in regions of large strain rate (Fluent, 2015). Therefore, the RNG *k*-*ε* model has a superior performance in near-wall flows such as the present case. The RNG *k*-*ε* turbulence model was used further to carry out additional simulations to assess how varying parameters affect the calculated hydrodynamic forces exerted on the horizontal pipeline.

5.4.2. The influence of the distance between the pipe and the bed, gap ratio (e/D)

Figure 5.7, shows the effect of gap ratio on the drag force time-history and the comparison between experimental and numerical results for a dry bed case and an impoundment depth of 0.5 m.

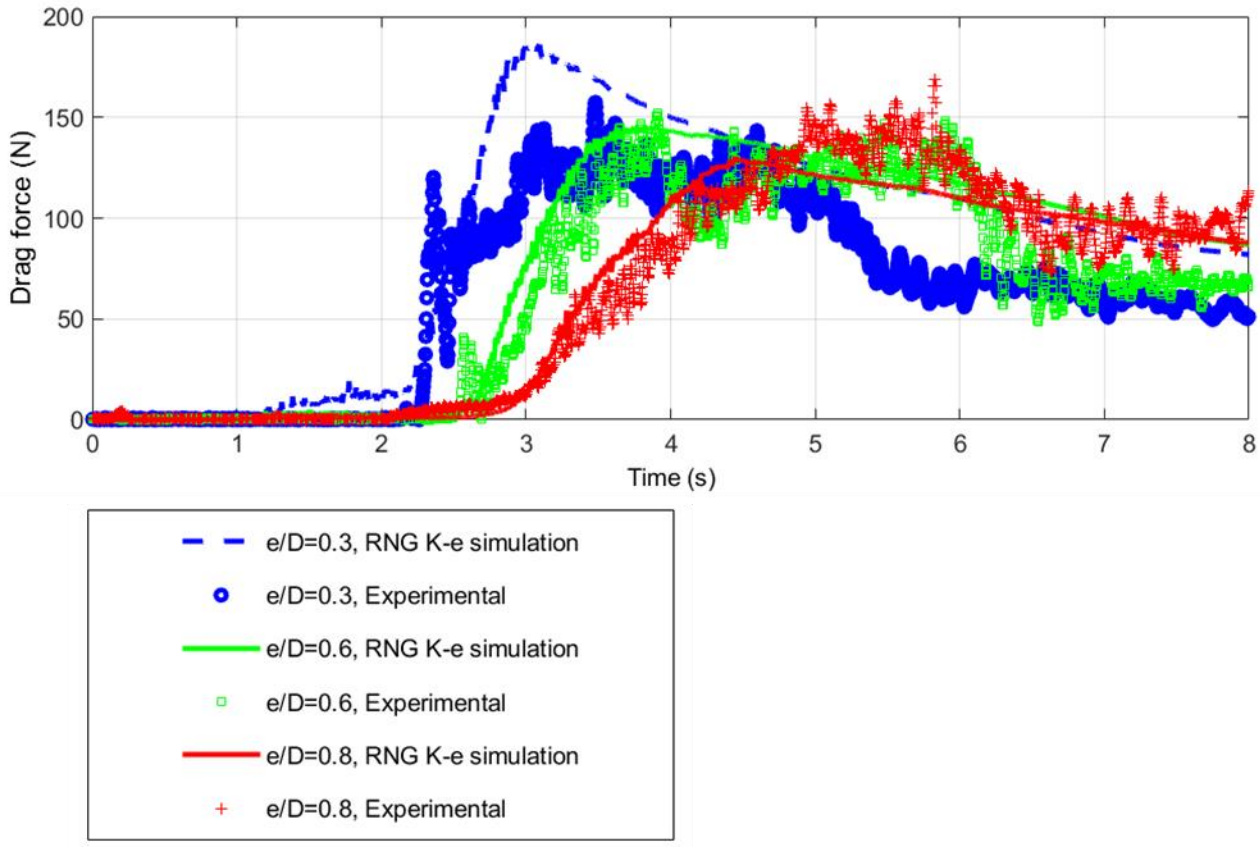

Figure 5.7. Numerical and experimental result comparison. Drag force time history. Different e/D ratios. Blue: e/D=0.3, Green: e/D=0.6, e/D=0.8. Bore generated by an impoundment depth of 0.50 m.

In the numerical models, the flume bed and the pipe were considered to be hydraulically smooth. Figure 5.7 shows that the numerical model is better at predicting the drag force for larger gap ratios and less accurate at predicting impulse forces at the time of the initial bore impact. Experimental results show that the impulse force is more pronounced for smaller gap ratios due to sudden bore blockage upstream of pipe at smaller gap ratios whereas, more water passes through the gap in the case of larger gap ratios. Hence, for this particular case, the numerical model is more successful in the case of larger gap ratios. Figure 5.8, illustrates the sequence of bore surging around the pipe for the three gap ratio values, e/D=0.3, 0.6 and 0.8.

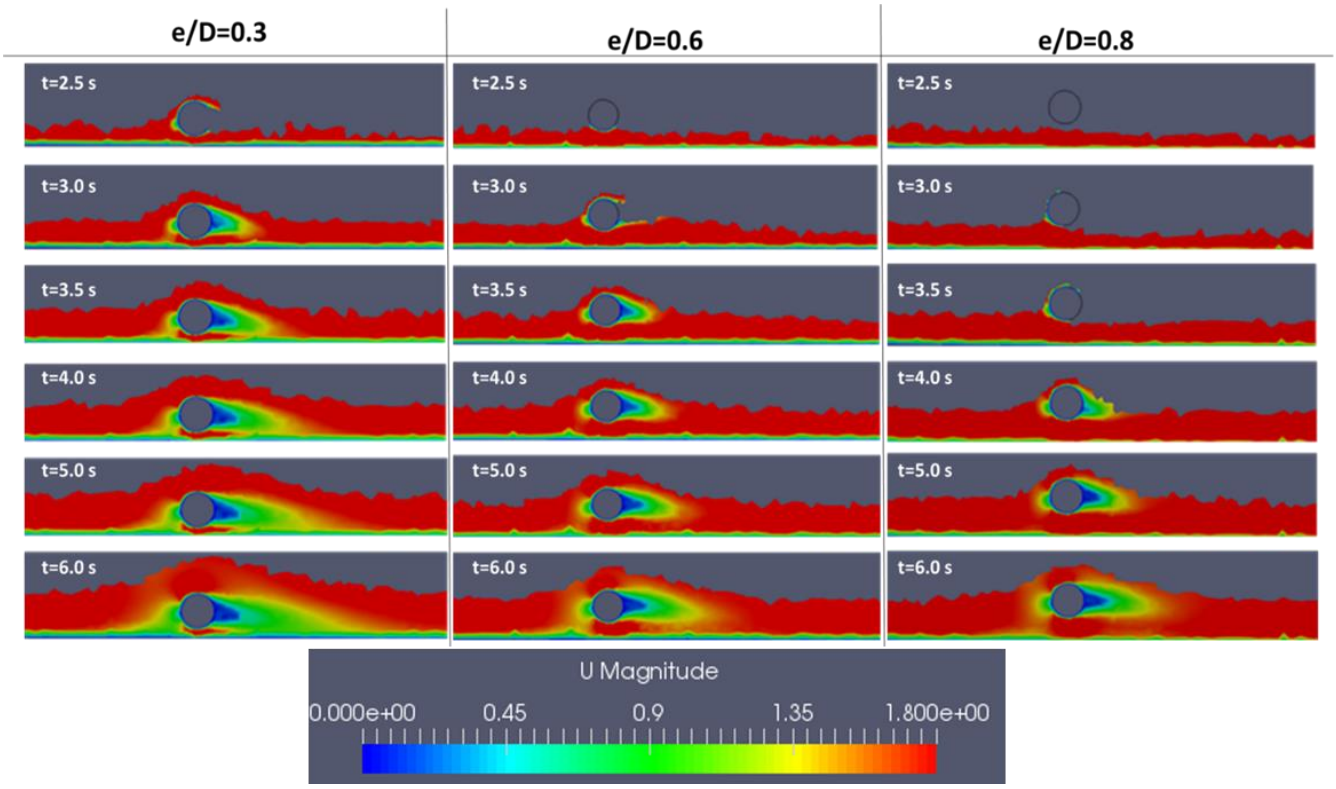

Figure 5.8. Time-history of the velocity field contours during the bore surge. e/D = 0.3, 0.6, 0.8. Vortex shedding suppression occurs faster in the case of smaller e/D=0.3. Bore generated by an impoundment depth of 0.50 m.

Figure 5.8 shows the bore rapidly surging on top of the pipe with e/D=0.3 in a relatively short duration of time (t=2.5 s) after the bore impact which causes a large impulse force. At the same instant (t=2.5 s) most of the water mostly passed through the gap space for the case when e/D=0.6 and e/D=0.8. A steeper increase in drag force in the case of smaller e/D can be also explained by the larger duration it takes the water to impact the entire exposed pipe cross section. Figure 5.8 also shows that vortex shedding is suppressed faster in the case of smaller e/D ratios as shown by fading visible vortices for e/D=0.3 and noticeable vortex shedding downstream of the pipe in the case of e/D=0.6 and e/D=0.8 as time passes. The changes in the location of the stagnation point and the angular position of separation points by moving the pipe close to the bed cause lager suction on the free-stream side of the cylinder than on the wall-side. This phenomenon causes vortex shedding suppression to occur faster in the case of the smaller gap ratio.

5.4.3. Influence of the pipe diameter

Figure 5.9. illustrates the comparison between dam-break wave induced force for different pipe diameters. Results for the Gap ratio value e/D=0.6 is discussed below.

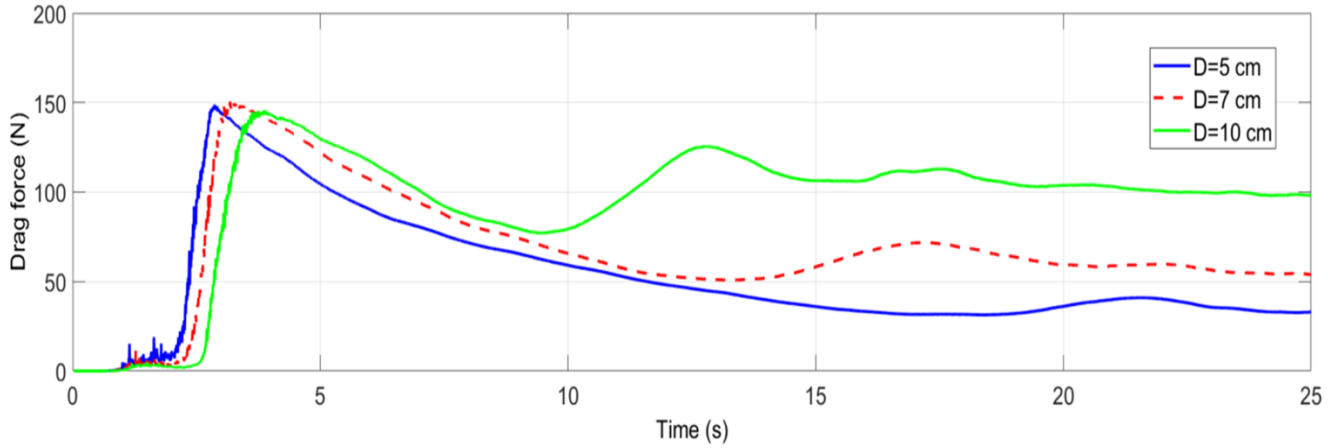

Figure 5.9. Predicted drag force time history. Different pipe diameters: D=0.10 m , 0.70 m, 0.50 m. bore generated by an impoundment depth of 0.50 m.

Figure 5.9, illustrates that impulse force has almost the same magnitude in all cases while after the initial impact and as the pipe becomes fully submerged, the drag force magnitude is larger for the cases with larger pipe diameter. As mentioned, Figure 5.9 shows the force time-history of the drag forces for the three pipe diameter values and one can notice that the peak force is almost equal in all three cases. However, later in the time-history, drag force magnitude is larger for the pipes with a larger diameter. In all three cases after some time (10-20 seconds), the flow becomes nearly critical due to the pipe blocking the flow which results in increase in the water depth. After this point, the presence of the pipe results in large standing wave and an increase in induced drag force. Figure 5.10, shows the sequence of the bore surge for three tested pipe diameters, i.e 0.10 m , 0.07 m, 0.05 m. As shown in Figure 5.10, the critical depth and the resulting standing wave occurs faster in larger pipe diameters compared to smaller pipe diameters. The waves start to travel upstream as the flow regime changes to subcritical flow which causes the drag force to decrease.

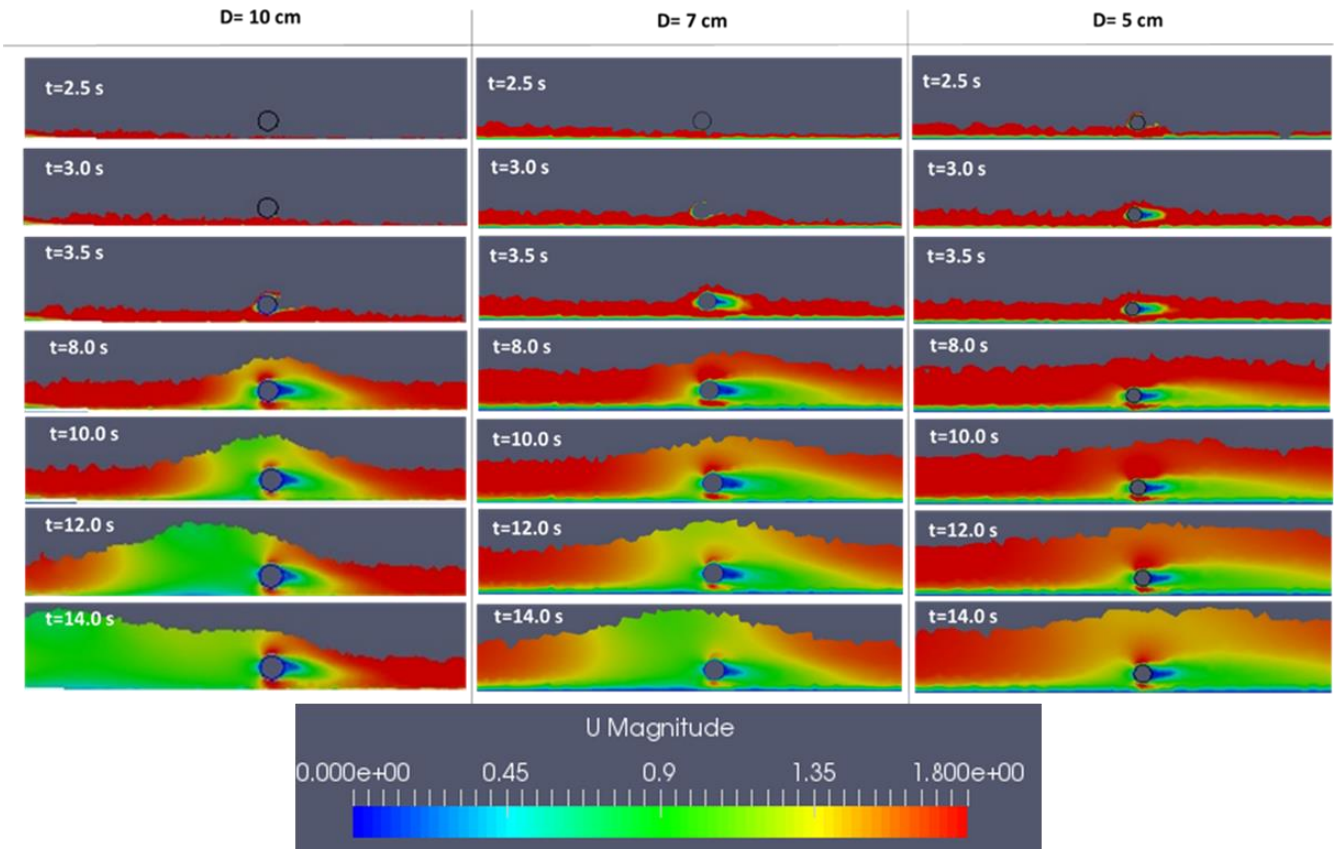

Figure 5.10. Time-history of the velocity field contours during the bore surge for three pipe diameters; bore generated by an impoundment depth of 0.50 m.

5.4.4. Influence of the bed roughness

Sensitivity analysis was performed to investigate the effect of the bed roughness on predicted time-history of the drag force.

In the numerical model, the roughness coefficient E is estimated as (Khosronejad et al. 2011):

$$E = \begin{cases} 9.8 & \text{if } k_s^+ \le 2.25 \\ \dfrac{9.8}{\left(\dfrac{k_s^+ - 2.25}{87.75} + C_s k_s^+\right)^{\sin\left(0.4258 \ln k_s^+ - 0.811\right)}} & \text{if } 2.25 < k_s^+ < 90 \\ \dfrac{E}{1 + C_s k_s^+} & \text{if } k_s^+ \ge 90 \end{cases} \qquad \text{(Eq. 5.4)}$$

where C_s is the roughness constant with a default value of 0.5 and k_s^+ is the dimensionless grain height defined as

$$k_s^+ = \frac{u_\tau k_s}{\nu} \qquad \text{(Eq. 5.6)}$$

where k_s is the grain roughness height, which can be usually estimated based on the sediment diameter.

Figure 5.11 shows the results for drag force with different bed roughness. Roughness height and roughness constant were set to 0.002 m and 0.7 respectively, in the rough model. Roughness height was increased to 0.003 m in the rougher model. Results from a model with increased roughness were compared against a model with no bed roughness. Results show that adding bed and pipe roughness decreased the force magnitude by approximately 10%. Flow speed on a rough bed is smaller compared to the flow on smooth bed, which causes the induced forces on the pipe, which is placed near the bed, to decrease. Increasing the roughness height from 0.002 m to 0.003 m did not change the force magnitude.

In another case of tested rough bed and smooth pipe, results from this model were almost identical to the previous simulation with equal roughness for pipe and the bed, showing that the pipe roughness does not significantly affect the drag force magnitude. Pipe roughness does not seem to influence the surrounding flow velocity and the induced drag force does not seem to be sensitive to the pipe roughness and this is due to the fact that the flow in a fully turbulent regime.

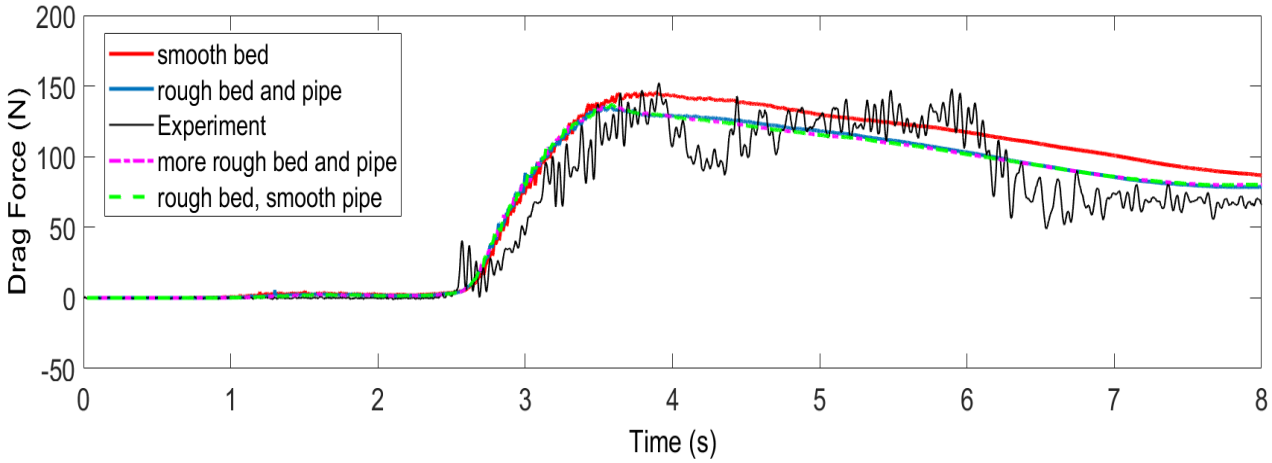

Figure 5.11. Roughness effect on induced force on pipe.

5.5. Conclusions

This paper presents the results of a combined experimental and numerical study on the impact of tsunami-like bores on horizontal pipelines. The numerical model was validated using data from a comprehensive experimental study conducted by the authors in the Hydraulic Laboratory at the University of Ottawa, Canada. Different parameters affecting the induced forces on the pipeline were investigated. The following conclusions were drawn from this research:

- The performance of several turbulence models' was tested and assessed. The RNG k-ε model proved to be most accurate among the RANS models in predicting the time history of the induced drag force exerted on the pipe. The addition of new terms to the ε equation in RNG k-ε model improves the calculation of the turbulent viscosity, especially in the near-wall regions, which leads to a superior performance. LES model exhibited the weakest performance due to the mesh around the pipe being too coarse, resulting in filtering of the small scale turbulence, which plays an important role in the flow around circular cylinders. Performance of hybrid models such as the DES and the DDES models which combine the RANS and LES models showed improvement compared to the LES model.
- Results from testing the model for different pipe gap ratio (e/D) demonstrated that the developed CFD numerical model is less accurate in predicting the impulse force at the time of bore impact. The model exhibited better performance for cases with larger e/D ratio. The model was successful in predicting vortex shedding suppression accelerating in cases with smaller gap ratio.
- The effect of the pipe diameter on the bore-induced drag force was investigated. It was demonstrated that the pipe diameter has little effect on the magnitude of the impulse force for the range of values tested in this study. After the initial impact, the drag force magnitude increased with an increased pipe diameter. In all three cases, after some time, the flow blockage caused by the presence of the pipe and the resulting increase in water depth, caused the flow to become nearly critical. At this point, large standing wave was formed and the induced drag force increased. This happened faster in the case of larger pipe diameters compared to the smaller diameters.
- The induced drag force decreases with an increase in the bed roughness due to decreased flow velocity compared to that calculated to the smooth bed. However, pipe roughness did not affect the magnitude of the induced drag force.

6. Summary and concluding remarks

A series of experimental and numerical research work was conducted to study loading on horizontal pipelines located in coastal areas induced by tsunami-like transient flow. Drag and lift forces exerted on pipelines were measured in different flow conditions and different pipe configurations. Based on the analysis of the collected experimental data, this study aimed to recommend force coefficients using different pipe configurations under a wide variety of flow conditions. For the first time, findings from this study will help prescribe new design recommendations for horizontal pipelines located in tsunami and flood-prone areas.

In the first part of this study:

The focus was on the flow hydrodynamics in dry and wet bed conditions and its changing characteristics in the presence of the pipe. In the case of dry bed condition, increasing the impoundment depth proved to increase the bore front velocity and momentum flux as a result of increase in both flow velocity and water depth. In the case of wet bed condition, increasing the initial still water level downstream of the gate led to slower bore flow velocities, reduced Froude number, and reduced momentum flux. The presence of the pipe, for both dry and wet bed condition, caused the water level to rise and the flow velocity to decrease. In dry bed condition, smaller *e/D* values resulted in more abrupt water level rise at the time of the bore impact and a faster decrease in flow velocity. For bore propagating over dry bed, the water level increase at the time of bore impact in the presence of the pipe became larger with an increasing impoundment depth. In the case of the wet bed condition, increased level of pipe submergence *S/D*, due to increasing the still water depth *d* resulted in a reduction of the influence of the pipe on flow hydrodynamics. This was explained by a reduction in the flow blockage, due to the increased pipe submergence.

In the second part of the study:

A comprehensive experimental program was conducted to investigate the mechanisms of the extreme hydrodynamic loading exerted on a pipe due tsunami-like hydraulic bore flows.

Impact of distance of the pipe to bed was investigated in terms of gap ratio (e/D). It was proved that under dry bed condition, the initial horizontal impulse force and the lift force was considerably larger for smaller *e/D*. However, altering the gap ratio (*e/D*) under wet bed condition did not considerably change the force components. Impact of level of pipe submergence on the induced forces was investigated. It was concluded that impulse force decreases by increasing the initial level of submergence (S/D) which results in decreasing the effective contact area of the pipe exposed to surge. This study suggests force coefficient values for various Froude numbers and several pipe configurations through proposed force coefficient versus Froude number graphs. The wide range of suggested force coefficients for various flow and pipe characteristics could be essential and helpful for design purposes. The suggested resistance coefficients are in the range of $1 < C_R < 3.6$ and lift coefficient values in the range of $-2.8 \leq C_L < 2.8$ for the experimental conditions investigated.

In the third part of the study:

The impact of dam-break tsunami-like waves on horizontal pipelines and the parameters affecting the induced forces on pipelines were investigated using CFD numerical modeling and different parameters which could affect the induced forces on pipelines were tested. The numerical model was validated using the data from the experimental study explained in parts one and two. Among all the Reynolds Avergaed Navier-Stokes (RANS) turbulence models tested in this study, RNG k-ε model proved to be more successful in predicting the induced force time history due to the improved ε equation which makes the model more accurate in predicting the turbulent viscosity close to the wall boundary. CFD model showed to be less accurate in predicting the impulse force at the time of bore impact. Therefore, model was more accurate in predicting induced forces on pipelines with larger gap ratios where the impulse force is less significant. Three different pipe diameters were tested using the CFD numerical model. Pipe diameter showed to have little impact on the impulse force magnitude at the time of bore impact in the range of the tested diameters. However, force magnitude showed to increase with increasing pipe diameter later in the time-history and after the bore impact time due to faster flow regime change to critical flow causing the generation of standing waves in cases with larger diameters. Numerical modeling results showed that increasing the bed roughness results in decreasing the induced forces on pipelines while pipe roughness showed not to have a significate impact on the force magnitude.

7. Recommendations for Future Work

The studies presented here examines the extreme hydrodynamic loading on pipelines through a comprehensive experimental testing as well as detailed CFD numerical modeling, However, further work is necessary to accurately capture the hazard at full-scale, the following additions to the body of knowledge would greatly improve the methodology:

- Develop experimental studies for testing the effect of pipe angle in respect to the incoming wave. Such a problem will be a three-dimensional problem and would need sufficiently wide flume to avoid side effects. Numerical model can be employed to test several different pipe configurations.
- Double pipes are commonly used as transition pipelines. Such pipes are installed in different arrangements such as tandem, side-by-side and staggered configurations. Experimental and numerical studies can be conducted to investigate the extreme hydrodynamic loads on such pipeline configurations. Different parameters such as distance between the two pipes can affect flow hydrodynamics around and induced forces on pipes that need to be addressed.
- Flow around pipe placed initially on a flat bed will cause a progressive scour profile and a considerable change in bed geometry. Change in bed geometry due to scour can be significant during extreme events and thus may change flow hydrodynamic around pipelines which in turn can result in altering the induced hydrodynamic forces on pipelines. Investigations of such changes on both flow hydrodynamic and the resulting forces in different scour rates are essential for a proper pipeline design.
- Different bed roughness can also be tested in a set of experiments to investigate roughness effect on changing flow hydrodynamics and the resulting forces on pipelines. Different bed materials such as sand or gravel can be used for this purpose.
- Image analysis technics could be employed in the future experimental studies in order to better understand flow hydrodynamics. Such techniques could be extremely helpful especially for velocity profile measurements where commonly used equipments such as ADV showed to lack accuracy.
- SPH numerical models have proved to be successful in predicting the extreme hydrodynamic loading on different structures. SPH could be tested for the case of extreme hydrodynamic loading on horizontal pipelines.

Appendix A

ASCE 7-16 Change Proposal Form

Proposals to revise the ASCE 7-16 Standards must be submitted using this form. Proposals from outside the Committee/Subcommittees are to be submitted via email to Jon Esslinger, Director, Codes and Standards, at Jesslinger@asce.org

Submitted by: Ioan NISTOR

161 Louis Pasteur, Colonel By Building, CBY-A110, Ottawa, ON, K1N 6N5

Submission date: 8/12/20198/12/20198/12/20198/12/2019

Considered by ASCE 7 Subcommittee on: Ch. 6: Tsunami Loads and EffectsCh. 6: Tsunami Loads and EffectsCh. 6: Tsunami Loads and EffectsCh. 6: Tsunami Loads and Effects

---

FILENAME: TS-CH06-18r00 by Nistor-6.10.2.6- Loads on Above-Ground Horizontal Pipelines

BRIEF DESCRIPTION: A methodology to determine tsunami design forces on above-ground horizontal pipelines

SCOPE: 6.10.2.6 Loads on Above-Ground Horizontal Pipelines

PROPOSAL FOR CHANGE: (Use ~~strike-out~~ and underline format to indicate text to be removed or added, respectively; related modification/proposed addition to Commentary shall be included below.)

6.10.2.6 Loads on Above-Ground Horizontal Pipelines. Above-ground horizontal pipelines necessary for the functionality of Tsunami Risk Category III and IV buildings and other structures shall be designed to resist the loads given in Sections 6.10.2.6.1 and 6.10.2.6.2.

6.10.2.6.1 Hydrodynamic Loads on Above-Ground Horizontal Pipelines

The horizontal force per unit length shall be calculated as

$$F_{rp} = C_{cp} C_r \rho_s I_{tsu} D_p u^2 \tag{6.10-8}$$

where C_{cp} shall have the value of 1.5, C_r is the pipe resistance coefficient as given in Table A.1 or in Fig. A.1, ρ_s is the minimum fluid mass density for design hydrodynamic loads, I_{tsu} is the importance factor, D_p is the pipe diameter and u is the tsunami flow velocity.

Table A.1. Pipe Resistance Coefficient, C_r

Froude number, F_r	Resistance Coefficient, C_r
0<Fr<0.25	3.6
0.25<Fr<1.3	4.22-2.48Fr
1.3<Fr<2.75	1.0

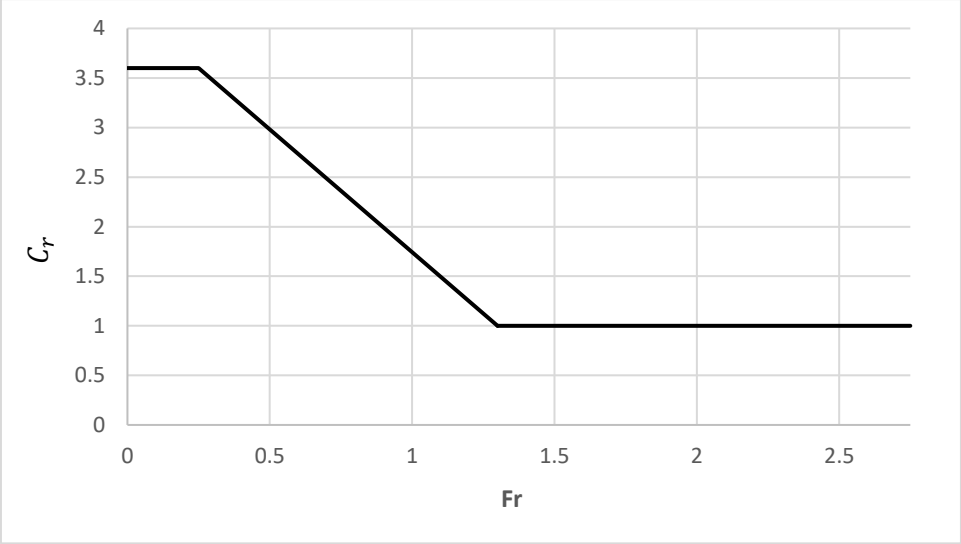

FIGURE A.1 Pipe Resistance Coefficient, C_r, as a Function of the Froude Number, F_r

The upward vertical force per unit length shall be calculated as

$$F_{l+} = C_{cp} C_l^+ \rho_s I_{tsu} D_p u^2 \quad (6.10\text{-}9)$$

where C_{cp} shall have the value of 1.5, C_l^+ is the upward lift coefficient as given in Table A.2 or in Fig. A.2, ρ_s is the minimum fluid mass density for design hydrodynamic loads, I_{tsu} is the importance factor, D_p is the pipe diameter and u is the tsunami flow velocity.

Table A.2. Upward Lift Coefficient C_l^+, for Pipelines

Froude number, F_r	Upward Lift Coefficient, C_l^+
0<Fr<0.25	2.8
0.25<Fr<1.3	3.23-1.71Fr
1.3<Fr<2.75	1.0

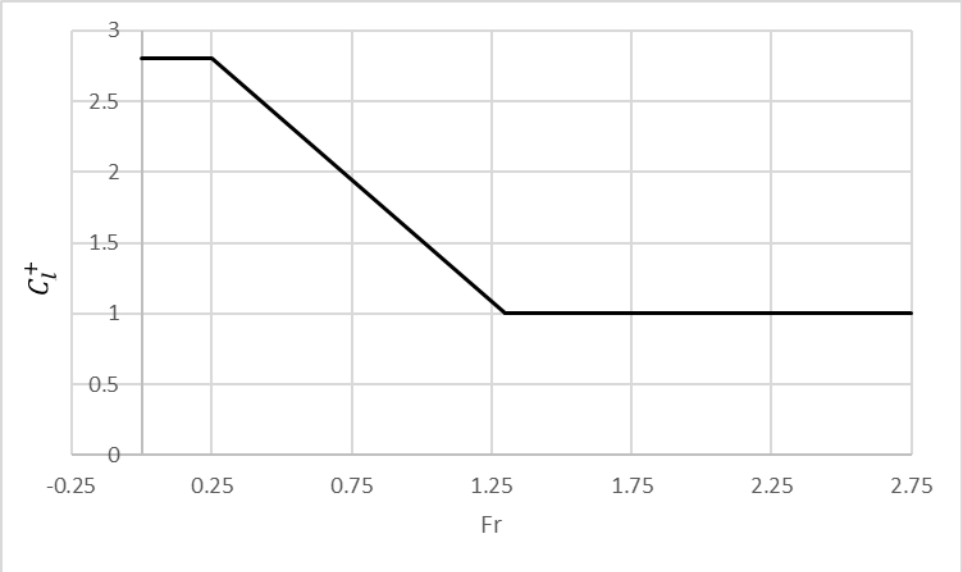

FIGURE A.2 Upward Lift Coefficient, C_l^+ as a Function of the Froude Number, F_r

The downward vertical force per unit length shall be calculated as

$$F_{l-} = C_{cp} C_l^- \rho_s I_{tsu} D_p u^2 \quad (6.10\text{-}10)$$

where C_{cp} shall have the value of 1.5, C_l^- is the downward lift coefficient as given in Table A.3 or in Fig. A.3, ρ_s is the minimum fluid mass density for design hydrodynamic loads, I_{tsu} is the importance factor, D_p is the pipe diameter and u is the tsunami flow velocity.

Table A.3. Downward Lift Coefficient, C_l^-, for Pipelines

Froude number, F_r	Downward Lift Coefficient, C_l^-
0<Fr<0.25	-2.8
0.25<Fr<1.3	2.19Fr-3.35
1.3<Fr<2.75	-0.5

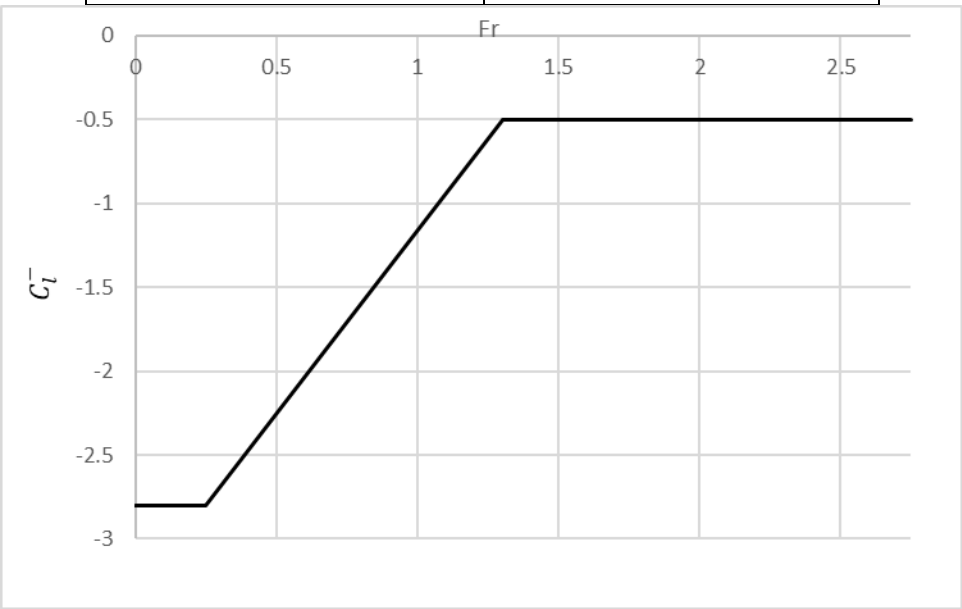

FIGURE A.3 Downward Lift Coefficient, C_l^-, as a Function of the Froude Number, F_r

6.10.2.6.2 Debris impacts on above-ground horizontal pipelines.

Debris impact loads on above ground horizontal pipelines shall be in accordance with Section 6.11.

COMMENTARY CHANGE: (Use ~~strike-out~~ and underline format to indicate text to be replaced and new text, respectively.)

C6.10.2.6 **Loads on Above-Ground Horizontal Pipelines**. The overall lateral resistance force as well as the upward and downward vertical forces caused either by incoming or outgoing flow are given by Eqs. (6.10-8), (6.10-9), and (6.10-10), respectively. Loading on pipelines installed above ground in the tsunami inundation zone is subject to transient, highly turbulent flows. Experimental work of Ghodoosipour et al. (2019a and b) investigated the impact of bores on horizontally placed pipelines for various transient flow conditions and proposed new resistance (C_r) and lift coefficients (C_l) to calculate these forces.
The hydrodynamic loading on above-ground horizontal pipelines due to transient flow conditions was found to depend on: (1) the presence of dry versus wet bed conditions prior to the tsunami

bore impact; (2) the gap between the pipeline and the soil; (3) the degree of pipe submergence. An illustration of these parameters is provided in Fig. A.4. The design tables and figures of Section 6.10.2.6 for the pipe resistance coefficient and lift coefficients encompass these variations.

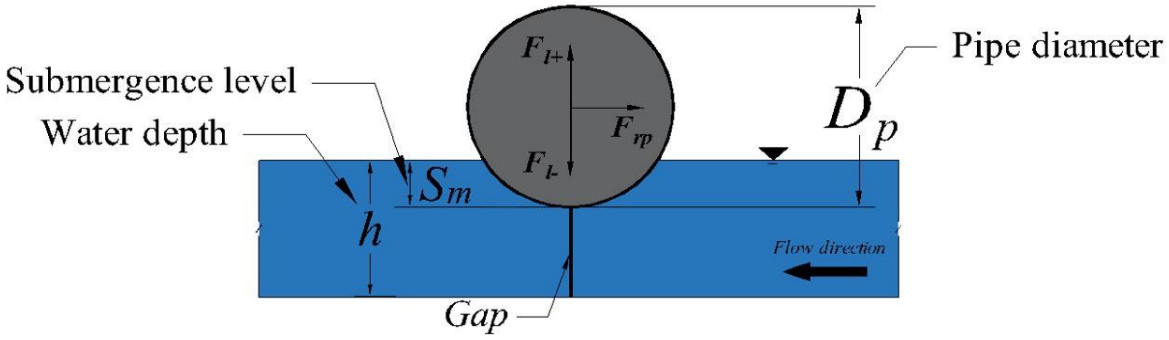

FIGURE A.4. Definition of resistance and lift forces, pipe gap between the pipe and the soil and degree of submergence

Figures A.5 illustrates relationships for the calculated resistance coefficient values as a function of the Froude number for the experiments performed by Ghodoosipour et al. (2019b).

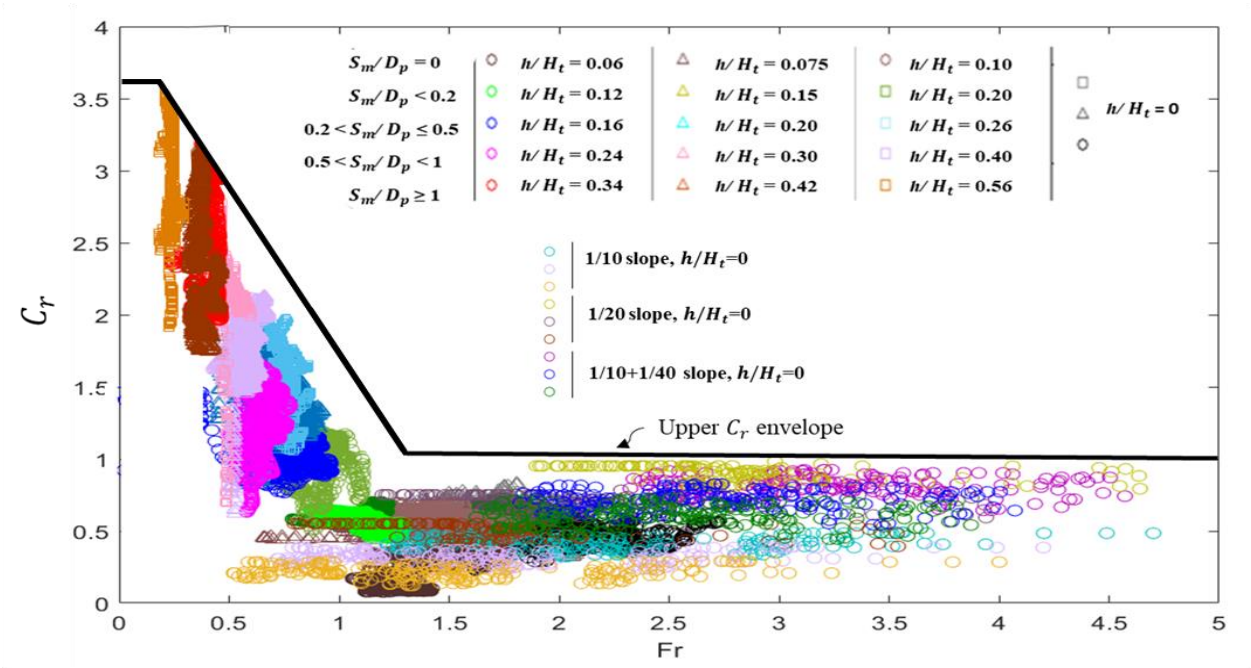

FIGURE A.5. Resistance coefficient, C_r, versus the Froude number, F_r, for different relative bore heights, gap space and degree of submergence

The values of the maximum estimated resistance coefficients were used to determine an upper envelope for the resistance coefficient, C_r. In the case of the dry bed condition, due to the higher flow velocities, the values of the resistance coefficients are found at the right side of the graph, corresponding to the larger Froude numbers which characterized the dry bed condition. Based on the results presented in Figure C6.10-8, the suggested C_r values vary between 1.0 and 3.5. Figure C6.10-8 shows that, for the case of supercritical flows (Fr > 1), C_r values were almost constant, while they linearly increased with a decrease in Fr number in the transitory and subcritical flow regime (Fr < 1). The black line in Figure C6.10-8 represents the upper envelope encompassing the entire range of experimental cases performed, from subcritical to supercritical flow conditions. As shown, it covers a variety of submergence conditions and gap space, as well as both wet and dry bed conditions.

Figures A.6 illustrates relationships for the calculated lift coefficient values as a function of the Froude number for the experiments performed by Ghodoosipour et al. (2019b).

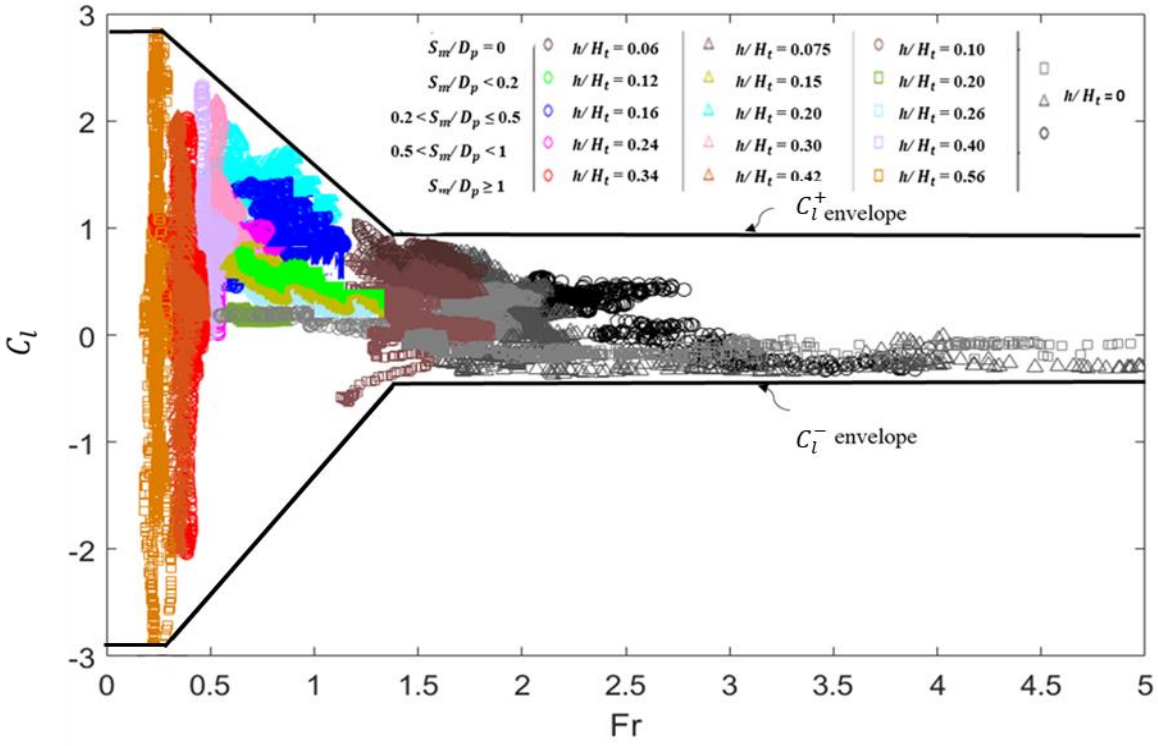

FIGURE A.6. Upward and Downward Lift Coefficients, C_l^+ and C_l^-, versus the i number, F_r, for different bore heights, gap space and degrees of submergence

The maximum upward and downward lift coefficients for all experimental cases were calculated to determine two envelopes which encompassed the variation of these coefficients with the Froude number. The values of the upward lift coefficient, C_l^+ for pipelines subjected to unsteady flow conditions vary in the range of $1.0 \leq C_l^+ < 2.8$ while those of the downward lift coefficient, C_l^- vary in the range of $-2.8 \leq C_l^- < -0.5$. Similar to the resistance coefficient behavior, the upward and downward lift coefficients remained almost constant in the supercritical flow region, while their absolute values increased as the value of F_r decreased in the transitional and subcritical flow region.

Additional References:

1. Ghodoosipour, B., Stolle, J., Nistor, I., Mohammadian, M., Goseberg, N., (2019a). Experimental study on extreme hydrodynamic loading on pipelines. Part 1: Flow hydrodynamics. *J. of Mar. Sci. Eng.*, MDPI, 7, 251; doi:10.3390/jmse7080251
2. Ghodoosipour, B., Stolle, J., Nistor, I., Mohammadian, M., Goseberg, N., (2019b). Experimental study on extreme hydrodynamic loading on pipelines. Part 2: Induced force analysis. *J. of Mar. Sci. Eng.*, MDPI, 7, 262; doi:10.3390/jmse7080262

REASON FOR PROPOSAL: (a reason statement providing the rationale for the proposed change must be provided – attach additional pages if necessary).

The proposed change is to provide for the calculation of hydrodynamic forces exerted on above-ground pipelines subjected to incoming tsunami flow, as well as to include debris impact loads on them. Recent comprehensive experimental work of Ghodoosipour et al. (2019a and b - Part 1 and Part 2) allows for an empirically-based evaluation of the pipe lateral and lift forces that takes into consideration the flow Froude number, and accounts for variations in the geometry of the pipeline placement, including the gap between the pipeline and ground, the degree of submergence, as well as wet versus dry bed conditions just prior to the tsunami inflow propagation.

CONSTRUCTION COST COMMENTS: [Click to Select][Click to Select][Click to Select][Click to Select] [OPTIONAL: Click to enter comments on construction cost impacts.]

Committee Action on Proposal: ApproveApproveApproveApprove Tsunami Loads and Effects Subcommittee has 11 Voting Members, 17 Associate Members Voting Members 8 affirmative, 0 affirmative with comments; 0 negatives.

Appendix B

TRANSIENT DAM-BREAK WAVE LOADING ON PIPELINES NEAR SLOPING BED[4]

Introduction

Extreme events such as tsunamis and floods have caused massive damaging consequences to nearshore infrastructures. This has been more significant recently due to a changing climate. Transmission pipelines are among such infrastructures and need to be protected against potential extreme events. Design of pipelines requires comprehensive understanding of the exerting hydrodynamic forces. Such pipelines are often placed on sloping beds in coastal areas. Therefore, to address the uncertainties and parameters involved in extreme hydrodynamic loading on pipelines near sloping bed, an experimental program was conducted in the hydraulic laboratory at WASEDA University, Tokyo, Japan. This study is a complement of another experimental research conducted by Ghodoosipour et al., 2019a & b to investigate loadings from tsunami-like dam-break waves on pipelines located on flat bed. Both research experiments are in line with the American Society of Civil Engineers, ASCE7 recommendation for studying tsunami loading on pipelines.

Experimental setup

Experimental program was performed in the hydraulic laboratory at the WASEDA University, Tokyo, Japan. The flume was 14.0 m long, 0.40 m wide and 0.80 m high. Tests modeled on-land tsunami flow inundating on sloped coastal plains. This allowed for investigation of the hydrodynamic forces exerted on pipe due to the tsunami wave-induced bores. Different slope levels, as well as various flow conditions, were tested to investigate their influence on exerted forces. Wave gauges and Electromagnetic Current Meter (ECM) were used to measure the time-history of water levels and velocity at different locations along the flume. High-speed cameras were also utilized to observe flow behavior from different angles and to drive bore front velocity using particle image velocimetry (PIV) techniques.

[4] A modified version of this section was published as: Ghodoosipour, B., Takabatake, T., Nistor, I., Mohammadian, M., Hamano, G., Ishii, H., Imura, K., & Shibayama, T. Transient dam-break wave loading on pipelines near sloping bed. Coastal Engineering Proceedings,2020, (36v), waves.55.

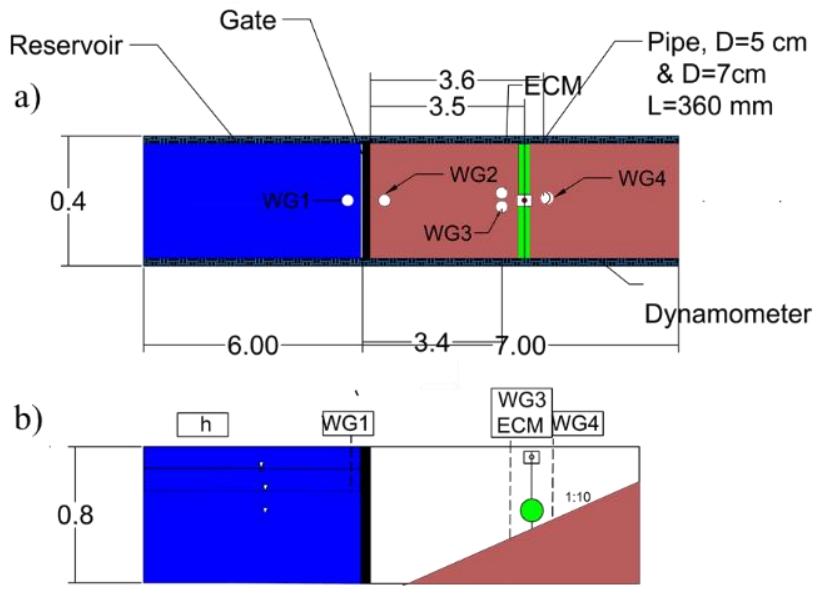

Figure B.1. Experimental setting and instrument locations (a) plan view, (b) side view. (All dimension are in meter)

Three different slope beds i.e., 1:10, 1:20 and a combination of the two slopes as 1:10+1:20 were tested and results were compared against the tests on the flat bed condition. The tested sloped bed configurations are shown in Figure B.2.

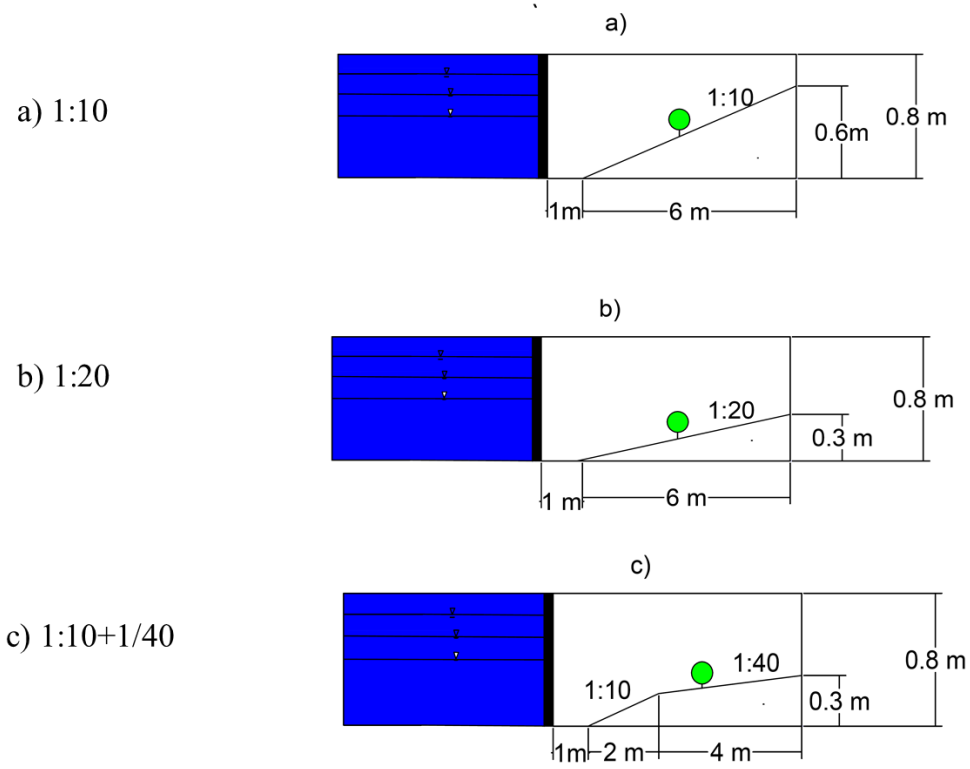

Figure B.2. Three different sloped bed configurations tested in experiments.

Results

Force time history results for flat bed and different slopes are shown in Figure B.3(a) and (b).

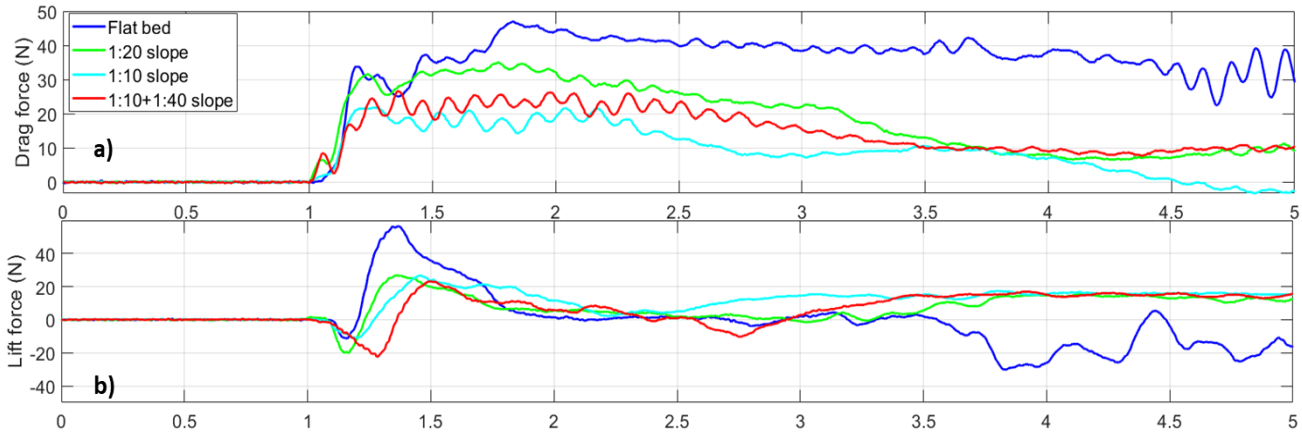

Figure B.3. Time-history of the a) drag force b) lift force for dry-bed condition, h=60cm, flat bed, slopes: 1:10. 1:20, 1:10+1:40.

Results from testing different slope beds show that increasing the steepness of the bed slope leads to a decrease in drag force both at the time of bore impact as impulse force and later in the time-history. Induced drag force magnitude in the case of the combined slopes (1:10+1:40) lies in between the steeper (1:10) and milder slopes (1:20). The lift force peak on the flat bed, is significantly larger compared to the three tested sloped beds. Changing the slope steepness did not change the positive lift force peak magnitude considerably.

In order to compare the test results of different slopes with equal hydraulic head at the location of the pipe, the flat bed results with 0.40 m wave height was compared to 1:20 slope with a 0.50 m wave height and 1:20+1:10 slope with 0.60 m wave height. The head at the location of the pipe for all these three cases is approximately 0.40 m. Figure B.4 shows the results from this comparison.

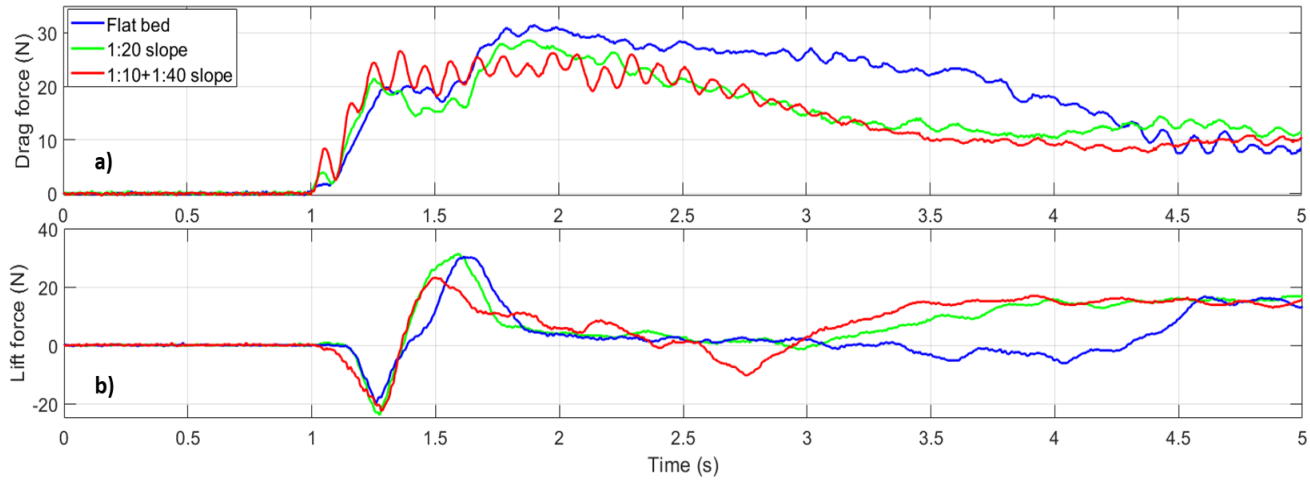

Figure B.4. Time-history of the a) drag force b) lift force for dry-bed condition, h=60cm, flat bed, slopes: 1:10. 1:20, 1:10+1:40.

Results show that drag force magnitude decreases faster for the case of pipes installed on sloped bed compared to the case of flat bed. The maximum force is larger in flat bed compared with the drag force on pipes installed on sloped beds. Figure also shows that the maximum drag force is smaller in the steeper slope (1:10+1:40) compared to the milder slope (1:20). Maximum lift force time-history shows to also decrease for a steeper slope.

Figure B.5, illustrates results for the calculated resistance coefficient values as a function of the Froude number for the sloped bed cases tested in this study together with the calculated coefficients in previously tested cases on flat bed (Ghodoosipour et al. 2019 b).

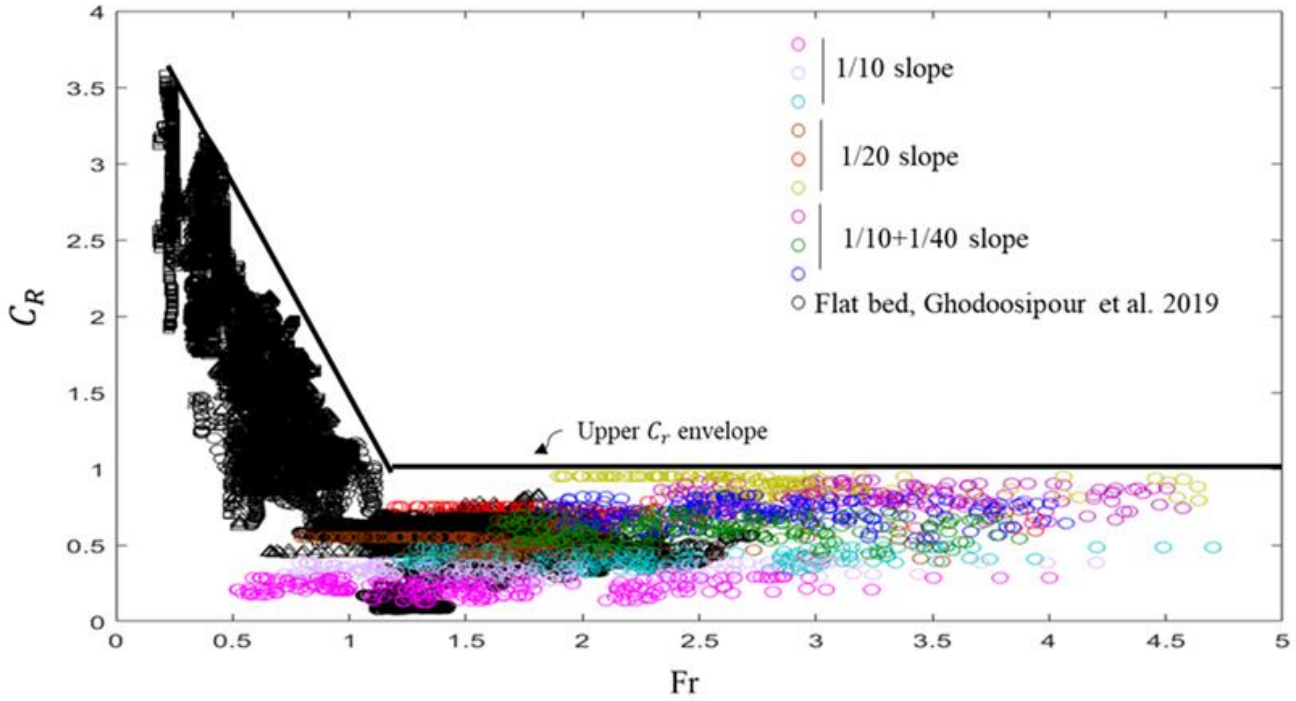

Figure B.5. Calculated resistance coefficient vs. Froude Number for the sloped and flat-bed experiments.

CONCLUSIONS

This study investigates the loading on pipelines located on sloped beds induced by transient dam break wave. Findings of this study helps in characterizing the effect of different slope levels on induced loadings. Drag and lift forces were measured in different flow conditions and slope levels. Results show that both drag and lift forces decrease as the bed slope increases. This study also aimed to calculate force coefficients in different tested configurations. Moreover, results of this study will assist in better understanding of the phenomenon and the improvement of the results obtained from the previous study on flat bed.

References

Achenbach, E. Distribution of local pressure and skin friction around a circular cylinder in cross-flow up to Re = 5× 10^5. *J. Fluid Mech*. **1968**, 34(4):625- 639

Al-Faesly, T.; Palermo, D.; Nistor, I.; Cornett, A. Experimental modelling of extreme hydrodynamic forces on structural models. *Int. J. Prot. Struct.*, **2012**, 3, 477–506.

Angrilli, F.; Bergamaschi, S.; Cossalter, V. Investigation of wall induced modifications to vortex shedding from a circular cylinder. *J. Fluids Eng.*, **1982**, 104, 518-522.

Araki, S.; Deguchi, I. Characteristics of wave pressure and fluid force acting on bridge beam by tsunami. *Coast. Struct.* **2011**, 1299–1310.

Aristodeme, F.; Tripepi, G.; Meringolo, D.D.; Veltri, P. Solitary wave-induced forces on horizontal circular cylinders: Laboratory experiments and SPH simulations. *Coast. Eng.* **2017**, *129*, 17–35.

Aristodemo, F.; Tomasicchio, G.R.; Veltri, P. New model to determine forces at on-bottom slender pipelines. *Coast. Eng. J.*, ***2011***, 58, 267-280.

Aristodeme, F.; Tripepi, G.; Meringolo, D.D.; Veltri, P. Solitary wave-induced forces on horizontal circular cylinders: Laboratory experiments and SPH simulations. *Coast. Eng*. **2017**, 129, 17–35.

Arnason, H. Interactions between an Incident Bore and a Free- Standing Coastal Structure, *Ph.D. dissertation, University of Washington, Seattle, Washington* **2005**.

Arnason, H., Petroff, C., and Yeh, H. Tsunami bore impingement onto a vertical column. *Journal of Disaster Research*, **2009**, 4(6):391–403.

Asakura, R., Iwase, K., Ikeya, T., Takao, M., Kaneto, T., Fujii, N., and Omori, M. An experimental studyonwave force acting on on-shore structures due to overflowing tsunamis. *Proceedings of Coastal Engineering JSCE,* **2000**, 47:911–915.

ASCE/SEI (ASCE/Structural Engineering Institute). Minimum design loads and associated criteria for buildings and other structures. *ASCE/ SEI 7-16*, Reston, VA, **2017**, 25-50.

Bai, J., Ma, N. and Gu, X.. Study of interaction between wave-current and the horizontal cylinder located near the free surface. *Applied Ocean Research*, **2017**, 67, pp.44-58.

Bearman, P.W.; Zdravkovich, M.M. Flow around a circular cylinder near a plane boundary. J. Fluid Mech, **1978**, 89, 33-47.

Bloor, M. S., (1964): The transition to turbulence in the wake of a circular cylinder. J. Fluid Mech, **1964**, 19.02 : 290-304.

Bricker, J.D. On the need for larger Manning's roughness coefficients in depth-integrated tsunami inundation models. *Coast. Eng. J.* **2015**, *57*, 1550005.

Buresti, G.; Lanciotti, A. Mean and fluctuating forces on a circular cylinder in cross-flow near a plane surface. *J. Wind Eng. Ind. Aerod.*, **1992**, 41, 639-650.

Cao, Z.; Yue, Z.; Pender, G. Landslide dam failure and flood hydraulics. Part I: Experimental investigation. *Nat. Hazards* **2011**, *2*, 1003–1019.

Chevalier, C., Lambert, E. and Belorgey, M., 2000, January. Wave forces on a horizontal cylinder in the coastal zone. In The Tenth International Offshore and Polar Engineering Conference. *International Society of Offshore and Polar Engineer*s, **2000**.

Chock, G., Robertson, I., Kriebel, D., Francis, M., and Nistor, I. Tohoku japan tsunami ofmarch 11, 2011 – performance of structures. *American Society of Civil Engineers (ASCE)*, **2012**, 348 pages.

Chock, G. Y. Design for tsunami loads and effects in the asce 7-16 standard. *Journal of Structural Engineering*, **2016**, 142(11):04016093.

CEPA. Pipeline watercourse management program **2013,** *Canadian Energy Pipeline Association*.

Chaplin, J.R. and Subbiah, K.. Large scale horizontal cylinder forces in waves and currents. *Applied Ocean Research,* **1997***, 19*(3-4)*,* pp.211-223.

Chan, I.C.; Liu, L.F. On the run-up of long waves on a plane beach. *J. Geophys. Res.* **2012**, *117*, 72–82.

Chanson, H. Tsunami surges on dry coastal plains: Application of dam break wave equations. *Coast. Eng. J.* **2006**, *48*, 355–370.

Chanson, H. Applications of the Saint-Venant equations and method of characteristics to the dam break wave problem. *Hydraul. Model Rep*. **2005**, *47*, 41–49.

Chanson, H.; Aoki, S.I.; Maruyama, M. An experimental study of tsunami runup on dry and wet horizontal coastlines. *Sci. Tsunami Hazards* **2003**, *20*, 278–293.

Chaplin, J.R. and Subbiah, K.. Large scale horizontal cylinder forces in waves and currents. Applied Ocean Research, **1997**, 19(3-4), pp.211-223.

Chen, C.; Melville, B.W.; Nandasena, N.A.K.; Farvizi, F. An experimental investigation of tsunami bore impacts on a coastal bridge model with different contraction ratios. *J. Coast. Res.* **2017**, *34*, 460–469.

Chow, V. *Open Channel Hydraulics*; McGraw-Hill Book Company, Inc.: New York, NY, USA, **1959**.

Clague, J.J., Munro, A., Murty, T., 2003. Tsunami hazard and risk in Canada. *Natural Hazards*, **2003**, 28, 435-463.

Coulibaly, P., Bobée, B. and Anctil, F. Improving extreme hydrologic events forecasting using a new criterion for artificial neural network selection. Hydrological Processes, **2001**, 15(8), pp.1533-1536.

Dames, M. Design and construction standards for residential construction in tsunami-prone areas in Hawaii. Federal Emergency Management Agency (FEMA), **1980**, Washing- ton DC, USA.

Dias, P.; Dissanayake, R.; Chandratilake, R. Lessons Learned from Tsunami Damage in Sri Lanka. *Civil Eng.* **2006**, *159*, 74–81, doi:10.1680/cien.2006.159.

Dias, W. and Mallikarachchi, H. Tsunami-planning and design for disaster mitigation. *Structural Engineer*, **2006**, 84(11):25.

Douglas, S.; Nistor, I. On the effect of bed condition on the development of tsunami-induced loading on structures using OpenFOAM. *Nat. Hazards* **2015**, *2*, 1335–1356.

Drescher, H. (1956): Messung der auf querangestromte Zylinder ausgeiibten zeitlich veranderten Driicke. Z. f. Flugwiss, **1956**, 4(112):17-21.

El-Shafie, A., Najah, A., Alsulami, H.M. and Jahanbani, H. Optimized neural network prediction model for potential evapotranspiration utilizing ensemble procedure. Water resources management, **2014**, 28(4), pp.947-967.

FEMA P646. Guidelines for the design of structures for vertical evacuation from tsunamis. *Federal Emergency Management Agency, Washington,* D.*C.* **2012**, 174.

Fluent, A.N.S.Y.S. Ansys fluent. *Academic Research. Release*, 2015, 14.

Foster, A.S.J.; Rossetto, T.; Allsop, W. An experimentally validated approach for evaluating tsunami inundation forces on rectangular buildings. *Coast. Eng. J.* **2017**, *128*, 44–57.

Fritz, H.M.; Phillips, D.A.; Okayasu, A.; Shimozono, T.; Liu, H.; Mohammed, F.; Skanavis, V.; Synolakis, C.E.; Takahashi, T. The 2011 Japan tsunami current velocity measurements from survivor videos at Kesennuma Bay using LiDAR. *Geophys. Res. Lett.* **2012**, *39*.

Fujima, K., Achmad, F., Shigihara, Y., and Mizutani, N. Estimation of tsunami force acting on rectangular structures. *Journal of Disaster Research*, **2009**, 4(6):404–409.

Gao, F.P.; Gu, X.Y.; Jeng, D.S.; Teo, H.T. An experimental study for wave-induced instability of pipelines: The breakout of pipelines. *Appl. Ocean Res*. **2002**, 24, 83–90.

Gao, N., Yang, J., Li, X. and Zhao, W.. Wave forces on horizontal cylinder due to nonlinear focused wave groups. In The Twenty-fifth International Ocean and Polar Engineering Conference. *International Society of Offshore and Polar Engineers*. **2015**.

Gedik, N.; Irtem, E.; Kabdasli, S. Laboratory investigation on tsunami run-up. Ocean Eng. **2005**, 32, 513–528.

Gerrard, J. H. The wakes of cylindrical bluff bodies at low Reynolds number. *Philosophical Transactions of the Royal Society of London A: Mathematical, Physical and Engineering Sciences*. **1978**, 288.1354: 351-382.

Ghodoosipour, B.; Stolle, J.; Nistor, I.; Mohammadian, A.; Goseberg, N. Experimental study on extreme hydrodynamic loading on pipelines. Part 1: Flow hydrodynamics. *J. Mar. Sci. Eng*. **2019.**

Ghodoosipour, B.; Stolle, J.; Nistor, I.; Mohammadian, A.; Goseberg, N. Experimental study on extreme hydrodynamic loading on pipelines part 2: Induced force analysis. *JMSE* **2019**.

Gómez-Gesteira, M. and Dalrymple, R.A. Using a three-dimensional smoothed particle hydrodynamics method for wave impact on a tall structure. *Journal of waterway, port, coastal, and ocean engineering*, **2004**, 130(2), pp.63-69.

Goseberg, N.; Schlurmann, T. Non-stationary flow around buildings during run-up of tsunami waves on a plain beach. In Proceedings of the Coastal Engineering Conference, *American Society of Civil Engineers (ASCE)*, Reston, VA, USA, **2014**.

Grass, A.J.; Raven, P.W.J.; Stuart, R.J.; Bray, J.A. The influence of boundary layer velocity gradients and bed proximity on vortex shedding from free spanning pipelines, *J. Energ. Resour-ASME*, **1984**, 106, 70-78.

Gupta, V. P.; Goyal, S. C. Hydrodynamic forces on bridge piers, *Journal of the Institution of Engineers (India), Civil Engineering Division*, **1975**, 56, 12–16.

Haley, J.F.; Swan, C.; Gibson, R. An Experimental Investigation of Wave Impact Loads on a Slender Horizontal Cylinder. In Proceedings of the ASME 2014 33rd International Conference on Ocean, Offshore and Arctic Engineering, San Francisco, CA, USA, 8–13 June **2014**; *American Society of Mechanical Engineers*: New York, NY, USA, **2014**; p. V08BT06A041.

Henderson, F.M. *Open Channel Flow*; MacMillan Company: New York, NY, USA, **1966**.

Hsiao, S.C.; Lin, T.C. Tsunami-like solitary waves impinging and overtopping an impermeable seawall: Experiment and RANS modeling. *Coast. Eng.* **2010**, *57*, 1–18.

Istrati, D.; Buckle, I.; Lomonaco, P.; Yim, S. Deciphering the tsunami wave impact and associated connection forces in open-girder coastal bridges. *J. Mar. Sci. Eng.* **2018**, *6*, *148*.

Jaffe, B.E.; Goto, K.; Sugawara, D.; Richmond, B.M.; Fujino, S.; Nishimura, Y. Flow speed estimated by inverse modeling of sandy tsunami deposits: Results from the 11 March 2011 tsunami on the coastal plain near the Sendai Airport, Honshu, Japan. *Sediment. Geol.* **2012**, *282*, 90–109.

Kawamura T, Mayer S, Garapon A, Sorensen L Large Eddy simulation of a flow past a free surface piercing circular cylinder. *ASME J Fluids Eng* **2002**, 124:91–101.

Khosronejad, A., Kang, S., Borazjani, I. and Sotiropoulos, F. Curvilinear immersed boundary method for simulating coupled flow and bed morphodynamic interactions due to sediment transport phenomena. *Advances in water resources*, **2011**, 34(7), pp.829-843.

Kreibich, H., Thieken, A. H., Petrow, T., Müller, M., andMerz, B. (2005). Flood loss reduction of private households due to building precautionarymeasures–lessons learned from the elbe flood in august **2002**. NaturalHazards andEarth System Science, 5(1):117–126.

Lauber, G.; Hager, W.H. Experiments to dam break wave: Horizontal channel. *J. Hydraul. Res.* **1998**, *3*, 291–307.

Leal, J.G., Ferreira, R.M. and Cardoso, A.H. Dam-break wave-front celerity. *Journal of Hydraulic Engineering*, **2006**, 132(1), pp.69-76.

Lee, Y.G., Hong, S.W. and Kang, K.J. January. A numerical simulation of vortex motion behind a circular cylinder above a horizontal plane boundary. *Fourth International Offshore and Polar Engineering Conference. International Society of Offshore and Polar Engineers*. **1994**.

Lei, C.; Cheng, L.; Kavanagh, K. Re-examination of the effect of a plane boundary on force and vortex shedding of a circular cylinder. *J. Wind Eng. Ind. Aerod.*, **1999**, 80, 263-286.

Li, Y.; Lin, M. Hydrodynamic coefficients induced by waves and currents for submerged circular cylinder. *Procedia Eng.*, **2010**, 4, 253-261.

Limura, K.; Norio, T. Numerical simulation estimating effects of tree density distribution in coastal forest on tsunami mitigation. *Ocean Eng.* **2012**, *54*, 223–232.

Madsen, A.; Schäffer, H.A. Analytical solutions for tsunami run-up on a plane beach: Single waves, N-waves and transient waves. *J. Fluid Mech.* **2010**, *645*, 27–57.

Madsen, A.; Fuhrman, D.R.; Schäffer, H.A. On the solitary wave paradigm for tsunamis. *J. Geophys. Res.* **2008**, *113*, 286–292.

Matsutomi, H.; Okamoto, K. Inundation flow velocity of tsunami on land. *Island Arc*. **2010**, *3*, 443–457.

Mazinani, I.; Ismail, Z.; Hashim, A.M.; Saba, A. Experimental investigation on tsunami acting on bridges. *Int. J. Civ. Env. Eng*. **2014**, *8*, 1040–1043.

Morison, J.R., Johnson, J.W. and Schaaf, S.A. The force exerted by surface waves on piles. Journal of Petroleum Technology, **1950**, 2(05), pp.149-154.

Mouazé, D. and Bélorgey, M.. Flow visualisation around a horizontal cylinder near a plane wall and subject to waves. *Applied ocean research*, **2003**, 25(4), pp.195-211.

Nakano, Y. Design load evaluation for tsunami shelters based on damage observations after Indian Ocean tsunami disaster due to the 2004 Sumatra earthquake. *The 14thWorld Conference on Earthquake Engineering*, Beijing, China, **2008**, 12 - 17 October.

Nicholls, R.J. Coastal flooding and wetland loss in the 21st century: Changes under the SRES climate and socio-economic scenarios. *Glob. Environ. Change* **2004**, *1*, 69–86.

Nishino, T., Roberts, G.T., Zhang, X. Vortex shedding from a circular cylinder near a moving ground. *Physics of Fluids*, **2007**,19, 025103.

Nishino, T., Roberts, G.T. and Zhang, X. Unsteady RANS and detached-eddy simulations of flow around a circular cylinder in ground effect. *Journal of Fluids and Structures*, **2008**, 24(1), pp.18-33.

Nouri, Y.; Nistor, I.; Palermo, D. Experimental investigation of tsunami impact on free standing structures. *Coast. Eng. J.* **2010**, 52, 43-70.

Okada, T., Sugano, T., Ishikawa, T., Ohgi, T., Takai, S., and Hamabe, C. Structural design method ofbuildings for tsunami resistance. *BuildingTechnologyResearch Institute, Building Centre for Japan*, **2005**, 15, Tokyo, Japan.

Palermo, D.; Nistor, I.; Al-Faesly, T.; Cornett, A. Impact of tsunami forces on structures: The University of Ottawa experience. *In Proceedings of the Fifth International Tsunami Symposium, Ispra, Italy,* **2012**, 3-5.

Park, H., Cox, D.T., Lynett, P.J., Wiebe, D.M., Shin, S. Tsunami inundation modeling in constructed environments: a physical and numerical comparison of free-surface elevation, velocity, and momentum flux. *Coastal Engineering*, **2013**, 79, 9‑21.

Prasad, S. *Wave Impact Forces on a Horizontal Cylinder*; Doctoral dissertation, University of British: Columbia, UK, **1994**.

Peakall, J.; Warburton J. Surface tension in small hydraulic river models- The significance of the Weber number. *J. Hydrol. (New Zealand)* **1998**, *35*, 199–212.

Qi, Z.X.; Eames, I.; Johnson, E.A. Force acting on a square cylinder fixed in a free surface channel flow. *J. Fluid Mech.*, **2014**, 756, 716–727.

Ramsden, J.D. Forces on a vertical wall due to long waves, bores, and dry-bed surges. *Journal of waterway, port, coastal, and ocean engineering*, **1996**, 122(3), pp.134-141.

Ribés, A., Bruneton, A. and Geay, A.. SALOME: An open-source simulation platform integrating Paraview. Tech Rep, **2017**, p 7.

Ritter, A. Die Fortpflanzung der Wasserwellen. *Z Des. Vereines Dtsch. Ingenieure* **1892**, *36*, 947–954

Robertson, I. N., Pacskowski, K., Riggs, H. R., and Mohamed, A. (2013). Experimental investigation of tsunami bore forces on vertical walls. *Journal of Offshore Mechanics and Arctic Engineering*, **2013**, 135(2):1–8.

Robertson, I. N. Tsunami loads and effects: Guide to the tsunami design provisions of asce 7-16. *American Society of Civil Engineers (ASCE)*, Reston (VA), USA, **2016**.

Rossetto, T.; Peiris, N.; Pomonis, A.; Wilkinson, S.M.; Re, D.; Koo, R.; Gallocher, S. The Indian Ocean tsunami of December 26, 2004: Observations in Sri Lanka and Thailand. *Nat. Hazards*. **2007**, *1*, 105–124.

Rusche, H. Computational fluid dynamics of dispersed two-phase flows at high phase fractions. PhD thesis, Imperial College, London, UK, **2002**.

Schewe, G. : "On the force fluctuations acting on a circular cylinder in crossflow from subcritical up to transcritical Reynolds numbers." *J. Fluid Mech*. **1983**, 133:265-285.

Schmid, P. and Sesterhenn, *J. Dynamic mode decomposition of numerical and experimental data*. APS, **2008**, 61, pp.MR-007.

Sarpkaya, T., Isaacson, M.. Mechanics of Wave Forces on Offshore Structures. *Van Nostrand Reinhold Company*. **1981**, 650 pp.

Sibley, P., Coates, I.E., Arumugam, K.. Solitary wave forces on horizontal cylinders. *Appl. Ocean Res*. **1982**, 4(2), 113-117.

Spalart, P. and Allmaras, S. January. A one-equation turbulence model for aerodynamic flows. *In 30th aerospace sciences meeting and exhibit*, **1992**, p. 439.

Spalart, P.R., Jou, W. H., Strelets, M., Allmaras, S.R.: Comments on the feas1ibility of LES for wings, and on a hybrid RANS/LES approach. In: Proceedings of first AFOSR international conference on DNS/LES, Ruston, Louisiana. Greyden Press, **1997**.

Spalart, P.R., Deck, S., Shur, M., and Squires, K.D. "A New Version of Detached-Eddy Simulation, Resistant to Ambiguous Grid Densities," Theoritical and Computational Fluid Dynamics,**2006**, vol. 20, pp. 181–195.

Spalart, P.R., Coleman, G.N. and Johnstone, R. Direct numerical simulation of the Ekman layer: A step in Reynolds number, and cautious support for a log law with a shifted origin. *Physics of Fluids*, **2008**, 20(10), p.101507.

Subbiah, K.; Cheong, H.F.; Shankar, N.J. Regular and random wave pressures around large diameter submarine pipeline near ocean bed. *J. Hydraul. Res.* **1991**, 29, 49–66.

St-Germain, P.; Nistor, I.; Townsend, R.; Shibayama, T. Smoothed-particle hydrodynamics numerical modelling of structures impacted by tsunami bores. *J. Water W Port Coast* **2013**, *1*, 66–81.

Stoker, J.J. *Water Waves: The Mathematical Theory with Applications*; John Wiley Sons: Hoboken, NJ, USA, 1958.

Stolle, J.; Ghodoosipour, B.; Derschum, C.; Nistor, I.; Petriu, E.; Goseberg, N. Swing gate generated dam-break waves. *J. Hydraul. Res.* **2018**, 1–13.

Subbiah, K.; Cheong, H.F.; Shankar, N.J. Regular and random wave pressures around large diameter submarine pipeline near ocean bed. J. Hydraul. Res. **1991**, 29, 49–66.

Sumer, B.M.; Fredsøe, J. *Hydrodynamics Around Cylindrical Structures*; World Scientific Publishing Company: Singapore, **1989**.

Sumer, B.; Christiansen, N.; Fredsoe, J.The horseshoe vortex and vortex shedding around a vertical wall-mounted cylinder exposed to waves. *Journal of Fluid Mech*. **1997**, 332, 41–70.

Sundar, V.; Vengatesan, V.; Anandkumar, G.; Schlenkhoff. A. Hydrodynamic coefficients for inclined cylinders. *Ocean Eng. J.*, **1998**, 25, 277–294.

Synolakis, C.E. The run-up of solitary waves. *J. Fluid Mech.* **1987**, *185*, 523–545.

Tong, F.F.; Cheng, L.; An, H.; Griffiths, T. The hydrodynamic forces on a circular cylinder in proximity to a wall with intermittent contact in steady current. Ocean Eng. **2017**, 146, 424–433.

Wei, Z., Dalrymple, R.A., Hérault, A., Bilotta, G., Rustico, E. and Yeh, H. SPH modeling of dynamic impact of tsunami bore on bridge piers. *Coastal Engineering*, **2015**, 104, pp.26-42.

Williamson, C. H. The existence of two stages in the transition to three-dimensionality of a cylinder wake. *California Inst of Teck Pasadena Graduate Aaronatical Labs*. **1988**.

Wüthrich D. Extreme Hydrodynamic impact onto buildings. *PhD thesis, EPFL*; **2018**.

Wüthrich, D.; Pfister, M.; Nistor, I.; Schleiss, A.J. Experimental study of tsunami-like waves generated with a vertical release technique on dry and wet beds. *J. Water W Port Coast*, **2018a**, *4*, 04018006.

Wüthrich, D.; Pfister, M.; Nistor, I.; Schleiss, A.J. Experimental study on the hydrodynamic impact of tsunami-like waves against impervious free-standing buildings. *Coast. Eng. J.* **2018b**, *60*, 180–199.

Wüthrich, D.; Pfister, M.; Nistor, I.; Schleiss, A.J. Experimental study on forces exerted on buildings with openings due to extreme hydrodynamic events. *Coast. Eng. J.* **2018c**, *140*, 72–86.

Yeh, H. Design tsunami forces for onshore structures, *J. Disaster Res.*, **2007**, 2, 531-536.

Yeh, H., Robertson, I., and Preuss, J. Development of design guidelines for structures that serve as tsunami vertical evacuation sites. Open File Report2005-4, *Washington State Department of Natural Resources, Division of Geology and Earth Resources*, *USA*, **2005**, 42 pages.

Xiao, H., Huang, W., Tao, J. and Liu, C. Numerical modeling of wave–current forces acting on horizontal cylinder of marine structures by VOF method. *Ocean Engineering*, **2013**, 67, pp.58-67.

Yakhot, V. and Orszag, S.A. Renormalization group analysis of turbulence. I. Basic theory. *Journal of scientific computing*, **1986**, 1(1), pp.3-51.

Yan, X. and Mohammadian, A. Numerical modeling of vertical buoyant jets subjected to lateral confinement. *Journal of Hydraulic Engineering*, **2017**, 143(7), p.04017016.

Zdravkovich, M.M. Forces on a circular cylinder near a plane wall, *Appl. Ocean Res.*, **1985**, 7, 197-201.

Zhao, E.; Qu, K.; Mu, L.; Kraatz, S.; Shi, B. Numerical study on the hydrodynamic characteristics of submarine pipelines under the impact of real-world tsunami-like waves. *Water*, **2019**, 11.

Zhiyin, Y., 2015. Large-eddy simulation: Past, present and the future. *Chinese Journal of Aeronautics* , **2015**, 28, 11–24. https://doi.org/10.1016/j.cja.2014.12.00